Microstructural Effects on the Hydrogen Embrittlement of High Strength Steels

A Thesis

Submitted to the Faculty

of

Drexel University

by Andrew W. DeVillier

in partial fulfillment of the

requirements for the degree

of

Master of Science in Materials Science and Engineering

October 2010

©Copyright 2009-2010
Andrew W. DeVillier. All Rights Reserved.

Acknowledgements

First, I'd like to thank my advisors, Professor Roger Doherty and Mr. Christopher Hovanec, for their insightful discussions and continual guidance over the course of this work. You were both instrumental to my success, and I look forward to future projects.

Second, I'd like to thank NAVAIR and the SMART Program for funding this work. It has been an incredible experience. Several people were key in this project, especially Mr. Joseph Bilko, Mr. Robert Taylor, Dr. Bruce Pregger, and Mr. Bill Lightell, who I would like to thank for the various training, machining, and metallography work.

Finally, I cannot begin to express my gratitude and love to my family, especially Mom and Dad, for the sacrifices you have made to give me the best opportunities possible (and for putting up with me for the past 23 years). Without your support, I would not be who I am, or where I am, today.

Table of Contents

List of Tables

List of Figures

Abstract

Microstructural Effects of Hydrogen Embrittlement in High Strength Steels

Andrew DeVillier

Roger Doherty, D. Phil

Christopher Hovanec

High-strength, high-toughness steels are used in critical components of Naval aviation systems. These critical applications include landing gear components in tactical aircraft and rotary components in helicopters where large stresses must be sustained and the probability of failure due to flaws in the part are kept minimal. To prevent corrosion and wear, high strength steels are plated. When parts undergo repair/rework, the plating is stripped in an acidic bath, and the part is re-plated. During stripping and plating, as well as in-service duty, the steel is exposed to hydrogen-rich environments, which have been identified as a potential cause of premature failures in aviation system components. A high strength, precipitation hardened steel, PH 13-8Mo, one of six candidate steels, was examined in three different conditions – solution annealed (SA), H1000 (538^{o}C aged), and H1150 (621^{o}C aged) in order to compare the susceptibility of the different microstructures to hydrogen embrittlement and determine the stress-life curve for PH13-8 Mo in the H1000 condition. The PH 13-8Mo was selected as a result of a recent in-service failure of a reworked component.

Fatigue pre-cracked compaction-tension (CT) specimen were loaded in displacement control and seated in a 10% strength hydrochloric acid bath. The load and crack mouth opening displacement (CMOD) were monitored as a function of time. From the load and CMOD versus time behavior, failure criterion were developed to determine points of crack initiation.

Fractured samples were examined via scanning electron microscopy (SEM). Polished samples of the H1000, SA and H1150 condition were also analyzed by electron backscatter diffraction (EBSD). EBSD analysis showed that the packets of reverted austenite that grew in the H1150 condition material possessed an orientation that tended towards [111], which may indicate a Kurdjumov-Sachs or Nishiyama-Wasserman orientation relationship. In addition, packets of austenite within a local region also shared a common orientation with one another. An explanation for this behavior is proposed.

The hydrogen embrittlement results show that the H1000 condition is highly susceptible to crack initiation over a wide range of applied stress values. A comparison of the different conditions showed that the H1150 and SA conditions possessed similar equal or better resistance to crack initiation in the hydrogen-rich environment at equivalent values of applied stress intensity (K) than the H1000 condition. Comparing equal percentages of applied (apparent) fracture toughness (K_Q or K_{IC}), only the SA condition had better resistance to initiation than the H100 condition. Resistance to *crack propagation* for the H1150 and SA conditions was superior to that of the H1000 condition. Finally, the threshold stress intensity, K_{th}, below which no cracking occurs for the H1000 condition, is on the order of 10% K_{IC} or less, which is in good agreement with what has been established in literature.

Chapter 1: Introduction

High strength steels have been used historically utilized in pressure vessels for the nuclear and petroleum industries as well as in structurally critical components for the aircraft industry. More recently, high strength steels have been utilized in automobiles as reinforcing members. Of the many degradation mechanisms causing component fracture (corrosion, etc.), hydrogen embrittlement has been one of the toughest to eliminate, as evidence by the fact that conferences and reports on the effects of hydrogen in steels stretch back to the 1950's and 1960's, some of the earliest being on the effects of hydrogen on the mechanical properties in uranium (1). Despite large efforts to limit damage due to hydrogen, hydrogen embrittlement still plagues modern, ultra-high strength steels today (2). It has particularly become a problem in naval aviation, where exposure to a variety of environments – corrosive chemicals, high stresses, continuous electric fields, and salt water – promotes the uptake of atomic hydrogen into the crystal lattice, which weakens the steel and causes premature failure. Several failures of system-critical components have occurred during both repair/rework and in-field service (3). Among the many processes that may be involved with introducing hydrogen into the steel, electroplating and acid stripping are considered to be the most damaging environments. In order to prevent corrosion and increase wear resistance, many parts are electroplated with an oxide forming metal such as chromium or cadmium. Hydrogen generation is inherent to these plating processes. Various stripping agents, including hydrochloric acid (HCl) are used to remove the coatings when a part returns from the field in need of service. Failures in and out of the field are not only costly, but impose unnecessary and potentially even deadly risk.

PH 13-8Mo, a precipitation hardening, ultra-high strength martensitic stainless steel, which is certified for use in Naval aircraft, was selected to be stressed under a hydrogen rich (acidic) environment in order to characterize its susceptibility to hydrogen embrittlement. Comparisons are made between three heat treatments:

"**SA**" - solution annealed, 100% martensite supersaturated with alloying elements;

"**H1000**" - 538^{o}C (1000^{o}F) aged martensite with nanoscale NiAl precipitates, and a small fraction of reverted austenite;

"**H1150**" - 621^{o}C (1150^{o}F) aged martensite with coarser Ni_3Mo/Ni_4Mo precipitates and a larger volume fraction of reverted austenite (4).

The fractured surfaces were examined with scanning electron microscopy (SEM) to determine whether any changes in fracture behavior/morphology (ductile vs. brittle fracture) occurred as the microstructure changed.

The following schematic graph, featured in a number of sources (refs), shows how stress (or stress intensity, K, for samples with cracks) is predicted to vary with time under an aggressive environment:

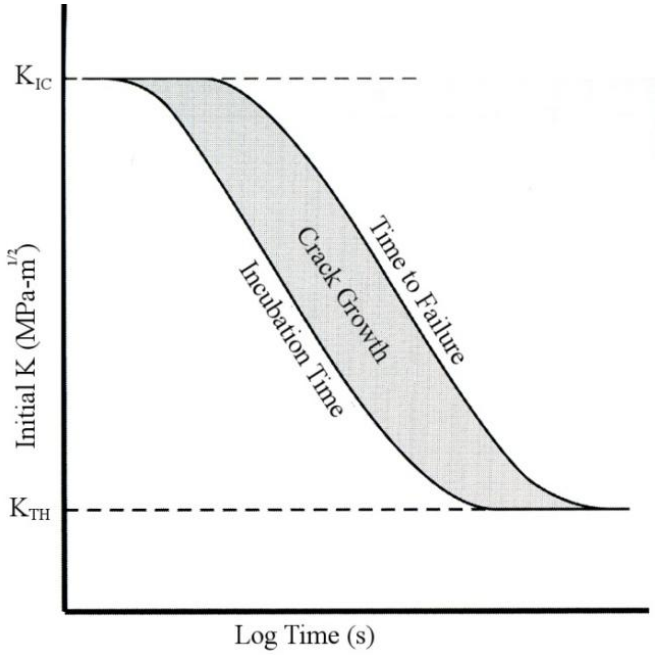

Figure 1: The Schematic Stress Intensity vs. Life Curve
At K_{IC}, fracture is instant. Below, there is a time delay before crack initiation.
Image courtesy of T.L. Anderson (5)

The generation of this curve for PH 13-8Mo in the H1000 condition is one of the primary goals of this work, since it is the most commonly used heat treatment. At the top of the curve is the plane strain fracture toughness, K_{IC}, which is a measurement of a material's resistance crack extension when the crack tip is at maximum constraint. Below K_{IC}, there is a distinctive time between immersion in the hydrogen environment (time=0) and the time of crack initiation for a given K level. Assuming a constant K value, there will then also be a characteristic time between crack initiation and complete failure of the sample. At the lower critical stress intensity level and below (K_{TH}), no crack growth occurs. It should be noted that the lower critical stress is somewhat arbitrarily defined – with infinitely sensitive equipment and time periods, one could always detect some level of crack growth. Based on ASTM E1681, the lower critical stress (threshold) value is defined as no crack growth after 5000 hours in the environment

for an ultra-high strength steel (6). For the purposes of this testing, 5000 hours is prohibitively long, and also not representative of the time spent in acid baths at Navy repair depots.

While high strength is important for any structural application, high toughness – the ability to tolerate flaws such as cracks – is even more critical. Naval aviation system design is based on fracture toughness (high stress, critical loading) rather than fatigue (low stress, cycling loading) because of the harsh operating environments and limited repair facilities in the field.

SEM fractography has long been used to examine the fracture surfaces of materials to try and determine how and why a material failed. For example, a crack may have nucleated at an inclusion within the material or at a brittle grain boundary, locally increasing the stress and causing premature fracture.

In addition to SEM analysis under secondary mode, electron backscatter diffraction (EBSD) was also used to characterize the structure of PH 13-8Mo in various heat treatments. As a result of the investigation, it is proposed (though not entirely confirmed) that the reverted austenite formed during the aging process not only possesses a specific orientation relationship (the Kurdjumov-Sachs relationship, as proven in literature (7; 8) but that it also possesses the orientation of the parent prior austenite grain.

Chapter 2: Literature Survey and Background

Hydrogen Embrittlement Theory

Hydrogen presents itself as a problem in steels largely because it is a small, diffusible atom that can be transported not only through traditional diffusion but dislocation transport and other mechanisms as well. Gaseous hydrogen typically obeys Sievert's Law (9):

$$C = K\sqrt{P} \qquad [1]$$

In Equation [1], C is the concentration of hydrogen, K is the constant of proportionality, and P is the pressure of the hydrogen in the environment. However, hydrogen concentrations at notches and stress concentrations can be significantly higher, particularly in aqueous environments. Though the overall solubility of hydrogen in iron is not very high – typically parts per million – austenite (FCC iron) does have a much higher solubility limit than ferrite (BCC iron). This difference is exacerbated greatly as the hydrogen pressure is increased

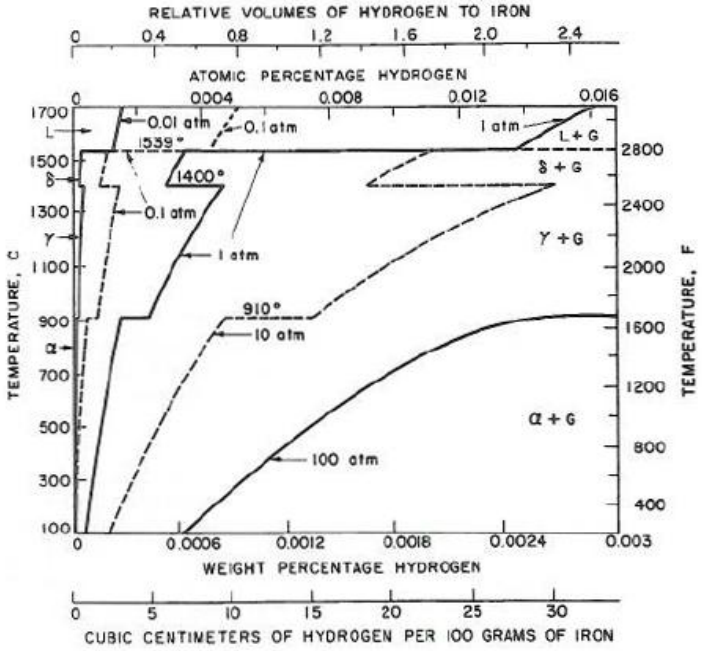

Figure 2: The Hydrogen-Iron Phase Diagram.
Notice the large decrease in solubility at 910°C (the beginning of the ferrite-austenite transition). Image courtesy of Pressouyre and Interrante (9).

Intuitively, one would expect that hydrostatic tensile stress would actually *reduce* hydrogen concentration around a crack tip based on Equation [1], since pressure is a hydrostatic *compressive* stress. However, the dilatation (hydrostatic expansion) caused by the movement of hydrogen into an interstitial site causes a gradient in the chemical potential of the hydrogen (10), which creates a driving force for the diffusion of hydrogen. As long as the state of stress is maintained, the triaxial region keeps its locally increased solubility, so no H supersaturation exists. If the stress is removed, then H will be in a supersaturated state and may begin to precipitate/react. This effect is described by Einstein diffusion, given by (10):

$$J = -\left(\frac{Dc}{kT}\right)\left(\frac{\delta\mu}{\delta r}\right) \qquad [2]$$

where J is the flux, D is the diffusivity, c is the concentration of hydrogen, k is Boltzmann's constant, T is temperature, μ is the chemical potential, and r is the radial position. Thus, counterintuitive to Sievert's Law, which shows a hydrostatic *compressive* stress promoting hydrogen uptake, hydrogen ingress is actually *promoted* in the region of triaxial *tensile* stress surrounding a crack, thus increasing the probability of failure when a cracked part is exposed to a hydrogen-rich environment. In plotting solubility versus temperature, it is seen that below 400^{o}C the hydrogen solubility limit is much greater than if the curve were extrapolated (see Figure 3 below). This is a result of traps being able to retain hydrogen at sites other than the interstices. A trap is any structure – grain boundary, austenite, ferrite, martensite, a carbide or intermetallic precipitate, oxide inclusion, etc. – that can retain hydrogen in the crystal lattice. Traps have a certain binding energy associated with them, essentially determining how strong a hold each trap has on atomic hydrogen. Observing the solubility curve below in Figure 3, there is a large difference between the expected concentration of hydrogen and the experimentally observed concentration as a result of traps within the iron. Above 400^{o}C, where the two curves meet, it appears all traps are relieved of hydrogen and only the interstices remain as available sites for hydrogen. This temperature approaches the temperatures of many low temperature heat treatments of steel, meaning that the heat treatments meant to remove hydrogen may cause undesirable microstructural changes in addition to removing the hydrogen. At room temperature, the interstitial hydrogen may only represent a small fraction of the total hydrogen content (the majority being held at trap sites).

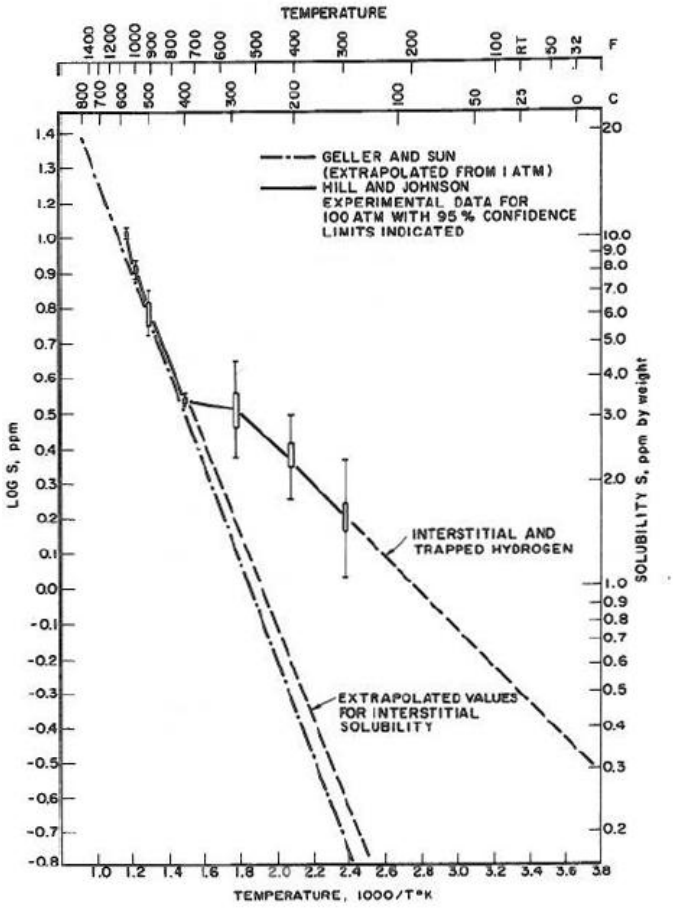

Figure 3: Solubility Curves for Hydrogen in Iron.
Note how the existence of traps increases solubility well beyond the linear extrapolation**.**

Hydrogen removal – the time required to remove a certain fraction of residual hydrogen from a part - is proportional to the thickness squared for plates (r^2 for cylinders) and inversely proportional to diffusivity (9). As temperature is increased, diffusivity increases dramatically since it is exponential with temperature. The only caveat to increasing the temperature is that, because of austenite's high solubility and low diffusivity, hydrogen removal may be retarded as temperatures near ferrite-austenite phase transition region. For particularly large parts, including forgings, reactor vessels,

and weldments, H removal poses a particular challenge because of the removal time being proportional to t^2 or r^2.

Though hydrogen in water is only weakly absorbed, hydrogen ions from acids are strongly absorbed. In addition, materials such as S, P, As, Se, Te, Sb, and CN can be included in the solution to promote uptake (9; 10; 11; 12). They are often referred to as "poisons" due to the fact that they increase the rate of hydrogen uptake and embrittlement. Hirth reports that O, N, and others can act as inhibitors (10), reducing hydrogen ingress. Therefore it may be beneficial to study the effects of bubbling and forced convection of O_2 or N_2 gas on hydrogen embrittlement in a standard solution. Under sufficiently high temperatures (> 200^{o}C) it is possible for internal decarburization (more formally called "hydrogen attack") to occur by methane bubble formation (9; 13). These methane bubbles exert hydrostatic pressures that promote crack and void growth. Hydrogen attack has been observed in the petrochemical and ammonia industries for some time.

Higher strength materials are more sensitive to HE because the ability to sustain higher loads around a flaw also increases the stress gradients around the notch tip – increasing the ability of hydrogen to diffusive towards the notch and lowering the strength of the material. The tendency for high energy shear failure decreases with increasing strength, also increasing the likelihood of a low-stress failure. As strength increases, the onset of plasticity increases as well. Plasticity relieves stress around a notch or flaw and localizes deformation to a specific region. Since higher strength means higher elastic limits, the stress is more uniformly distributed, and allows for a higher chance of activating a flaw causing elastic failure (with or without HE effects).

For low strength steels (<700MPa yield strength) in sulfide environments, blistering occurs around the void space of an inclusion and is observed as a bubble on the surface of the steel (usually indicating sub-surface cracking). This is often referred to as blistering. Blistering is promoted by a banded microstructure where inclusions are aligned in parallel plane. A banded microstructure is the result of Mn microsegregation during solidification. After hot rolling, the Mn-rich regions become stretched along the rolling direction, and upon slow cooling, stabilize the austenite phase, resulting in carbon-rich regions of austenite. When temperature becomes sufficiently low, the C-rich austenite transforms to pearlite, yielded the banded structure of C-rich pearlite and C-free ferrite. The void spaces present are small pockets of gas. As they expand, they act as highly localized crack fronts within the metal. This behavior then implies that there is a microstructural preference for fracture (at least in specific instances). However, voids can be closed by deformation processes such as hot rolling. If broken up into very small voids, the surface tension increases the gas solubility from the Gibbs-Thomson pressure:

$$P = 2\gamma/r \qquad [3]$$

γ is the surface tension and r is the void radius (14).

Perhaps one of the greatest challenges in hydrogen embrittlement is the fact that no single theory can explain all observed failure phenomena. It is universally accepted that hydrogen damages steel and can cause premature failure. However, the mechanism(s) by which failure occurs are not only highly debated, but vary from experiment to experiment based on the material in question (12; 15). In high purity nickel and iron, for example, the predominant mechanism of fracture is hydride formation and cleavage. Brittle metal hydride intermetallic particles that are thermodynamically

stable form near the crack tip, with additional stability provided by a triaxial stress state. At a critical stress, the particles break, causing a crack to form or propagate, leading to catastrophic failure.

In mild steel, however, significant ductility can be observed around the crack tip at small scales and can result (counterintuitively) in premature fracture, as proposed by Birnbaum (15). This mechanism is known as hydrogen enhanced localized plasticity (HELP). Atomic hydrogen diffuses into the crack tip and is able to reduce the stress field caused by a single dislocation, therefore reducing the long-range interactions between multiple dislocations. As a result, fracture at a crack tip is supposed become a highly localized ductile process rather than a brittle fracture. Shortly before Birnbaum proposed the HELP mechanism, J.P. Hirth performed a very complete review of hydrogen embrittlement in iron and noted that enhanced plasticity may not be able to model hydrogen-induced cracking by itself, but rather may be part of a larger mechanism that is responsible for hydrogen embrittlement (10).

Hydrogen transport in steel occurs by a variety of mechanisms (12). The primary mechanism is lattice diffusion, typical of any solid state diffusion process. Being the smallest atom, hydrogen in interstitial sites will possess a relatively high diffusivity value. Hirth cites a room temperature diffusivity of 1.2×10^{-4} cm^2/s and a corresponding activation energy of 6.88kJ/mol (0.0714 eV/atom). However, dislocation-enhanced transport of hydrogen has been experimentally observed (15; 16; 17; 18), and therefore can promote hydrogen embrittlement with a sufficiently large hydrogen concentrations at the surface. Even residual surface stresses from machining can drastically affect hydrogen transport (11). This is a clear indicator of dislocations enhancing hydrogen

motion throughout the lattice. This is not true for all experimental instances though. For example, increasing the strain rate decreases the amount of hydrogen evolved from iron under deformation. Mobile dislocations within the lattice are able to drag the hydrogen, giving rise to the transport mechanism. However, at extremely high strain rates, the hydrogen lags behind the dislocation because it cannot keep up with the local strain rate, causing an apparent hardening (15).

While dislocations can aid in the transport of hydrogen, hydrogen can also be trapped by various features within the material. Atomic hydrogen can bind to a particular site within the material – carbides, grain boundaries, etc. The total amount of energy required to trap atomic hydrogen is referred to as the trap activation energy, E_a. The activation energy is further broken down into the binding energy, E_b, which represents the strength of the trap, and the saddle energy, Es, which is an indicator of the jump frequency. A schematic trap energy diagram from Lee and Lee is shown below (19).

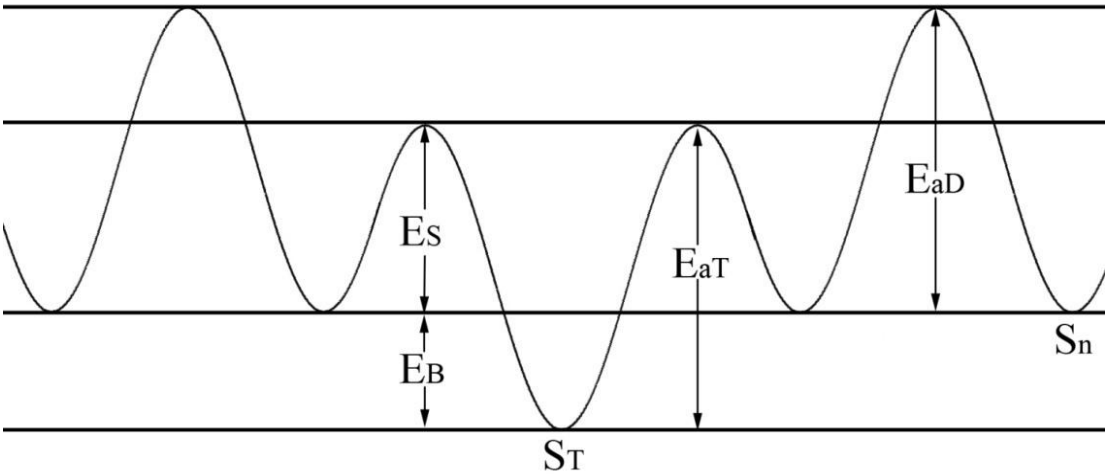

Figure 4: The Energy Diagram of a Hydrogen Trap.
The total energy of a trap is given by E_{aT}, the activation energy of the trap. This energy is split into the binding energy, E_B (strength of trap), and the saddle energy, E_S, (jump-frequency). E_{aD} is the diffusion activation energy, while S_n and S_T are the normal lattice and trap energies. Schematic recreated from Lee and Lee (19).

A number of authors have measured trapping energies of various traps, with Hirth (10) having one of the most complete sets of data. The table below includes not only Hirth's data collection (itself an aggregate of sources), but also includes data from more recent papers as well (10; 19; 20; 21).

Table 1: Energies for Various Hydrogen Traps

Reversible Traps (Ea < 40 kJ/mol)			
Trap Type	**Ea (kJ/mol)**	**Eb (kJ/mol)**	**Es**
H - perfect lattice	0	0	0
H-C	3.3	-	-
H-H	4.2	-	-
Lattice site	7.708	-	-
H-N	> 12.5	-	-
Grain Boundary	16.3 - 18.2	8.8 - 9.6	7.5 - 8.6
Cementite Interface	18.35	9.7	8.65
H - elastic dislocation	0-20.2	-	-
H-Ti	26-26.1	-	-
Dislocation	26.9	26.5	0.4
H - dislocation core (screw)	20-30	-	-
H - 0.5 H_2 vapor phase	28.6	-	-
Microvoid in CW Iron	35.15	29	6.15

Irreversible Traps (Ea > 40 kJ/mol)			
Trap Type	**Ea (kJ/mol)**	**Eb (kJ/mol)**	**Es**
Interface of Fe oxide	47.2	14.3	32.9
Austenite	55	-	-
Microvoid in 4340 Steel	56.2	-	-
H - dislocation core (mixed)	58.6	-	-
H - Grain boundary	58.6	-	-
H - AlN Interface	65	-	-
Interface of MnS	72.3	-	-
Interface of Al_2O_3	78.96	-	-
Interface of TiC	86.98	28.1	58.88

It is generally regarded that traps with activation energies below 40kJ/mol are referred to as "weak traps" or "reversible traps" and hydrogen is not particularly well bound to these sites. Traps with energies above 40kJ/mol, such as ceramic inclusions (oxides, sulfides, carbides, etc.) are considered "strong traps" or "irreversible traps" to which hydrogen is strongly bound. Based on various trapping energies, different metal microstructures should then give rise to different hydrogen embrittlement susceptibilities, purely from the ability to trap and retain hydrogen or allow it to remain mobile within the lattice structure. In an analysis of hydrogen trapping in various ultra-high strength steels, Pound (22) observed that the trapping in Aermet® 100, a high-alloy, precipitation hardening martensitic steel, changed as the microstructure changed from having MC-type precipitates (trapping constant, k = 0.44) to M_2C type (k = 0.66) after ageing temperatures of 270-370^{o}C and 482^{o}C respectively.

With an established base of theory and experimental observation, it becomes critical to take theory and derive models from which predictions can be made about hydrogen effects on the mechanical behavior of steel for structural analysis and accurately determining the lifetime of parts exposed to hydrogen. One of the most significant and fundamental models was proposed by G.M. Preyssoure and Bernstein in 1979 (23). The steel analyzed was an Fe-Ti alloy, in which Ti substitutional atoms, grain boundaries (GBs), and dislocations act as reversible traps while TiC particles act as irreversible traps at room temperature. Though cracks have often been observed nucleating at secondary phase particles along the grain boundaries, large, isolated particles appear best for crack nucleation. Fracture type – ductile, intergranular, or transgranular – is largely determined by solute distribution – elements like carbon,

antimony, silicon, and oxygen. If mobile interstitial solutes are removed, fracture becomes intergranular (which is interesting, because in the case of PH 13-8Mo, both trans- and intergranular fracture have been observed in HCl, however as previously stated, for sulfide environments the fracture mode tends to be largely intergranular. In their analysis, Preyssoure and Bernstein only considered intergranular fracture. As can be expected, H content depends on charge time, H concentration (fugacity/activity), and microstructural factors (types and number of traps). The Fe-Ti-C alloy examined contained ferrite, incoherent TiC particles, and Ti in substitutional positions, and was studied at varying Ti and C contents. In reversible traps (Ti, GB's, dislocations), a dynamic equilibrium exists the weakly trapped hydrogen and the diffusing hydrogen. An important result of the kinetics analysis of TiC trapping is that TiC sites may trap before the material reaches a saturated H level, both at the local and bulk level. In terms of diffusion behavior, this means that initially, external hydrogen flux cannot keep up with the TiC trapping rate, resulting in depletion of H from the GBs for a brief period of time. Once a critical hydrogen concentration is reached, however, cracking can occur through the grain boundaries (and in the model, it is assumed *only* grain boundary cracking occurs). It is suggested that for an irreversible trap (such as TiC) to be effective at limiting the extent of H-initiated damage, there must be a large number of particles available for trapping, a large number of H trapped per particle at saturation, or both. An increase in either of these quantities can delay the time between crack initiation and crack growth. On the other hand, reversible traps (substitutional Ti) can be beneficial by delaying the time for crack initiation once the critical hydrogen concentration has been reached (again, based on the model). This may be a result of hydrogen remaining mobile

within the alloy. To compare the model with experiment, Fe-Ti-C samples were mechanically and chemically polished, then cathodically charged in H_2SO_4 with CS_2 and As_2O_3 poisons added in the H_2SO_4 solution to facilitate H entry. Grain boundary cracking was determined using quantitative metallography on transverse cut sections with a 2% nital etch. Cracked boundary area was estimated by a random line intersection method (which appears to be similar to how grain size is measured). Their experimental results showed that increasing Ti content (reversible traps) significantly reduced the extent of grain boundary cracking as a function of time, as predicted from the theory presented. Furthermore, addition of C to form TiC lengthened the time between crack initiation and growth by almost a factor of 3. From their study, Preyssoure and Bernstein concluded that in order to promote resistance to hydrogen embrittlement, reversible traps must be fine, homogenously dispersed, and possess an activation energy Eb < 0.6 eV/atom (~36 kJ/mol). This would include solute atoms, low angle grain boundaries (LAGBs), and microvoids. For irreversible traps, they must be fine, homogenously dispersed, and possess Eb > 0.6 eV/atom (such as TiC particles under 1um with concentration greater than 10^{18} m^{-3}). Poor traps would include large, heterogeneously dispersed particles such as large, inconsistent TiC particles or high angle grain boundaries (HAGBs).

Modern micromechanics modeling is significantly more detailed than Preyssoure and Berstein's modeling performed over 30 years ago. Effects such as electrical potential around the crack tip – which can be significantly different from the remote, applied electric field – can be taken into effect. Gangloff and Lee modeled the effects of hydrogen on Aermet®100, a precipitation hardening ultra-high strength steel (24**).** Not

only were they able to analyze fracture morphology, but also were able use micromechanics modeling to understand material behavior in the fracture process zone (FPZ), which is the region about 10 microns ahead of the crack tip. They found that hydrogen was trapped strongly at martensite boundaries as well as hydrogen segregation. Depending on the precise microstructure of Aermet®100, it may be that small packets of austenite may form upon aging (as will be shown later for PH 13-8Mo). Reverted austenite at martensite boundaries could prove to be hydrogen "sinks" that promote brittle fracture.

As demonstrated above, there is clearly a large knowledge base on hydrogen. However, fractures from hydrogen embrittlement still cannot be predicted with precision, unlike traditional mechanics problems, which now have a solid foundation that can make extremely accurate predictions through modeling, such as finite element analysis. Thus, there is a need to contribute to the current body of hydrogen embrittlement knowledge by examining the effects of hydrogen on crack initiation in PH 13-8Mo, an aircraft-grade ultra-high strength steel.

The Microstructure of PH 13-8Mo

PH13-8Mo is a precipitation hardening (PH) martensitic stainless steel that is virtually carbon free, belonging to a class of steels known as maraging steels (typically Fe-Cr-Ni alloys). The nominal composition and of PH 13-8Mo given by Aerospace Materials Specification (AMS) 5629E is shown below (25):

Table 2: Composition of PH 13-8 Mo by Weight Percent

Al	C	Cr	Mo	Mn	N	Ni	P	S	Si	Fe
1.35	0.05	13.25	2.5	0.1	0.01	8.5	0.01	0.008	0.1	Bal

Heat treatment of maraging steels typically involves austenizing, allowing for most/all alloying elements to be dissolved into solid solution, followed by air cooling to below the martensite start (M_s) temperature. Depending on the specific composition and desired properties, a "quench" below the martensite finish (M_f) temperature may be necessary to complete the martensite phase transformation. Frequently, however, maraging steels complete the martensite transformation before reaching room temperature (26). Unlike the classic carbon steel, maraging steels do not rely on solution hardening to create a strong martensite phase or rapid cooling to avoid diffusional transformation reactions. The Continuous Cooling and Time-Temperature-Transitions Curves for a typical carbon steel can be observed below (27):

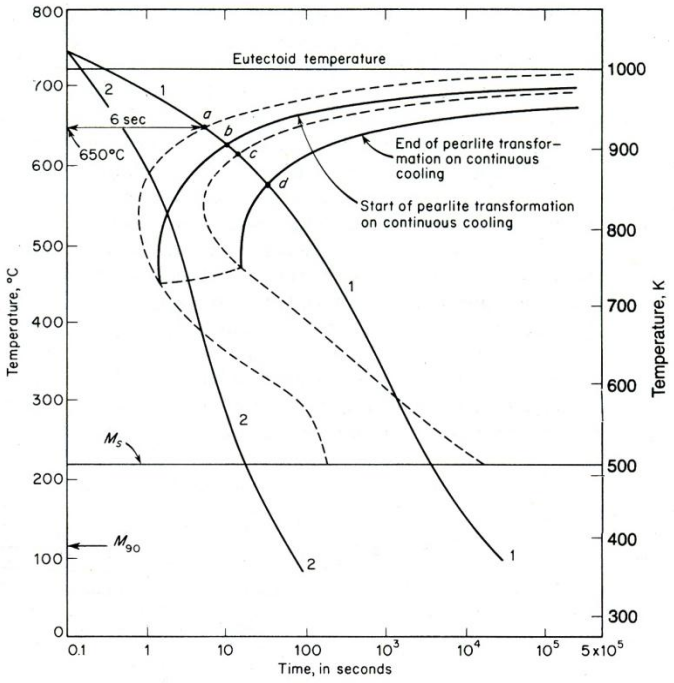

Figure 5: The Continuous Cooling Curve (CCC) for a Typical Carbon Steel.
Ferrite and pearlite form extremely quickly. A rapid quench is the only way to form martensite.
Image courtesy of Reed-Hill and Abbaschian (27).

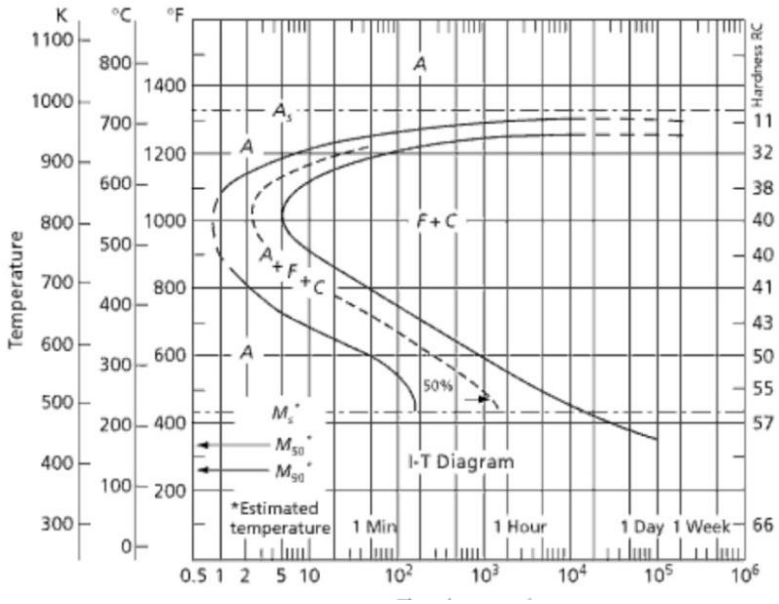

Figure 6: The Isothermal Time-Temperature-Transition (TTT) Diagram for a Typical Carbon Steel.
Again, illustrating the need for a rapid quench to avoid ferrite and cementite formation in carbon steel.
Image courtesy of Reed-Hill and Abbaschian (27).

The high percentage of substitutional alloying elements, particularly Cr and Ni, slow down diffusion and stabilize the austenite, eliminating the need for rapid cooling. This also helps avoid thermal stresses and deformations, particularly for large and/or complicated geometries. Because maraging steels are nearly carbon free, the martensite that is formed is actually quite soft (lower hardness, higher ductility) as compared to the martensite from a typical carbon steel. The high dislocation density resulting from the phase transformation provides a large number of nucleation sites for the precipitation of intermetallics upon heat treatment (26). The result is that a maraging steel precipitation *hardens* upon heat treatment, gaining strength while losing ductility and toughness, whereas a plain carbon steel precipitation *softens* (precipitation of Fe3C, which is soft compared to the solution hardened martensite), sacrificing strength for increased ductility and toughness. In general, however, maraging steels tend to have much greater toughness values than carbon-steels of similar strengths. Typical toughnesses for aerospace grade maraging steels are on the order of 100 MPa-$m^{½}$, while a similar quench-and-temper carbon steel might possess toughnesses on the order of 50-70 MPa-$m^{½}$ (some Q&T steels can be as high as 100 MPa-$m^{½}$ though, such as Hy-Tuf®, which is a Q&T steel similar to 4340).

The specific heat treatment steps for PH13-8Mo, as given in AMS 5629E, are outlined below:

1) Austenize at 927^{o}C (1700^{o}F) for a minimum of 30 minutes
2) Air cool to below 16^{o}C (60^{o}F)
3) Age for 4hrs at 510, 538, 552, 566, 593, 621^{o}C (900, 1000,1025,1050,1100,1150^{o}F) depending on desired properties.

4) Air cool to room temperature

It is common notation for a specific heat treatment to be referred to as the "H" condition, ex ageing Ph 13-8Mo at 1000^{o}F would be the "H1000" condition while ageing at 1150^{o}F would be designated the "H1150" condition.

The resulting mechanical properties of the aforementioned heat treatments are given in the table below (note, toughness values are not covered by AMS 5629E):

Table 3: Mechanical Properties of PH 13-8 Mo

Condition	**Ultimate Tensile Strength (MPa)**	**Yield Strength (MPa)**	**Elongation** (%)**	**Reduction in Area** (%)**	**Fracture Toughness (MPa-m^{½})**
Solution Annealed (SA)*	1040	650	-	-	-
H950 (Aged 510C)	1517	1413	10(L), 10(T)	45(L), 35(T)	-
H1000 (Aged 538C)	1413	1310	10(L), 10(T)	50(L), 40(T)	99***
H1025 (Aged 552C)	1276	1207	11(L), 11(T)	50(L), 45(T)	-
H1050 (Aged 566C)	1207	1138	12(L), 12(T)	50(L), 45(T)	-
H1100 (Aged 593C)	1034	931	14(L), 14(T)	50(L), 50(T)	-
H1150 (Aged 621C)	931	621	14(L), 14(T)	50(L), 50(T)	-

*data from Ding et al; not governed by AMS 5629E (28)

**(L) = longitudinal, (T) = transverse specimen orientation

***data from MMPDS. Other toughness values not available (29)

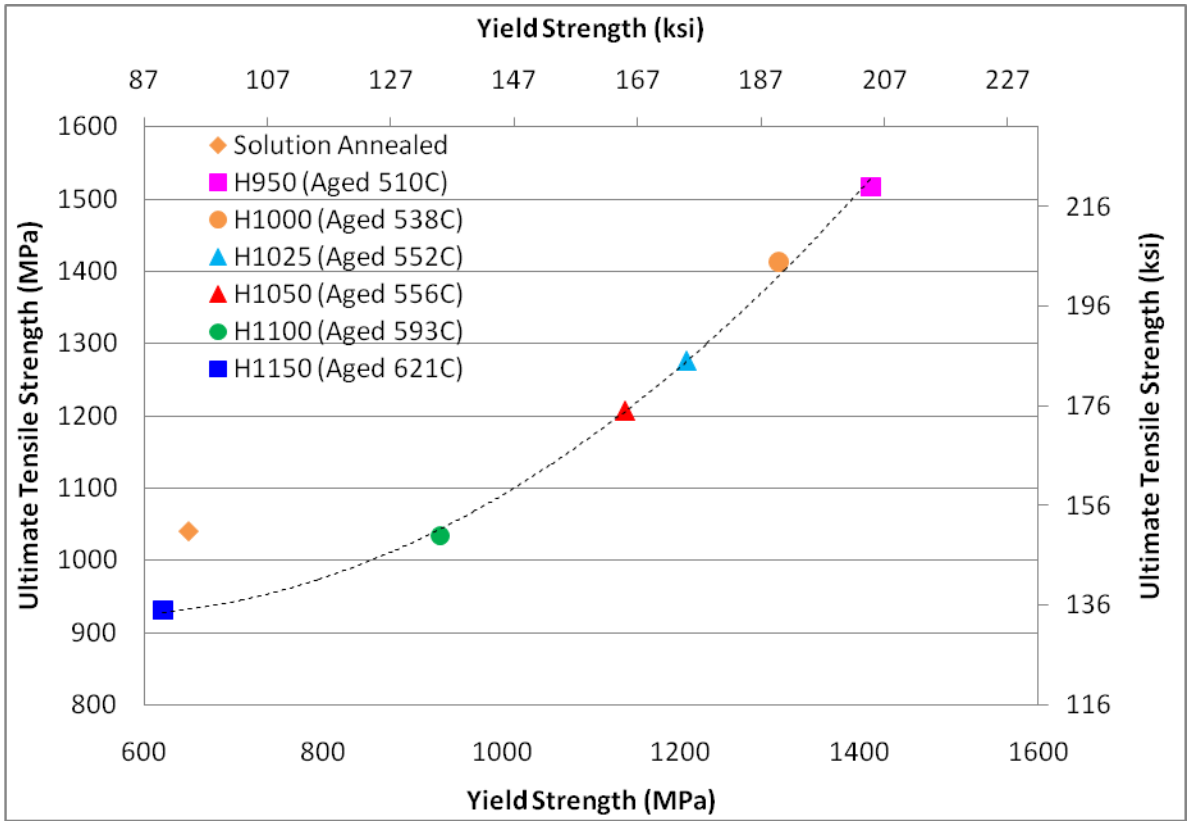

Figure 7: Yield and Ultimate Tensile Strengths for PH 13-8Mo in Different Heat Treatments.

Aluminum acts as a precipitate former, and molybdenum aids in high-temperature stability. Because of its high percentage of alloy content and low carbon content, the traditional iron-carbon phase diagram does not correctly describe the equilibrium phases present in the alloy. Delong et al. developed a phase diagram of the nickel-iron system for weldments. While the cooling rate in a weldment is not identical to those experienced by PH 13-8Mo under air cooling, their diagram is nonetheless useful in estimating which phases should be present and in what quantity (30):

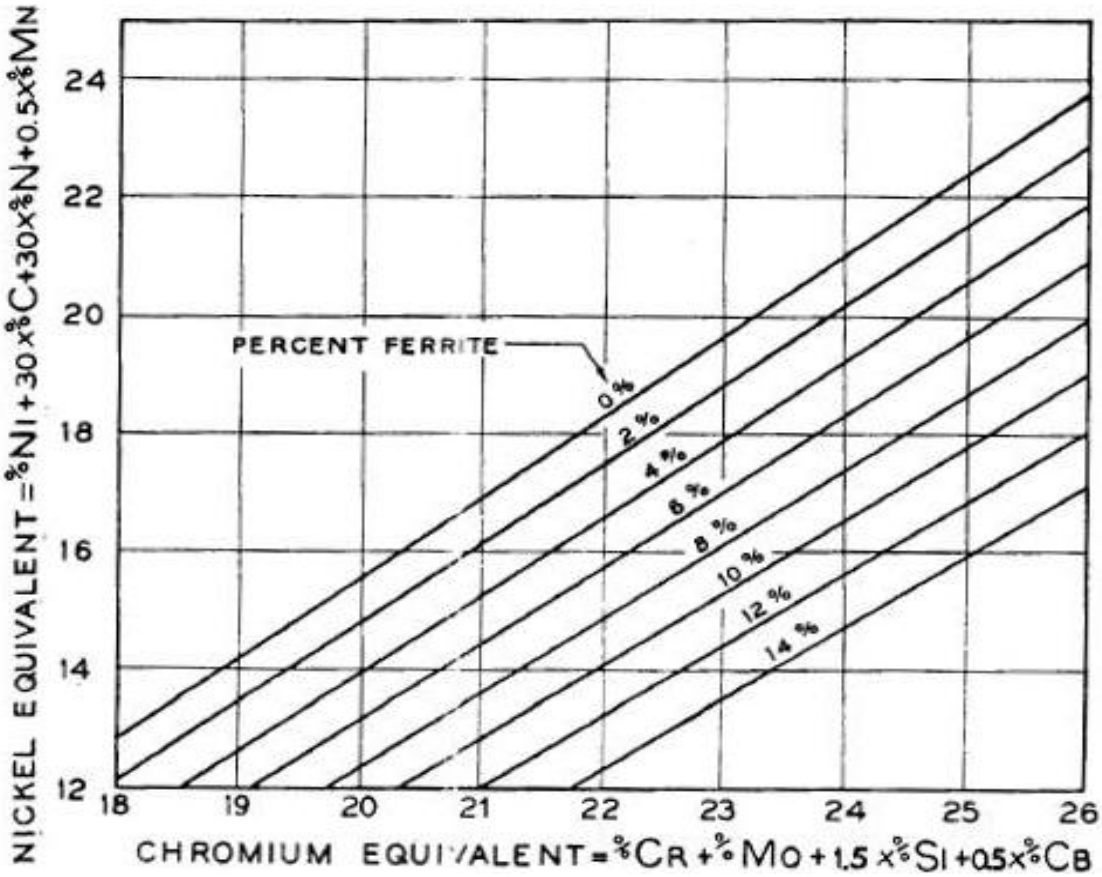

Figure 8: The Delong Phase Diagram for Stainless Steel Welds.
Image courtesy of Delong et al **(30)**.

Seetharaman et. al performed a microstructural analysis of PH 13-8Mo using optical and electron microscopy (4). In the solution annealed condition, PH13-8Mo is entirely BCC lath martensite with a lath thickness of approximately 0.25 µm. In the heat treatment range of 425°C to 500°C, nm-scale coherent NiAl particles precipitate within the laths. At ageing temperatures above 525°C, appreciable amounts of FCC austenite begin to form. Above 625°C, non-coherent Ni_3Mo/Ni_4Mo particles precipitate at grain boundaries and even larger amounts of austenite are formed as ageing time or temperature increase. Metallographic and TEM images below from Seetharaman et al show the microstructure of PH 13-8Mo at the various heat treatment conditions.

Metallographic images from the samples in this study are also shown for comparison with the work done by Seetharaman et al.

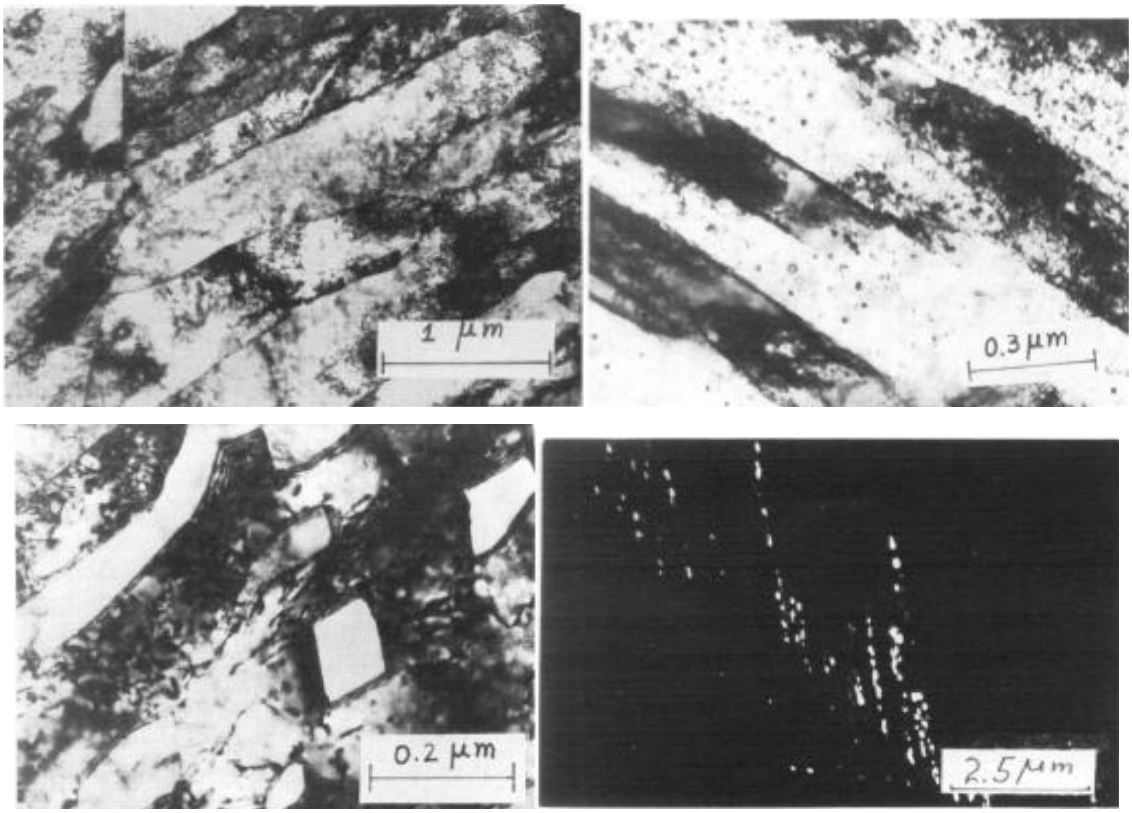

Figure 9: Transmission Electron Microscope Images of PH 13-8Mo from Seetharaman et al. These images detail the lath and precipitate structure of PH 13-8Mo. SA condition (top left), H1000 (top right), H1150 (bottom left; bottom right)In the dark field image of Fig 9, only a handful of precipitates show because they are the only ones satisfying the Bragg diffraction conditions.

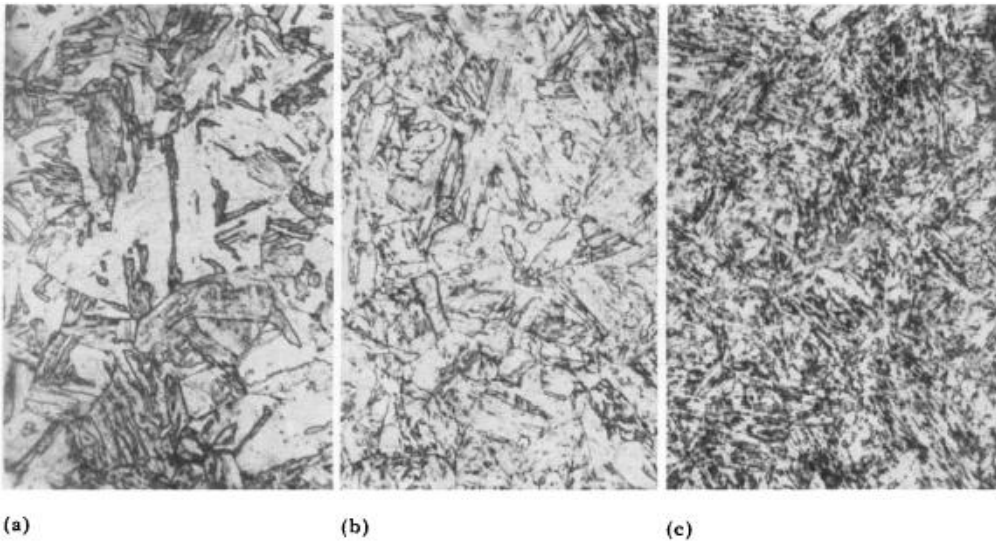

Figure 10: Optical Micrographs of PH 13-8Mo in Various Heat Treatments at 500x
Increasing the ageing temperature from a) 425°C to b) 525°C to c)600°C tends to produce finer precipitates over short periods of time. The larger number of precipitates at 600°C makes identification of individual martensite laths significantly easier. Images courtesy of Seetharaman et al (4)

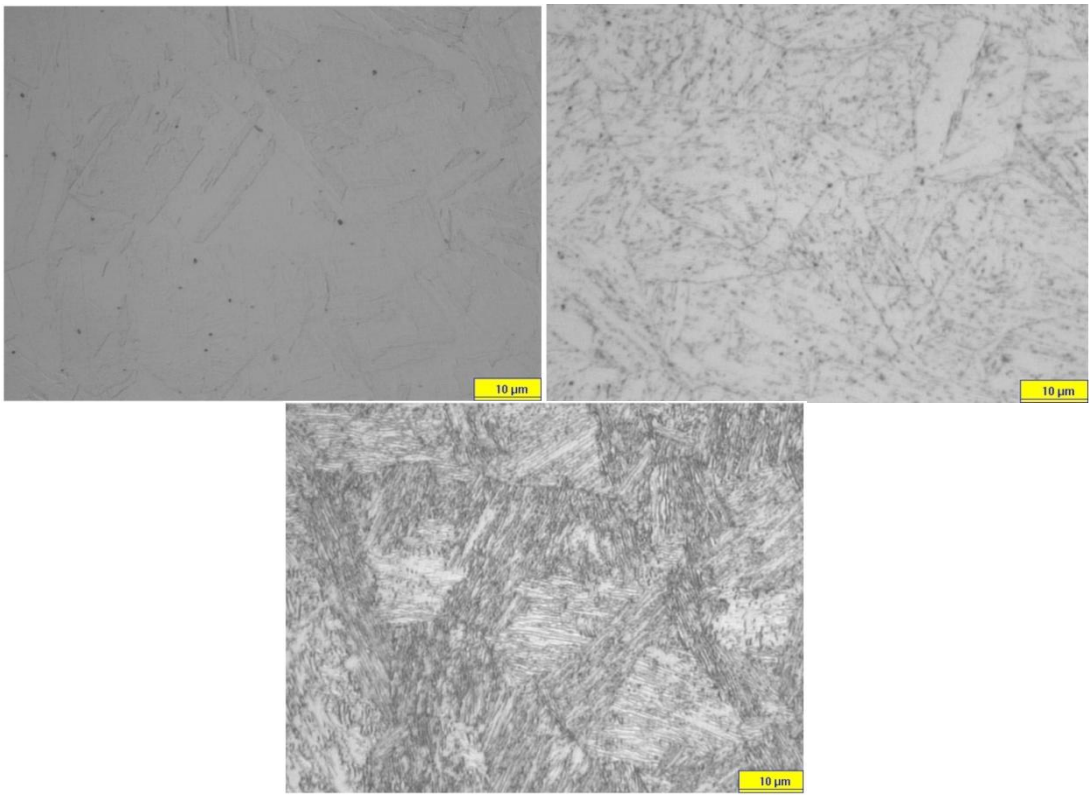

Figure 11: Metallographic Images of PH 13-8Mo from This Study.
Solution annealed (top left), H1000 condition (top right), H1150 condition (bottom center).

Hydrogen Embrittlement in High Strength Steels and PH13-8Mo

Hydrogen embrittlement (HE) has long been problematic in steels, as evidenced by research pertaining to it with respect to the petrochemical and nuclear industries. As metallurgy and alloy developments have continued to improve, so too has understanding the problem of hydrogen embrittlement. Research has shown that the susceptibility of steel to hydrogen embrittlement generally scales with increasing ultimate tensile strength (31). Thus, advances made by the development of more modern steels critical for progress in naval aviation systems – high strength, high toughness alloys– have been largely mitigated by hydrogen embrittlement (2; 24) since component failures continue to occur. A strong research community has developed to address the need of understanding hydrogen not only in steel in general, but particularly in high strength and ultra-high strength steels (UHSS) where mechanical failure of a single component is extremely costly. One of the greatest challenges in modeling and predicting effects of hydrogen on the mechanical behavior of steel is the fact that the microstructure, processing, and properties of steel cannot be decoupled from one another. For example, overageing steels tends to reduce susceptibility to HE (28; 31). For PH 13-8Mo, would this result be due to the loss of martensite, the growth of austenite, or the direct loss of strength? These effects cannot precisely be decoupled for the alloy because the loss of martensite is accompanied by austenite growth, and the soft austenite reduces strength. At the same time, the precipitate composition changes from NiAl to Ni_3Mo/Ni_4Mo. Changing the microstructure changes the properties. Complications such as these make it difficult for metallurgists and engineers to determine which microstructural and property features contribute the most towards resistance or susceptibility to hydrogen embrittlement.

Hydrogen embrittlement presents itself in a variety of corrosive and embrittling environments including water, hydrogen gas, cleaning solutions, and acids. Exposure to all of these environments may occur during the life of an aircraft component either while in service or during repair, though some environments are more aggressive than others (31). Acids are known to be particularly damaging to steels, and the effects of hydrogen can be further exacerbated by the addition of "poisons" such as arsenic which promote hydrogen ingress into the steel.

Tsay et al have characterized PH 13-8Mo in several different environments including pure hydrogen gas and hydrogen sulfide gas (28; 32; 33). Compared with gaseous embrittlement, sulfide stress corrosion cracking (SSCC), a specific manifestation of hydrogen embrittlement, is much more severe due to the liquid, as opposed to gaseous, H-rich environment (consequently, one would also expect a hydrochloric acid environment, used in this study, to be more damaging than pure H_2 gas). The formation of austenite is known to improve resistance to SSCC as well as HE in general. Compared to other PH steels at similar strength levels, PH 13-8Mo is more resistant to HE, which may be a result of its higher austenite content. Though no comprehensive source of HE data exists where environments and test methods are uniform, Carter et al assembled a table of stress corrosion cracking (SCC) threshold values for a variety of steels under standard salt solution (3.5% NaCl) (34). Several newer alloys have been added to the table by the author (threshold values taken from MMPDS)

Table 4: K_{ISCC} and Strength Level Comparison of Various Steel Alloys

Alloy	Heat Treatment	Yield Strength (MPa)	Ultimate Tensile Strength (MPa)	Elongation (%)	K_{IC} (MPa-$m^{1/2}$)	K_{ISCC} (MPa-$m^{1/2}$)
*17-7 PH	RH 950	1181	1286	11	36	< 21
	TH 1050	-	1360	9	43	17.4 ± 1
*PH 15-7Mo	RH 950	1355	1513	12	35	15.4 ± 2
	TH 1050	1157	1229	11	37	20.4 ± 2
*AM 355	SCT 850	1241	1472	17	65	36 ± 3
	SCT 1000	1180	1227	19	97(1)	97(2)
	Modified SCT 1000	1125	1196	18	129(1)	129
*AM 362	H 900	1358	1382	11	33	14 ± 2
	H 1000	1207	1233	14	44	34 ± 3
*AM 364	H 850	1264	1301	15	144(1)	102 ± 8
	H 950	1287	1320	15	141(1)	141(2)
*17-4 PH	H 900	1217	1342	14	57	56.5(2)
	H 1000	1089	1118	15	131(1)	131(2)
*15-5 PH (air melted)	H 900	1207	1349	16	106(1)	88 ± 2
	H 1000	1089	1114	16	125(1)	125(20
*15-5 PH (vacuum melted)	H 900	1206	1320	14	82	62 ± 4
	H 1000	1087	1123	15	132(1)	132
*PH 13-8Mo	H 950	1431	1552	14	81	81(2)
*Custom 455	H 950	1696	1703	11	79	79(2)
**AF 1410 (plate/billet)	not specified	-	-	-	-	25
**AF 1410 (bar)	AMS 6527D	1482	1620	12	143	52
**0.20C mod AF 1410	not specified	-	-	-	-	24
***Aermet® 100	H900	1710	2030	14	115	23

Table 4: K_{ISCC} and Strength Level Comparison of Various Steel Alloys (Continued)

***300M	575°F 2x Temper	1650	2000	8.5	55	16
***4340	450°F Temper	1670	1940	10	48	13
***Custom 465	H1000	1690	1740	13	99	> 59

*Data from Carter et al
**Data from MMPDS; KISCC estimated from MMPDS-04 Figure 2.5.0.2
***Data from E.U. Lee et al. (35)
(1) KIC test not valid
(2) No SCC growth at K levels below 85% KIC
(3) Values taken from MMPDS; presented as "typical" value.

As can be seen from the table above, PH 13-8Mo, along with other alloys such as Custom® 455 and 465, possess considerable resistance to SCC.

Hydrogen is more soluble in austenite compared to ferrite, but has a lower diffusivity. Tsay et al measured this effect by comparing the diffusivities of hydrogen in PH 13-8Mo across various heat treatments. Their results are shown below (32):

Table 5: Room Temperature Hydrogen Diffusivities and Concentrations in PH 13-8Mo

	H800	**H900**	**H1000**	**H1100**
D_{eff} ($m^2\ s^{-1}$)	2.44×10^{-12}	2.4×10^{-12}	2.2×10^{-12}	2.48×10^{-13}
$J_\infty L$ ($mol(H)\ s^{-1}\ m^{-1}$)	1.1×10^{-9}	1.19×10^{-9}	1.16×10^{-9}	7.35×10^{-10}
C_{app} ($mol(H)\ m^{-3}$)	450	500	530	2960

Notice that the (effective) diffusivity and concentration of hydrogen stay relatively constant from the H800 through H1000 conditions. Upon aging to H1100, however, *diffusivity* drops by one order of magnitude and *concentration* increases by nearly a factor of six. This may partially explain why higher austenite contents are

beneficial for resistance to hydrogen embrittlement. However, austenite is a "soft" phase and reduces alloy strength – thus there is a tradeoff between in-service strength level and HE resistance. A possibility of testing these effects would be to vary the Ni content within the steel – doing so would cause reverted austenite to become stable at lower aging temperature, where peak strength is typically achieved – allowing material strength and austenite content to be separated better. In gaseous H_2, Tsay et al used Notched tensile (NTS) bars and compact-tension (CT)specimen and compare susceptibility and crack growth rates of different heat treatments of PH 13-8Mo (28). NTS specimens were also drawn in H_2S (32). Under the pure hydrogen gas environment, results showed that the loss of NTS decreased as the ageing temperature was changed from the peak-age temperature, i.e., the H800 and H1000 samples were less susceptible than H900 (peak-aged) and the H1200 and SA condition samples were even less susceptible than H800 and H1000. The loss of NTS followed the UTS level – specimen with lower UTS values had less NTS loss (reinforcing the fact that HE susceptibility decreases with lower UTS), as shown in Tsay's figure below (28):

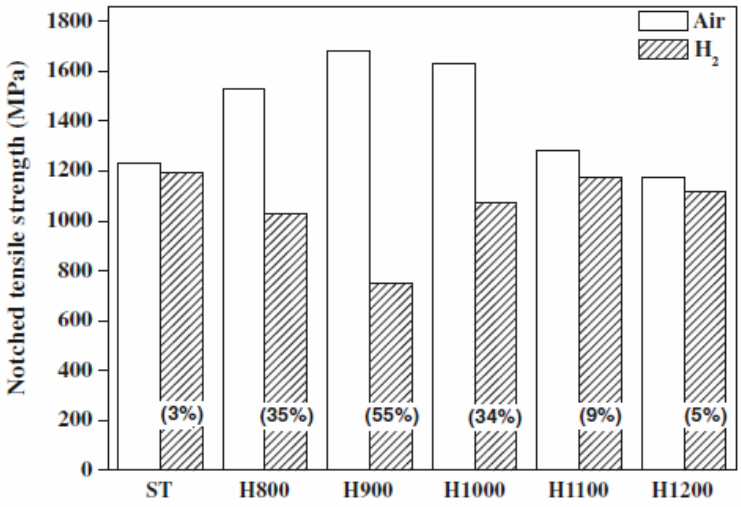

Figure 12: Notched Tensile Strength (NTS) Reduction of PH13-8Mo in H_2 Gas.
Note that NTS loss is reduced as the absolute NTS level drops, regardless of austenite content.
Image courtesy of Tsay et al (28).

The CT specimens used for fatigue crack growth rate (FCGR) analysis showed that the crack growth rate, da/dN, increased with increasing strength level. The crack length is a and N is the number of cycles at constant stress intensity range. For similar yield strength levels, the overaged samples (H1100 and H1200) had lower FCGR's than their underaged (H800 and A condition) counterparts. Tsay concluded that the austenite in the overaged specimen is able to resist planar slip, reducing the FCGR. This is sensible since lath martensite is BCC and cross slip is unfavorable between BCC and FCC systems. In addition, any plastic work under fatigue crack growth will be localized to the crack tip due to the large stress intensity factor around the root of the crack.

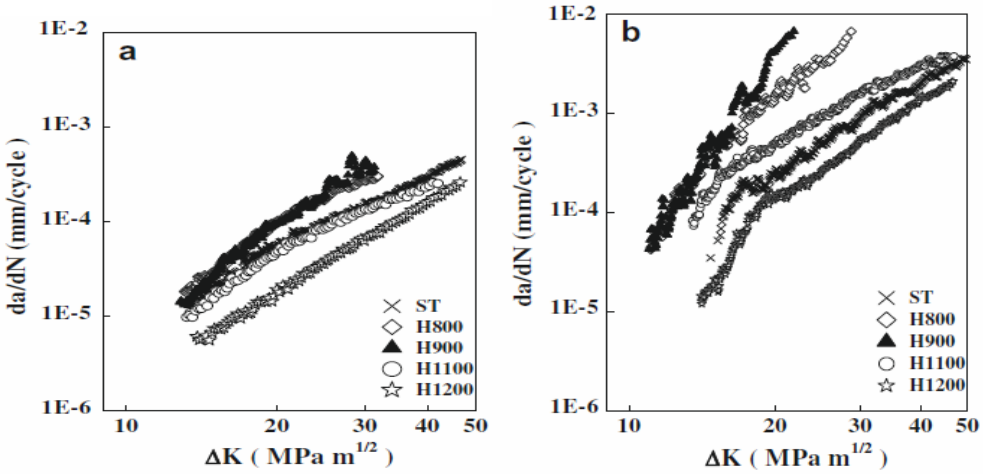

Figure 13: Fatigue Crack Growth Curves of PH 13-8Mo in Air (left) and Hydrogen (right). Crack growth rates are increased considerably for all specimens under the H2 environment. Image courtesy of Tsay et al (28).

Fatigue crack growth is often described by the Paris Law relationship (5):

$$\frac{da}{dN} = C\Delta K^m \qquad [4]$$

In the Paris Law, *a* is the crack length, *N* is the number of cycles, *C* (sometimes also listed as A) is the Paris Law coefficient, *ΔK* is the amplitude of the stress intensity level (Kmax – Kmin), and *m* is the Paris Law exponent. The Paris Law is frequently plotted on a log-log scale, where *m* becomes the slope of the line and *C* becomes the intercept. C(T) specimen were fatigued inside a stainless steel chamber into which the hydrogen gas was introduced. Under the hydrogen environment, da/dN curves showed extremely high Paris Law coefficients for the H800 and H900 conditions while the H1200 condition had significantly lower coefficient than the SA (listed as ST by Tsay) condition. Based on what has been stated so far, it would be expected that both the H1100 and H1200 conditions perform better than all other treatments as a result of the high austenite content, which the SA(ST), H800, and H900 conditions lack. However, it is somewhat surprising that, going from fatigue in air, where the H1100 and H1200 have

the two lowest growth rates, to the hydrogen environment, that the SA (ST) condition has a lower fatigue crack growth rate than the H1100 condition, but not the H1200 condition. In addition, crack growth rates for the H800 and H900 are relatively similar in both air and hydrogen (except in H_2 below $\Delta K \sim 15$ MPa $m^{½}$). It is quite evident that microstructure – not just strength – plays a significant role in determining the resistance of a material to environmentally assisted crack growth.

H transport around the crack tip is predominantly supported by mobile dislocations. High strength steels typically have small plastic zones, meaning critical stresses and H concentrations can be reached relatively quickly. It would be interesting to test materials with similar ultimate tensile strengths (since susceptibility tends to increase with UTS) but different plastic zone sizes or vice versa – different UTS levels but similar plastic zone sizes (given by the ratio $\left(\frac{K_{IC}}{\sigma_y}\right)^2$) - to test these effects. Because of the structure-property-processing triangle, we again would run into the fact that microstructure, processing, and properties cannot be *perfectly* decoupled. Another possibility is to compare the effects of hydrogen on two steels of similar strength but different dislocation density. In the case of PH 13-8Mo, this might be achieved by using the material in the H900 and H1000 condition and rolling them to similar UTS levels. Due to its lower strength after aging, the H1000 condition would require a higher degree of rolling, and presumably achieve a larger dislocation density for an equivalent UTS level. Low diffusivity in lower strength specimens (partly a result of lower dislocation densities in PH 13-8Mo) implies that a critical stress or H concentration cannot be reached as easily, improving resistance to HE.

Notched tensile strength testing by Tsay in H_2S showed similar behavior to that in pure gaseous H_2 – the under- and overaged specimens had reduced NTS loss compared with the peak-aged samples, and as the overageing temperature increased, so did the reduction in NTS loss. The SA condition was not tested under H_2S, however. Unlike pure hydrogen embrittlement, where fracture mode is found to be mixed between inter- and transgranular fracture, sulfide stress corrosion cracking tends to be largely intergranular with some transgranular fracture. If two alloys require identical H concentrations within the plastic zone to induce cracking, Tsay argues that permeation should then be an indicator of hydrogen embrittlement sensitivity (32). In PH 13-8Mo, it is reported that dislocations are the primary source of weak hydrogen traps (33), with the coherent NiAl precipitates acting as secondary weak traps. The apparent solubility is highly dependent on both the type of traps (strong vs weak) and their concentration. As aging temperature increases, recovery reduces dislocation density, reducing the number of weak dislocation traps. However, growth of reverted austenite increases the amount of strong traps. The effects are seen in the diffusivity and solubility data, where the H1100 condition 13-8Mo has a room-temperature diffusivity one order of magnitude less than lower temperature heat treatments and a solubility of hydrogen that was greater by a factor of six (see Table 5 above). Austenite is known to be a strong trap and able to sustain significantly higher concentrations of atomic hydrogen than ferrite as a result of its higher solubility (see Figure 2 – the Iron-Hydrogen Phase Diagram).

As a result of the high solubility and low diffusivity in austenite, Tsay inferred that austenite will inhibit transport of hydrogen to a crack tip, rendering the H800, H900, and H1000 conditions more susceptible to HE than the H1100 condition.

Furthermore, Tsay et al. compared the HE resistance behavior of PH 13-8Mo with that of another high strength steel – T200 Maraging, also a precipitation hardening steel. T200 Maraging is similar to PH 13-8Mo in that it is a martensitic precipitation hardening steel. The precipitates that form upon aging are of the form $(NiFe)_3(TiMo)$ and, also like PH 13-8Mo, forms reverted austenite as aging temperature/times increase. For comparison, the composition and properties are given below, as reported in Tsay's study (33):

Table 6: Composition of PH 13-8Mo and T-200 Maraging as Reported by Tsay et al (33)

Alloy	Cr	Ni	Mo	C	Si	Mn
PH 13-8Mo	12.56	8.11	2.12	0.05	0.04	0.05
T-200	-	18.84	2.85	0.02	0.075	0.023

Alloy		P	S	Al	Ti	Fe
PH 13-8Mo		0.006	0.003	1.07	-	Bal
T-200		0.005	0.003	-	0.8	Bal

Table 7: Mechanical Properties of PH13-8Mo and T-200 Maraging as Reported by Tsay et al (33)

Sample	Ultimate Tensile Strength (MPa)	Yield Strength (MPa)	Elongation (%)	Rockwell Hardness (HRC)
PH13-8Mo (SA)	1195	832	14	34.4
PH13-8Mo (H1200)	956	825	18	31.6
T-200 (SA)	904	814	15	28
T-200(H1200)	1035	887	14	31.2

Notched tensile strength was measured for both alloys in the solution annealed (SA) and overaged conditions (both aged at $650^oC/1200^oF$), under air and H_2S environments. For the H_2S environmental testing, two displacement rates were used – 0.0075mm/min and 0.0015 mm/min. It was found that a slower displacement rate

increased the reduction in NTS. This can be commonly observed in other time-dependent tests: the slower the displacement or loading rate, the longer hydrogen has to diffuse into the sample and the better it is able to be transported by mobile dislocations, resulting in reduced values of NTS. As compared to their respective SA conditions, both the overaged conditions of PH13-8Mo and T200 had significantly higher values of retained notched tensile strength under the H2S environment. For PH 13-8Mo, the H1200 condition lost 53% of its NTS while the SA condition lost 74% in H_2S (0.0015 mm/min). For the T200 Maraging steel under the same displacement rate, the overaged sample lost 63% of its NTS, while the SA sample lost 73% of its NTS. Though both alloys consist largely of martensite, PH 13-8Mo does form appreciable amounts of austenite when overaged, which may contribute to its better performance compared to T200 in a hydrogen-rich environment. Room temperature effective diffusivity in 13-8Mo was reduced by a factor of about 10 upon overaging, but only by a factor of 2 in T200, as measured by the permeation technique (details can be found in Devanathan and Stachurski's original paper of hydrogen transport in palladiium (33); Pound used a potentiostatic pulse technique in his experiments on Aermet®100 (22). Conversely, the effective solubility of hydrogen was much higher in 13-8Mo H1200 than T200 in the overaged condition, as a result of higher austenite content. However, because of T200's higher ductility, there should also be more blunting of a crack/notch tip and a decrease in the stress intensity factor at the notch tip, thereby reducing the transport of hydrogen to the strained region around the crack tip due to reduction in triaxial stresses.

Microstructure is not the only determining factor for steel susceptibility, however. Processing effects can change hydrogen behavior dramatically. Murray et al. tested the

effects of surface condition on HE susceptibility in PH 13-8 Mo (11). Two groups of smooth bar tensile specimen were cathodically charged in 10% H_2SO_4 with As_2O_3 poison (the only difference between the two being the place of machining). After charging, the samples were loaded with a dead weight until failure occurred (which was observed to be largely intergranular; consistent with work from Tsay et al. in an H_2S environment, as well as the work performed herein). The first group possessed a well defined threshold stress of 40% yield after 170hours (1 week). The second group did not exhibit a threshold stress in the time allotted for the testing. SEM analysis of specimens from this second group revealed that sub-surface cracks formed as a result of tooling dragging along the specimen surface during the machining process. Thus, even small amounts of surface damage can significantly amplify the effects of hydrogen embrittlement. For both groups, the brittle fracture zone size was found to be proportional to $t^{½}$, indicating a diffusion-limited process of failure. The apparent diffusivity (it was not actually measured) compared to that given by other work, such as Hirth's (10), was significantly less due to surface traps and other effects. Hirth's room temperature diffusivity value of 1.2×10^{-4} cm^2/s predicted a saturation time of roughly 5 minutes, but the experimental work took greater than 8 hours. Thus, traps can be highly effective at limiting hydrogen diffusion from the exterior for an uncracked, smooth tensile bar.

One of the weaknesses of current data and literature with respect to PH 13-8Mo is that the majority of the data only presents relative measurements. Most tests involved relative measurements such as notched tensile strength (NTS), hydrogen permeability/solubility, and analysis of hydrogen trapping constants. While Tsay did perform some fatigue crack growth analysis in H_2, the C(T) specimens used were not

designed to meet plane strain requirements. The crack growth rates may still be useful design values, but they are not the most representative since design criteria for high strength steel alloys in naval aviation relies on fatigue and fracture toughness data obtained under plane strain conditions. The work to be carried out in this thesis is based on an applied stress intensity, K_{app}. The value of stress intensity, introduced in linear elastic fracture mechanics (LEFM), is commonly used in the design and evaluation of flaw-sensitive structures. Unlike NTS or relative susceptibility measurements, the use of K provides data which can be utilized to design and model components where environmentally assisted cracking, particularly hydrogen embrittlement, is of concern. Searching through literature yielded no measured K-Life curves as shown in Figure 1, despite the schematic appearing in a variety of sources.

Linear Elastic Fracture Mechanics (LEFM)

The origins of fracture mechanics begin with Griffith in the 1920's. He proposed that the energy required to grow a crack must be greater than or equal to the energy required to create two new material surfaces (5), relying on the conservation of energy from the 1st Law of Thermodynamics.

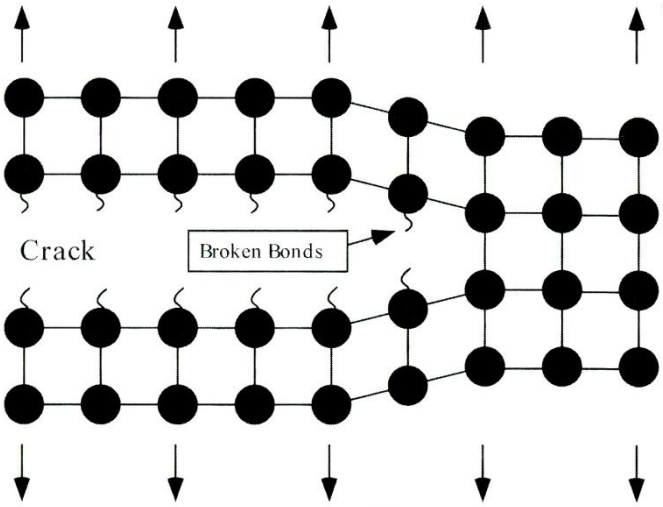

Figure 14: Schematic Diagram of a Griffith Fracture.
Image courtesy of T.L. Anderson (5)

$$\sigma_f = (2E\gamma_s / \pi a)^{0.5} \quad [5]$$

While this relation worked well for brittle materials (ceramics and glasses), it underestimated the fracture stress for metals. Irwin and Orowan later included a plastic work term into the Griffith equation in order to provide better agreement for metals (5):

$$\sigma_f = (2E(\gamma_s + \gamma_p)/\pi a)^{0.5} \quad [6]$$

The quantity in parentheses can be generalized to the work of fracture, w_f, in order to accommodate any energy dissipation mechanism (elasticity, plasticity, viscous effects, etc.). Irwin later introduced (1956) the energy release rate, G, describing the energy available for crack growth (5).

$$G = -d\Pi/dA \quad [7]$$

where Π is the potential energy and A is the crack area. When G reaches the critical level G_c, equal to the work of fracture, crack extension begins (5):

$$G = G_c = 2w_f \quad [8]$$

Depending on the material's resistance to crack growth, R, the extension may be unstable (catastrophic failure, dG/dA > dR/dA) or stable (incremental crack growth dG/dA ≤ dR/dA) as shown below:

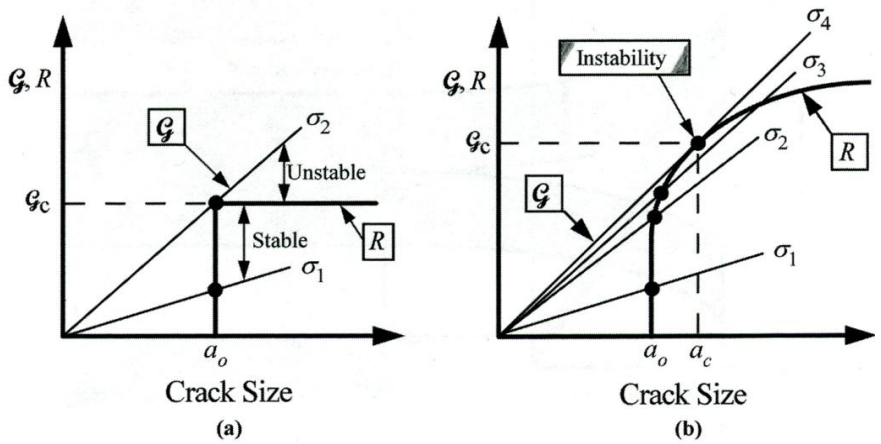

Figure 15: Resistance Curves (R-Curves) for Brittle(a) and Ductile(b) Materials.
Image courtesy of T.L. Anderson (5)

Though energy release rate provided a much better descriptor of cracked materials, the stress intensity factor, K, has become the dominant analytical tool. Introduced by Westergaard, Irwin, Sneddon, and Williams from 1940-1960, the stress intensity factor is used to describe the stress field around a crack in polar coordinates:

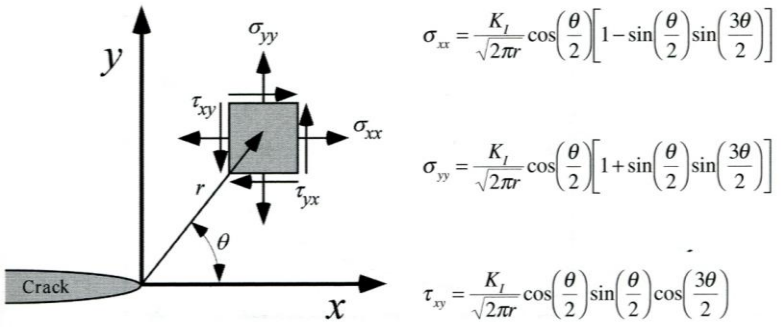

Figure 16: The Stress Field Around a Crack Tip.
Image courtesy of T.L. Anderson (5)

$$\sigma_{ij} = \frac{K}{\sqrt{R}} f_{ij}(\theta) + Ø \qquad [9]$$

Ø represents higher order terms of R that are ignored as r approaches 0. The stress intensity factor, K, describes how high the stress is at a crack tip relative to a material's plane strain fracture toughness K_C (in the same way that one would compare the applied stress, σ, to the yield or ultimate tensile stresses, σ_y and σ_{UTS}). Though there are three modes of failure – Mode I (tensile), Mode II (in-plane shear), and Mode III (out-of-plane shear) – typically the Mode I fracture toughness, K_{IC}, is used.

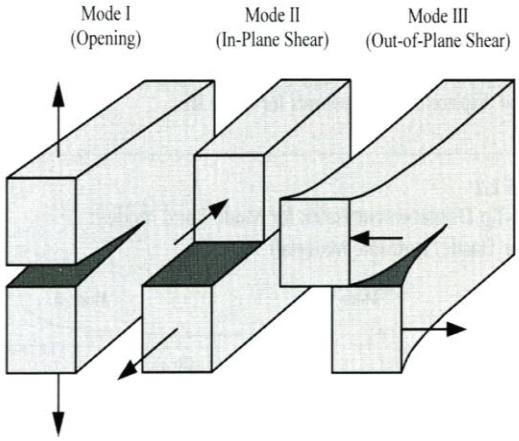

Figure 17: The Three Modes of Fracture.
Image courtesy of T.L. Anderson (5)

When the applied stress intensity equals the fracture toughness, the material is predicted to catastrophically fail. Because the severity of stress raisers (notches) depend on geometry, the generalized form of the stress intensity K is given by (5; 6):

$$K = Y\sigma\sqrt{\pi a} \qquad [10a]$$

Or

$$K = \frac{YP}{B\sqrt{W}} \qquad [10b]$$

Where K is the stress intensity, σ is the stress, a is the crack length, Y is the unitless stress intensity factor, B is the thickness and W is the ligament length. Y is usually expressed as a power series involving the ratio of the crack length (a) to another geometrically relevant length - typically the ligament length, (W), i.e Y = f(a/W). For the compact tension C(T) specimen used here, f(a/W) is given by (5; 6):

$$Y = \frac{2 + \frac{a}{W}}{\left(1 - \frac{a}{W}\right)^{\frac{3}{2}}\left[0.886 + 4.64\left(\frac{a}{W}\right) - 13.32\left(\frac{a}{W}\right)^{2} + 14.72\left(\frac{a}{W}\right)^{3} - 5.6\left(\frac{a}{W}\right)^{4}\right]} \qquad [11]$$

The loading of many fracture mechanics specimen, such as CT's, involves some degree of rotation, since there is a hinge point slightly behind the crack tip. Compliance methods are used to account for these effects, as well as the fact that the specimen is not perfectly rigid. The associated compliance equations for a CT specimen are given by ASTM E399 (36) as:

$$U = \frac{1}{1 + \sqrt{\frac{E' V_m B_e}{P}}} \qquad [12]$$

$$\frac{a}{W} = 1 - 4.5U + 13.157U^{2} - 172.551U^{3} + 879.944U^{4} - 1514.671U^{5} \qquad [13]$$

where *E'* is E for plane stress and E/(1-ν^2) for plane strain, V_m is the crack mouth opening displacement, B_e is the effective thickness of the sample, *P* is load, *a* is the crack length, and *W* is the ligament length.

Goals of Experiments

The goal of this work is to compare the susceptibility of PH 13-8Mo, an ultra-high strength steel currently used in Naval aviation systems, in three different conditions– solution annealed (SA), H1000 condition (538^{o}C aged) and H1150 (621^{o}C aged). The first objective is to compare the relative susceptibilities of the different tempers in light of their different microstructures by analyzing the time to crack initiation as well as crack growth rates for each temper. Second, the established understanding of hydrogen trapping will be used to explain the crack initiation and growth rate behavior of each temper. Understanding the different hydrogen embrittlement mechanisms is important but not necessarily needed in order to quantify the alloys' susceptibilities to hydrogen embrittlement. This work is part of a larger initiative to examine multiple UHSS alloys (4340, 300M, Hy Tuf, Aermet 100, Custom 465, and PH 13-8Mo) to identify which alloys are most/least sensitive to hydrogen embrittlement in the presence of a residual stress. This data can then be used to refine processing parameters at Navy Fleet Readiness Centers (FRCs) across the country

Stress-intensity life curves were generated by holding a pre-cracked, compact-tension (CT) specimen in tension at a constant displacement. The loaded samples were then exposed to a hydrochloric acid (HCl) solution representative of the stripping baths in the FRCs which is expected to introduce hydrogen into the structure of the samples. Load, crack mouth opening displacement (CMOD), and time were recorded during mechanical testing. These measured values were then used to calculate the stress intensity and crack length as a function of time. Optical microscopy and electron

backscatter diffraction (EBSD) were used to characterize the microstructure while SEM fractography was used to analyze the fracture and crack growth behavior.

Materials and Equipment

PH 13-8Mo

As previously described, PH 13-8Mo is a precipitation hardening martensitic stainless steel. In naval aviation systems it is used in the 538^{o}C (H1000) condition to provide a combination of excellent strength and toughness. The composition and basic material properties of PH 13-8Mo, as specified by Aerospace Materials Specification (AMS) 5629E, have been listed above. The solution annealed (SA) condition material properties are also shown, but are not defined by AMS 5629E. The data has been gathered from other sources as well as from tensile tests performed on specimens for this experiment. Minimum values for toughness are not specified in AMS 5629E and are derived from other handbooks such as the Damage Tolerant Design (DTD) handbook.

Solution annealed PH 13-8Mo (AMS 5629E) was purchased from Metalmen (Long Island, NY) and heat treated by Burton Industries (Long Island, NY) to the H1000 condition (AMS 5629E). Two bars from the entire lot were then solution annealed again in house, being held at 927^{o}C (1700^{o}F) for two hours in air and air cooled. After reaching room temperature, the bars were then cooled in ice-water (~5^{o}C) for approximately 30 minutes to complete the martensitic phase transformation. A single bar was then aged in air at 621^{o}C(1150^{o}F) for 4.25 hours in accordance with AMS 5629E (4 ±0.25 hours) and air cooled to maximize austenite content while staying with the AMS specification.

Compact tension (CT) samples were machined by electro-discharge machining (EDM) out of the heat treated bar stock. The compact tension specimen has the dimensions shown below and is designed to meet plain-strain conditions based on the minimum yield strength and toughness data listed in AMS 5629E and the Metallic Materials Product Design Specification Handbook (MMPDS).

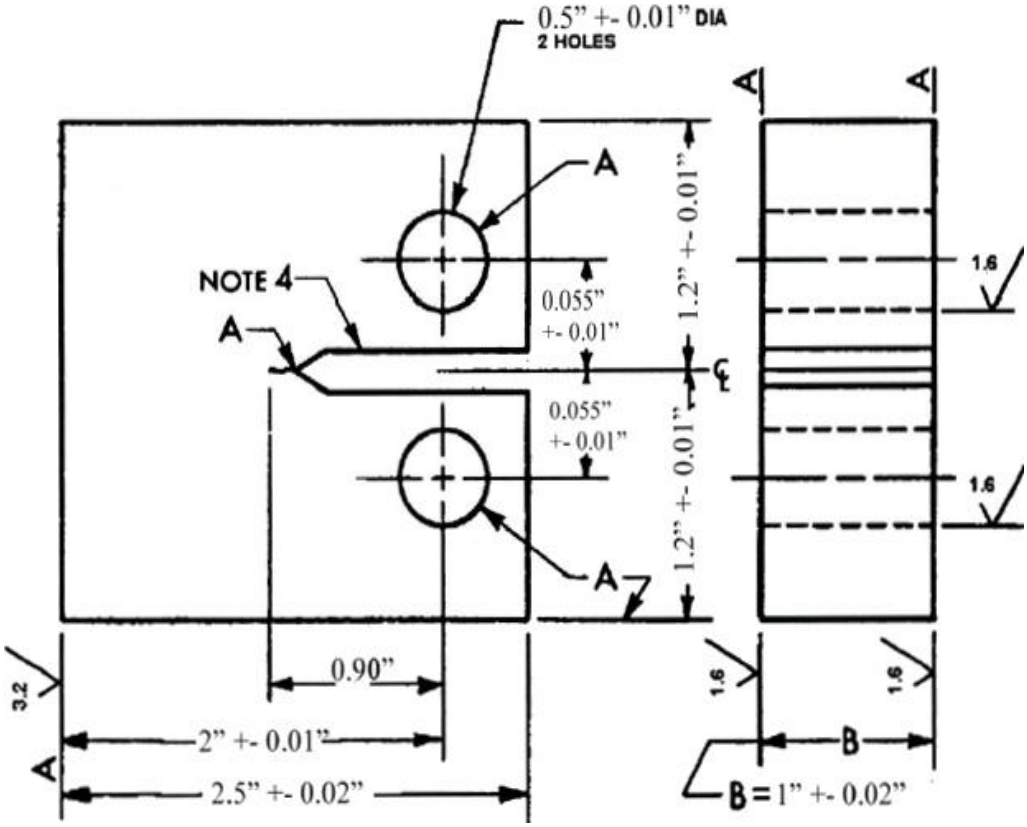

Figure 18: Compact Tension (CT) Specimen Dimensions. (36)

The CTs were then fatigued pre-cracked a length of approximately (0.1") in accordance with ASTM 1680. After fatigue pre-cracking, the samples were side-grooved via EDM with a 20% thickness reduction (0.1" per side with a 60^{o} angle) in order to

promote linear and uniform crack growth during testing, as well as aiding in elastic constraint of the plastic zone around the crack tip.

Fatigue Pre-Cracking System

A number of vertical tensile loading frames were used to fatigue pre-crack the CT specimens. Each test frame was an MTS closed-loop servohydraulic loading frame with feedback control. Fracture Technology Associates' Fatigue Testing and Analysis software was used to fatigue each specimen to a nominal final crack length of 25.4mm (1") while recording crack length, number of cycles, and the crack growth per cycle, da/dN.

Hydrogen Embrittlement Test System

The hydrogen embrittlement test system consists of precision-machined loading frames made from single blocks of 17-4PH steel heat treated to the H900 (482^{o}C aged) condition and a monoblock milled PVC trough. Each frame is designed to be compact, measuring approximately 203mm x 102mm x 38mm (8"x 4"x 1.5"), but able to apply extremely high loads (approximately 80kN/18kip). A floating clevis threaded onto a load-sensing stud (ST-FB 3-4-10NCx 5-1-2; Strainsert Company West Conshohocken, PA USA) pulls tension on the CT specimen by means of a tensioner nut (MT-075-10/w; Superbolt® Inc. Carnegie, PA USA). A clip-on gage (MTS Systems Corporation, Eden Prairie, MN) was used to measure the crack mouth opening displacement (CMOD). Load frame schematics and actual physical dimensions can be seen in Figures 19-22 (with apologies to the reader that they were originally designed in standard units of in/lbf/s).

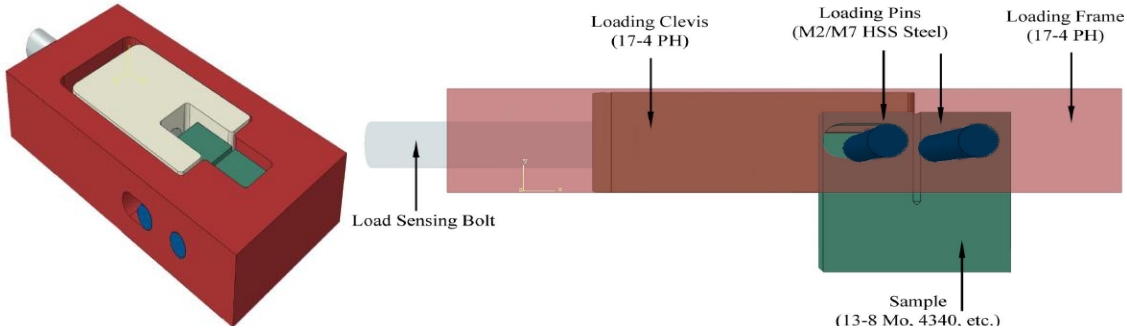

Figure 19: Schematic of the Assembled Loading Frame (left) and Transparent Image (right).

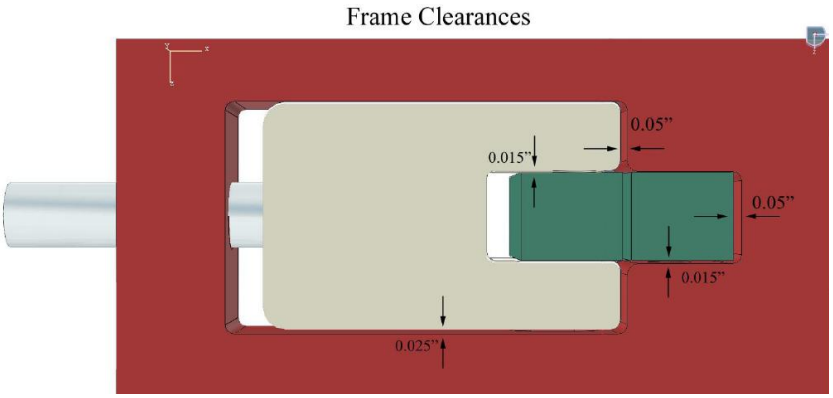

Figure 20: Clearances Between the Load Frame, Clevis, and CT Specimen.

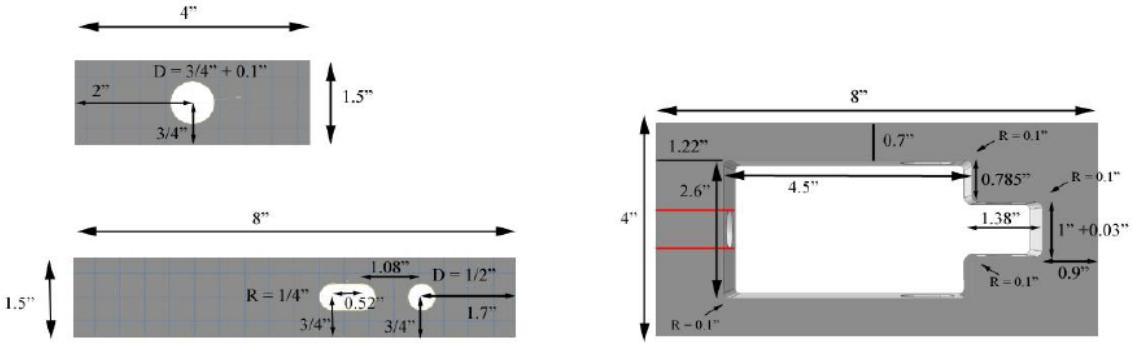

Figure 21: Dimensions for the loading frame.

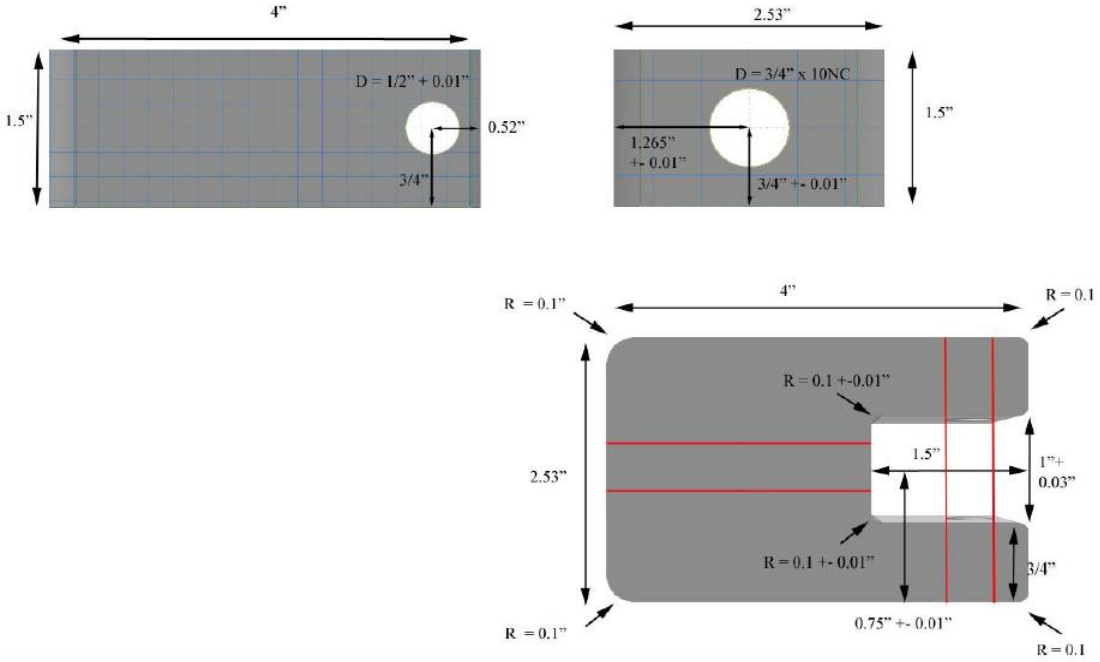

Figure 22: Dimensions for the Loading Clevis.

The test rig is then seated on a custom-milled PVC trough which carries the acid solution to the crack tip of the C(T) specimen. The acid bed is approximately 864 x 89 x 89 mm (34" x 3.5" x 3.5") with a drainage reservoir 508 x 51 x 76mm (20" x 2" x 3").

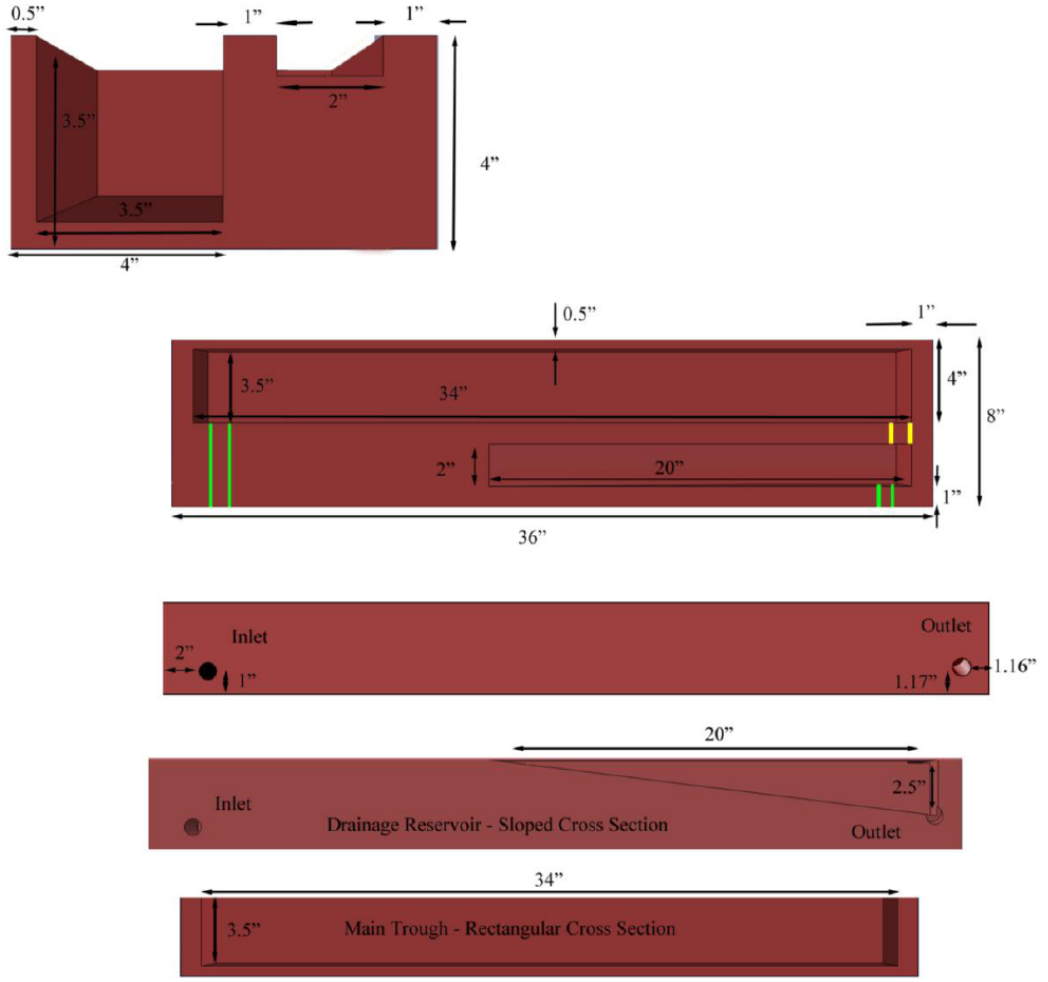

Figure 23: Fluid Trough Dimensions and Cross Sections.

Acid flow is provided by a Cole Parmer (Vernon Hills, IL) Masterflex® L/S® pumpand L/S® Easy-Load II pump head, providing a maximum acid flow rate of 2.3L/min.

The loading clevis and frame were coated with wax in order to prevent them from corroding in the acid and mitigate the chances of creating a galvanic cell between the test specimen and the load frame and clevis. In addition, plastic sheets were placed under the loading frames in order provide another physical barrier between the frames and the acid. Each plastic sheet has a small section cut out so that the CT specimen may fit through.

The hydrogen source, 12M (N) HCl, was purchased from Fisher Scientific and diluted to 10% strength by volume (9:1 water:acid). The entire test system can be seen in operation below:

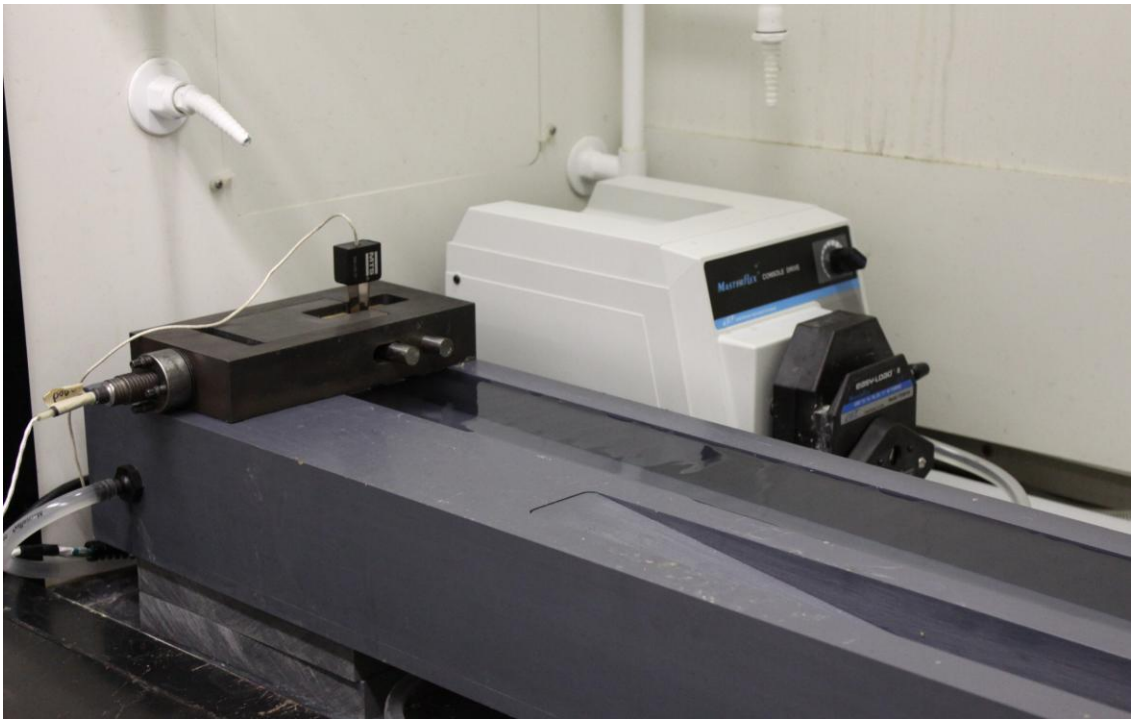

Figure 24: Hydrogen Embrittlement Test System Operating

While a variety of test systems exist for wet environments, this system is more compact and highly scalable. With sufficient clearance, 7 loading frames can be seated onto a single PVC trough in the current system.

LabVIEW Data Acquisition System

LabVIEW™ software from National Instruments (Austin, TX USA) was used to record the signal outputs by the load-sensing stud and clip-on gage. Each load-sensing stud and clip-on gage pair were connected to an NI SCC-SG24 10V excitation full-bridge

signal conditioner. Each signal conditioner was connected to an NI SC-2345 connector block which fed data to the NI 6259 PCI data acquisition card. The interactive front end of the code and a flow diagram can be seen below:

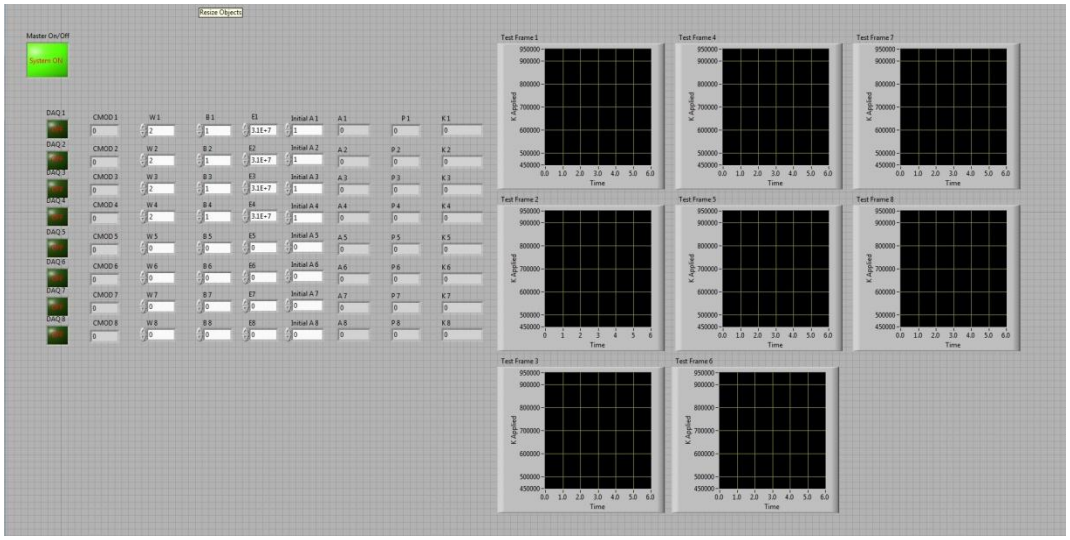

Figure 25: The Interactive Front End of the LabVIEW™ Data Acquisition Program

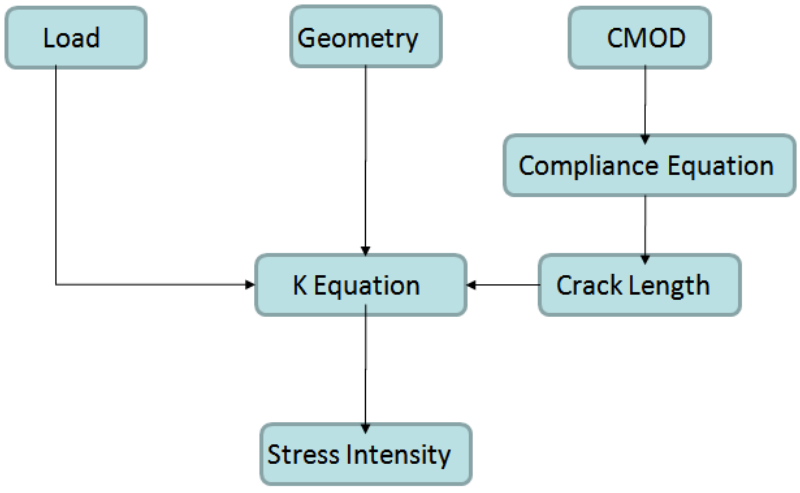

Figure 26: Flow Diagram of Data in the LabVIEW™ DAQ Program.

The LabVIEW™ codeconverts the voltage signals from the load sensing stud and clip gage into load(lbf) and displacement(inches) (note: Labview™ code is graphical, and too large to fit in Appendix. Code files can be furnished upon request). The load and displacement are then input into the compliance equation to compute crack length and the K equation to compute stress intensity. If data collection is not started, then the program simply indicates the current value of stress intensity (ksi-in ½) and crack length (in.) and does not store the data. Data storage is started by clicking on "DAQ 1,2,3,4…" and saving the data to an appropriately named file. The data storage rate was set to 2 Hz since the hydrogen embrittlement testing was going to be run over the course of many hours to days (rates on the order of 100-1000Hz would create extremely, and possibly unnecessarily large data files).

Load sensing studs were calibrated with a 2^{nd} order calibration. Each load sensor was threaded onto a rod that was gripped by an MTS servohydraulic load frame. Using the calibrated load cell on the MTS frame as the reference value, voltage measurements were recorded as the applied tensile load was gradually increased. Voltage measurements were averaged for 5 seconds with a sampling rate of 5 kHz. The average voltage readings from the load stud were input into LabVIEW™ as a calibration curve, and the measured load compared to the applied reference load. The load sensing stud was then cycled up and down three times to establish a calibration profile.

Clip gages were calibrated in a similar manner as the load sensing studs. Each gage was seated on a calibration stand, whose initial knife edge separation was verified with an optical comparator to be 5.08mm (0.2"). A known displacement was applied with calibration stand the voltage readings from the clip gage were averaged over 5

seconds with a sampling rate of 5 kHz. These readings were then input to LabVIEW™ to create a calibration curve, which was then verified by cycling each clip gage up and down three times.

SEM

SEM fractography was carried out at NAVAIR Patuxent River on a JEOL 6460LV SEM with a thermionic emission electron source. The accelerating voltage was 20kV with a spot size of 42. The primary observation mode was secondary electron mode.

EBSD

Electron-backscatter diffraction (EBSD) was performed at the Centralized Research Facilities (CRF) of Drexel University on an FEI XL30 environmental scanning electron microscope (ESEM) with attached EBSD camera from TSL. TSL's OIM Analysis 5 was used to analyze the resulting diffraction pattern data set. The data cleanup procedure was as follows:

1) Set minimum confidence index to 0.08
2) Grain confidence standardization with an angle tolerance angle of 3 degrees
3) Neighbor Orientation Correlation (level I, grain tolerance angle of 3 degrees)
4) Grain Dilation (1 iteration)

Experimental Methods

Fatigue Pre-Cracking

Fatigue pre-cracking was carried out both in load and K-control. Before the fatigue crack was initiated, a load of ~13.3kN (3000lbf) was applied through a 8Hz sinusoidal signal with an R-value of 0.1 in load control. Once the fatigue crack was initiated, the tensile frames were switched to operate in K-control with a maximum applied K value of ~20 MPa-$m^{½}$ (18 ksi-$in^{½}$). The fatigue crack length was monitored by the FTA software as well as rail-mounted microscopes from Mitutuyo. The nominal final fatigue crack length was 2.54mm (0.1"), giving a total crack length of 25.4mm (1") in the CT specimen and a ratio of crack length (a) to ligament length (W) of a/W = 0.5. The accompanying non-dimensional stress intensity factor,Y (not to be confused with K, which has units of MPa- $m^{½}$ or ksi-$in^{½}$) for a/W = 0.5 is 9.66 when substituted into equation [11].

Hydrogen Embrittlement Testing

First, the data storage was started for the load frames in which samples were being loaded. This allowed capture of both the loading and hydrogen embrittlement cycles. The CT specimen was then loaded into the frame and the clip gage placed in the knife edges of the specimen. The tensioner nut on the load-sensing stud was torqued to produce a given load, which is then turned into stress intensity by equations [10-13]. The PVC trough containing the acid is filled to the appropriate level (if not already done so). After loading to a given K level is complete, the clip-gage is removed from the knife-edges. The specimen is then seated so that the notch of the crack is submerged in acid

and the clip gage is re-attached. The discontinuity in the clip gage versus time data allows for easy determination of end of the loading cycle and the beginning of the hydrogen embrittlement cycle. As the crack grows and the load drops, the LabVIEW™ program automatically calculates the compliance and changes in crack length from the change in load and CMOD and uses this new data to update the value of K. Load, CMOD, a, and K, as well as the duration of the test, are recorded simultaneously by the data acquisition system.

CT specimen dimensions, including true initial (a_o) and final (a_f) crack lengths, were measured on an S-T Industries Inc. 4600 series optical comparator with a Quadracheck 2000 digital readout.

Metallography

Metallographic samples were first machined from heat treated bar stock using a Buehler 1030 cutoff wheel. The samples were then cold mounted in epoxy. Next, they were prepared on a Buehler automated grinder/polisher (model #) using 240, 600, and 1200 grit papers for 5 minutes at each stage. The samples were hand-polished by an expert metallographer at Patuxent River Naval Base using 9um and 1um diamond polishing cloths and etched using a cotton swab with Viella's Reagant (1g Picric Acid, 5mL HCl, 100mL ethanol) for 10-30 seconds (the length of the etch depending on whether the sample was SA, H1000, or H1150). Etched samples were viewed under a Nikon Epiphot 300 optical microscope with an attached digital camera. Buelher Ominmet software (v4.00B015) was used to capture digital images from the optical microscope.

Tensile Testing

Sub-sized dogbone-style tensile bars were cut from the PH 13-8Mo bar stock. The tensile specimen dimensions met the minimum length requirements of ASTM E8 for tensile testing (37). The dimensions of the dogbone samples (in inches) are shown below:

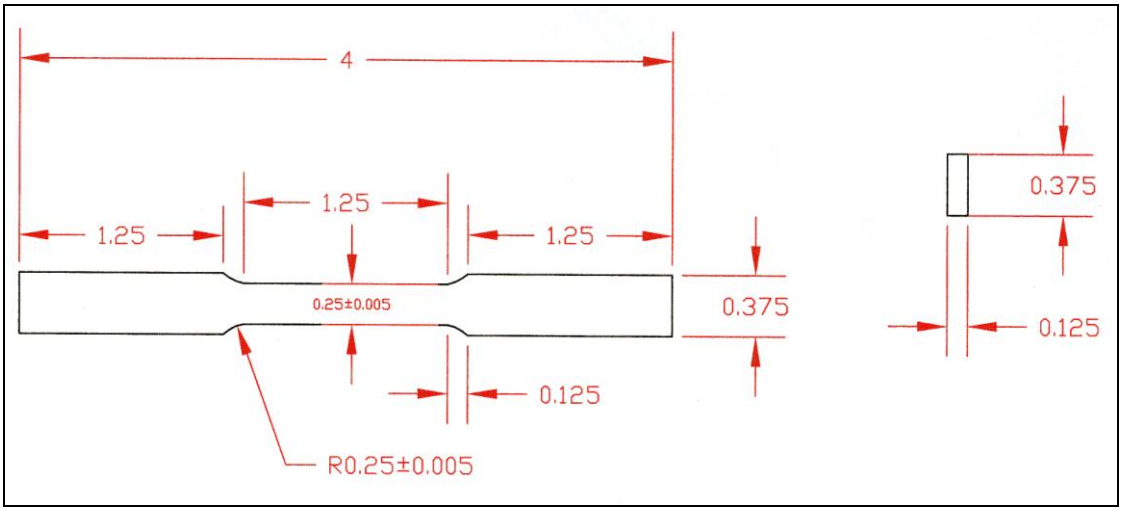

Figure 27: Small Dogbone Tensile Bar Used for Tensile Testing. Dimensions are in Inches.

The rolling direction in the tensile specimen was aligned with the tensile axis, meaning the measured tensile properties are expected to be slightly higher than other specimen orientations (normal or transverse).

The samples were loaded into an MTS hydraulic loading frame with an attached load cell and displacement gage and loaded in tension at a displacement rate of ~1mm/min (0.04 in/min) until failure. The resulting load and displacement data were converted into engineering and true stress/strain data based on the following relationships (38):

$$\sigma_e = F/A_o \qquad [14]$$

$$\sigma_t = \sigma_e(1+ \varepsilon_e) \quad [15]$$

$$\varepsilon_e = \Delta L/L_o \quad [16]$$

$$\varepsilon_t = \ln(1+ \varepsilon_e) \quad [17]$$

It should be noted that the relationships between true and engineering stress/strain are only valid until the point at which necking occurs (the engineering ultimate tensile strength, UTS). Once necking begins, volume is no longer conserved and the relationships break down.

K_{IC}/K_Q Testing

Fracture toughness testing was performed in MTS closed-loop servohydraulic load frames. The clip gage was seated in the knife edges of the specimen and the clip gage reading zeroed, after which the specimen was loaded into the clevises of the test frame. Load was then imposed upon the specimen until failure occurred. Data was recorded at approximately 100Hz. The resulting load vs. displacement records were analyzed in accordance with ASTM E399.

SEM Fractography

SEM fractography was performed on a Jeol JSM 6460LV at NAVAIR Patuxent River. Fractured samples were cleaned in a solution of Alconox® beforehand to remove rust, dirt, or any loose debris and dried with compressed air. The accelerating voltage was 20kV and the spot size was 42.

Electron Backscatter Diffraction (EBSD)

EBSD was performed at Drexel University's Centralized Research Facilties (CRF) on an FEI XL30 Environmental SEM (ESEM). The EBSD system is from TSL, and the EBSD data analysis was performed using TSL's OIM 5 software. The accelerating voltage was 20kV, the spot size was 5, and a 50um aperture was used.

Chapter 3: Results and Discussion

Optical Microscopy and EBSD

Maraging steels, PH 13-8Mo included, are typically supplied in the solution annealed (SA) condition and then heat treated to achieve the desired properties for strength and toughness. Optical micrographs of the SA condition can be seen below in Figures 19-20.

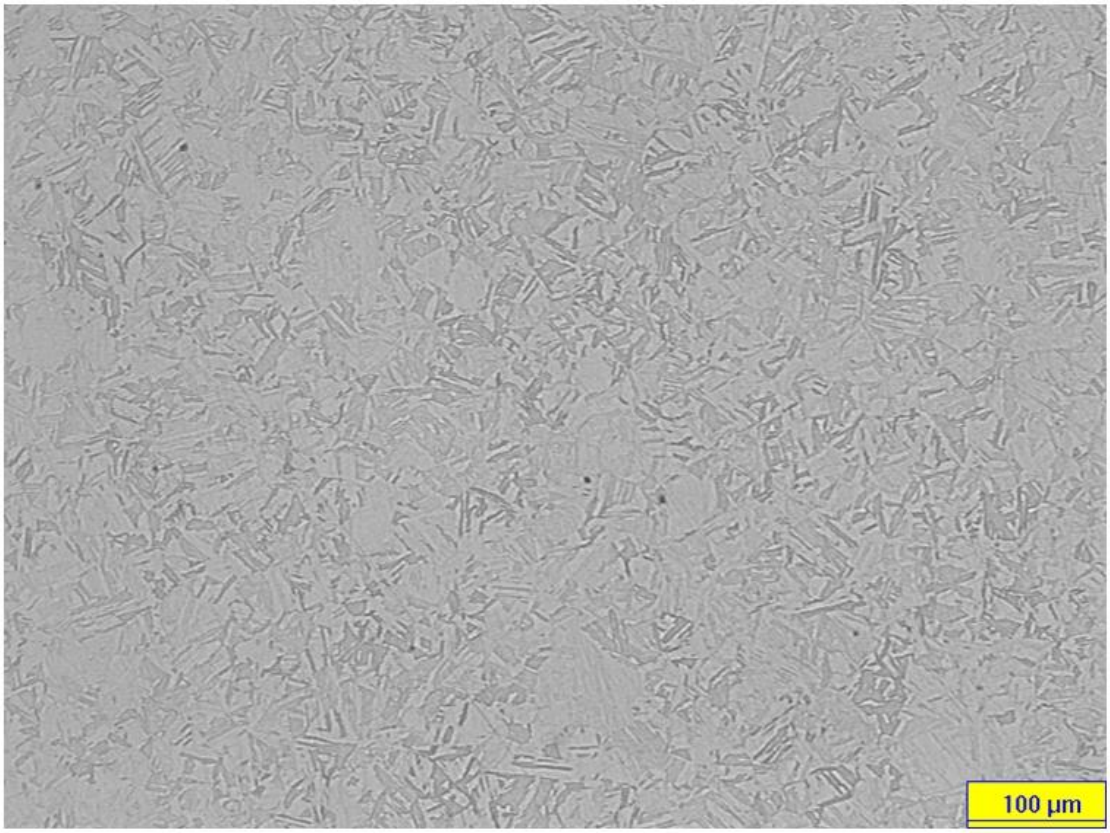

Figure 28: PH 13-8Mo in the Solution Annealed (SA) Condition at 100x.

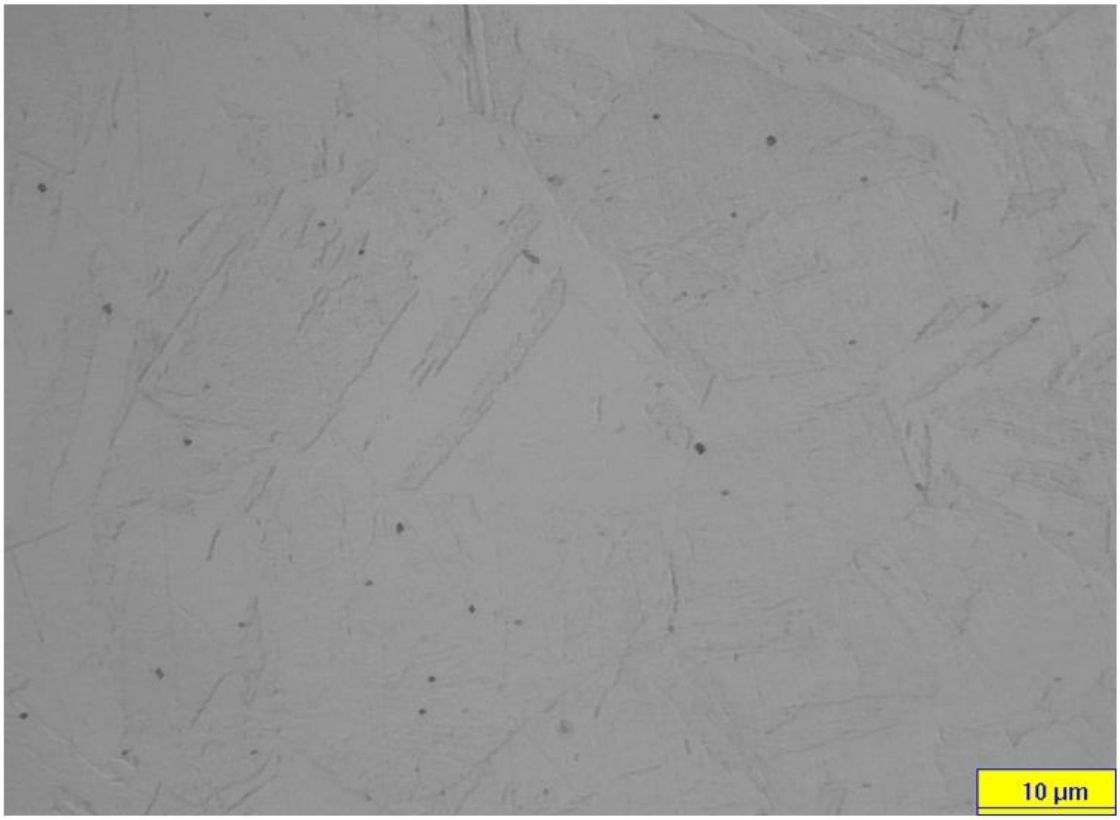

Figure 29: PH 13-8Mo in the Solution Annealed (SA) Condition at 1000x.

The solution annealed condition consists entirely of a highly dislocated lath martensite. Due to the light etching, the expected fine lath structure (based on the work of Seetharaman) is too fine to resolve under optical microscopy. When an austenite grain shears under martensite transformation, there are a total of 24 potential orientations of martensite (variants) that can form from a single austenite grain. The slender regions appearing to be laths are actually a packet of laths of a single martensite variant. In addition, faint boundary lines, on the order of 30 microns, can be observed in Figure 29. It is inferred that this is roughly the size of the prior austenite grain which nucleated the various martensite laths. Small dots also pepper the image in a heterogeneous fashion. Under SEM, these appeared to be small pits – possibly impressions left from debris in the

polishing process. No retained austenite is expected, based on the Delong diagram, as well as Seetharaman's prior work. Work from Seetharaman gives expected yield and tensile strengths of 640 and 1040 MPa, respectively. This strength can be attributed to some degree of solution hardening, since the martensite is supersaturated with the alloying elements, as well as dislocation strengthening based the shear flow strength relationship (27):

$$\tau_{crss} \alpha\ Gb\rho^{\frac{1}{2}} \qquad [19]$$

τ_{crss} is the critical resolved shear stress required for slip, G is the shear modulus, b is the Burger's vector (length of a single dislocation motion, approximately the size of 1 atom), and ρ is the dislocation density. Typical dislocation densities for lath martensites are on the order of 10^{15} to 10^{16} m/m^3 (27).

Since all of the alloying elements are in solution, there is also some degree of solid solution strengthening, which can be described by several equations (the Mott and Nabarro equation is given) (39):

$$\Delta\tau = \mu\eta^2 c \qquad [20]$$

where μ is the shear modulus, η is a variable describing the size difference of the atoms, and c is the concentration of the solute. Upon ageing the SA material at 538^{o}C (1000^{o}F) for approximately 4 hours, it has been reported that NiAl particles precipitate within the martensite laths, providing a significant degree of hardening via intermetallic precipitation (4). Strengthening via precipitation can occur by either dislocation cutting or bowing. In both cases however, the two most important parameters are the size and spacing of the precipitates. Orowan/Ashby strengthening suggests that very fine and

uniformly dispersed precipitates provide the greatest level of strengthening, as described by (39):

$$\Delta\tau = \frac{A(\varphi)\mu b}{2\pi L}\ln\left(\frac{1}{2b}\right) \quad [21]$$

A(φ) is a constant that describes the nature of the dislocation (screw, edge, or mixed), μ is the shear modulus, b is the Burger's vector, and L is the precipitate spacing. Ageing at higher temperatures for longer times will increase both particle size and spacing (since some precipitates are consumed at the expense of others' growth), and so the strength decreases in the overaged conditions.

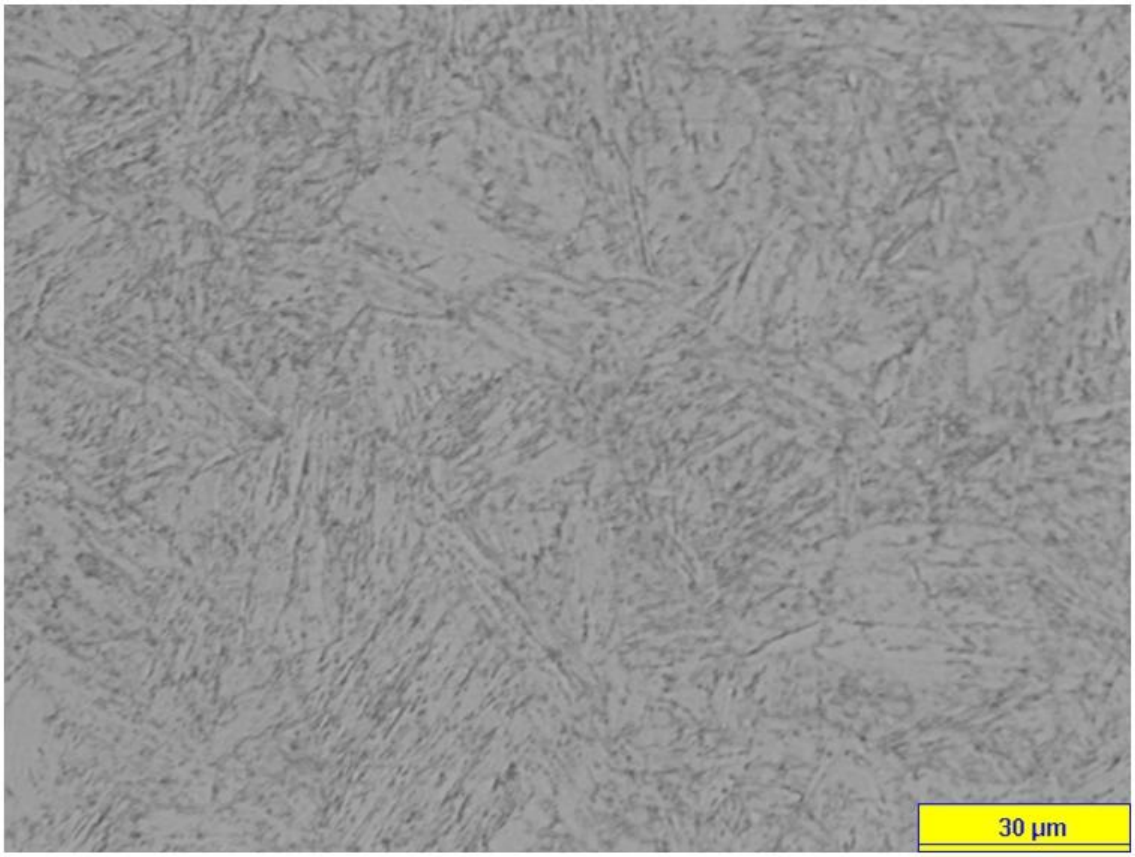

Figure 30: PH 13-8Mo in the H1000 Condition at 500x.

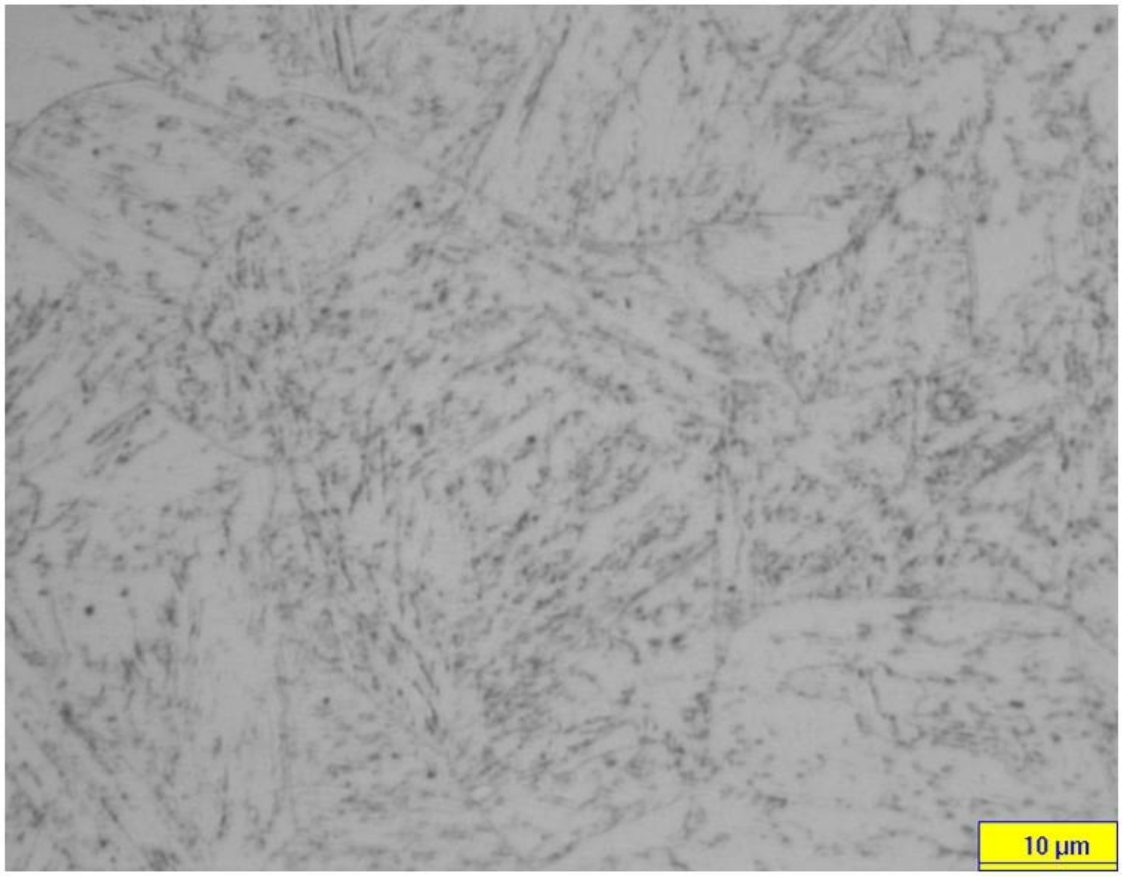

Figure 31: PH 13-8Mo in the H1000 Condition at 1000x.

The microstructures depicted in Figures 30 and 31 are typical of PH 13-8Mo in the H1000 condition (538^{o}C/1000^{o}F aged for 4 hours). A large number of NiAl precipitates have formed along the martensite lath boundaries (presumably within the laths as well), enabling them to be seen much more easily when compared with the SA condition. In addition, prior austenite grain boundaries are much more obvious. Prior austenite grain size appears, again, to be on the order of 30 microns. Unlike the SA condition, the small black dots are most likely to be reverted austenite. Seetharaman reported roughly 2% reverted austenite after heat treating PH 13-8Mo for 2 hours at 535^{o}C (4). Schnitzera et al. studied the growth of reverted austenite in PH 13-8Mo and

found a maximum of approximately 7.5% austenite after 4 hours of ageing at 575^{o}C (7). Using GIMP (GNU Image Manipulation Program), an open-source image editor, the image contrast was maximized to create a black-and-white picture. The histogram feature was then used to estimate the total area of black color, on the assumption that the remaining black spots were austenite.

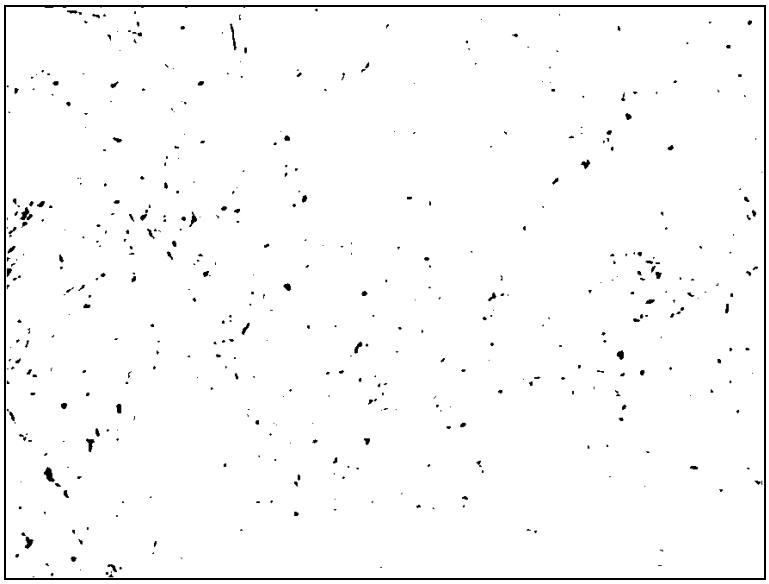

Figure 32: Contrast Adjustments to Figure 28 Highlight Potential Areas of Reverted Austenite.

Presumably not all of the black color in the image is truly austenite, thus the resulting number is *an overestimation of the reverted austenite content in the H1000 condition*. Most likely, much of the black area in Figure 32 is a result of contamination (dust particles, embedded diamond particles from polishing, etc.). The resulting black area, "reverted austenite content," based on Figure 32 is one percent (1%) reverted austenite, which is on the order of the observations performed by Seetharaman. Variables such as precise alloy content, particularly C, Cr, and Ni, as well as how the

alloy was cast may greatly affect the resulting structure. The alloy received in this study, in accordance with AMS 5629E, is vacuum induction melted (VIM) and consumable electrode vacuum melted (CEVM), while Seetharaman's work was done with a hot-forged round bar of PH 13-8Mo.

Ageing at higher temperature (621^{o}C/1150^{o}F) and slightly longer time (4.25 hours) dramatically increases the number of precipitates formed as well as the volume fraction of austenite.

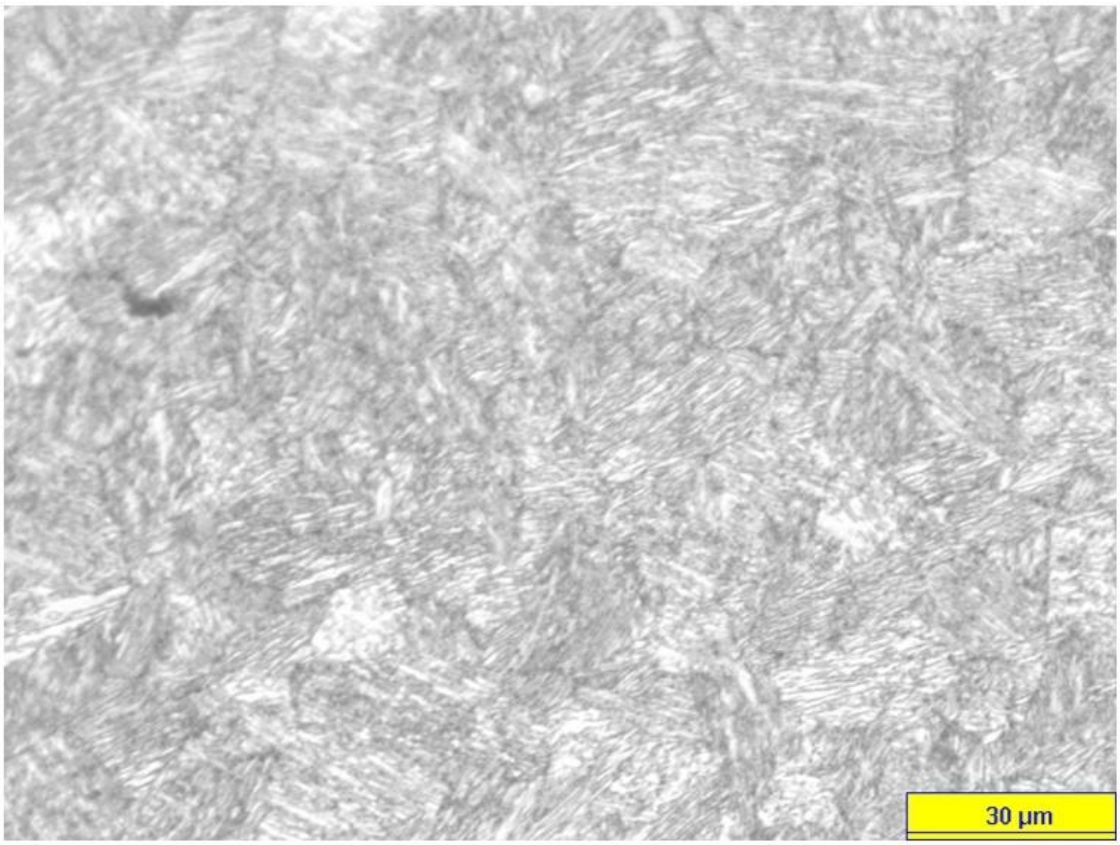

Figure 33: PH 13-8Mo in the H1150 Condition at 500x.
The large number of precipitates are able to highlight individual lath boundaries.

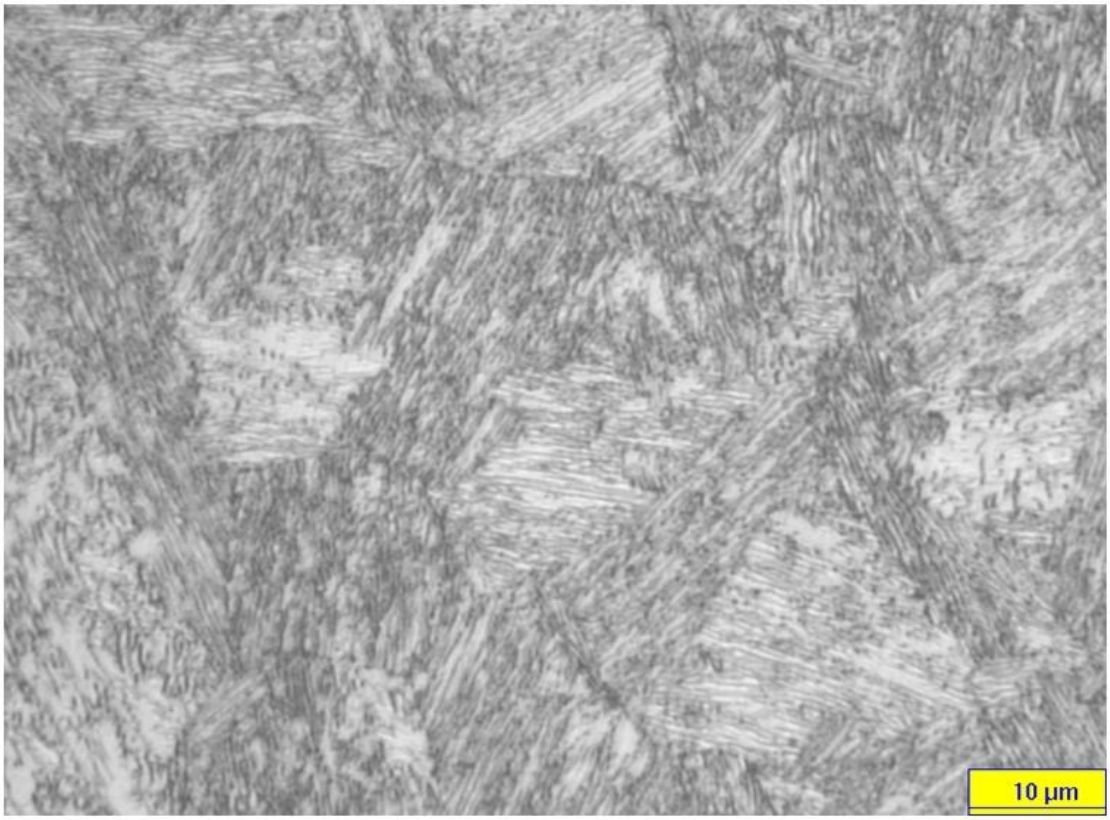

Figure 34: PH 13-8Mo in the H1150 Condition at 1000x.
Individual lath variants and their growth directions can be seen.

In the H1150 condition, heat treatment at higher temperatures for longer periods of time is expected to cause the precipitates to coarsen (though still only resolvable by TEM) (4). Seetharaman also reported that the some Ni_3Mo or Ni_4Mo begins to precipitate instead of NiAl. The volume fraction of austenite has increased substantially, however it is difficult to determine from the images the precise amount. An image analysis identical to that performed in Figure 32 results in 3.1% black area ("reverted austenite content"). Because of the significant precipitation along lath boundaries, much of the dark color in Figures 33 and 34 may not actually be real austenite. EBSD results, discussed later, also gave insight on the fraction of austenite present in the H1150 condition. As before, this number most likely represents an overestimation of the total

austenite content. As a result of precipitation coarsening and a larger fraction of austenite, the H1150 condition is significantly softer than the H1000 condition, possessing drastically lower yield and tensile strength, although its corrosion-resistance is greatly increased. Numerous reports have suggested that austenite is highly resistant to hydrogen embrittlement (21; 31), and thus for a specimen equivalent fraction of K_{IC}, one would expect crack initiation to take significantly longer in the H1150 condition than either the H1000 or SA conditions. The effects of precipitation and austenite formation will be explored later with mechanical testing results.

In addition to traditional metallography, EBSD was also used to analyze the microstructure of PH13-8Mo in the SA, H1000, and H1150 conditions. For the SA condition, an extremely fine scan was performed (spacing 0.07 um) to try and determine the approximate lath size. A larger step size of 0.2 um was used for the H1000 and H1150 conditions.

As previously stated, PH 13-8Mo is 100% lath martensite in the SA condition. EBSD imaging was able to reveal packets of laths of identical variants (as denoted by having a uniform color in the inverse pole figure image below).

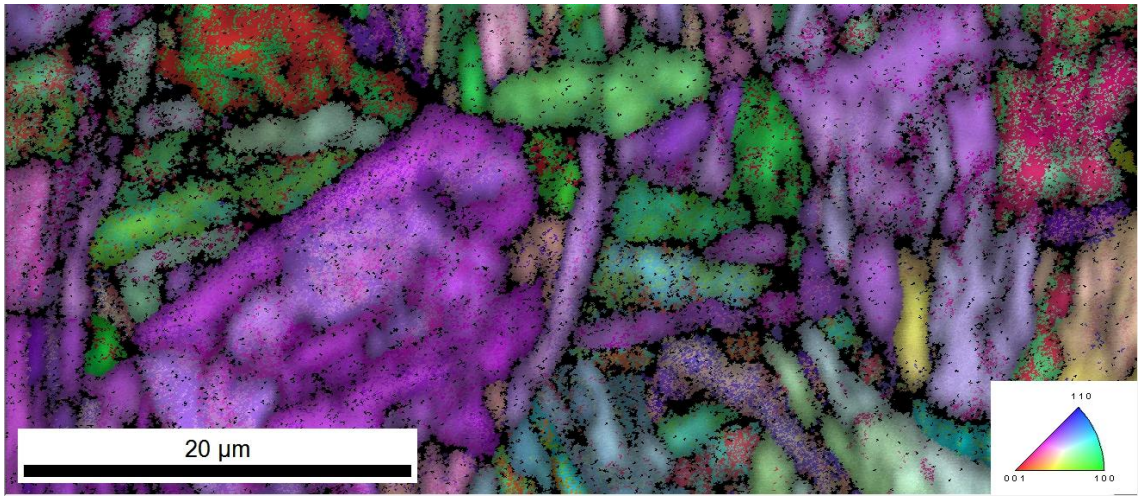

Figure 35: Colored Inverse Pole Figure (IPF) of PH 13-8Mo in the SA Condition.
Note: Red corresponds to 001, green to 100, and blue to 110

Based on the scaling, the typical packet size appears to be 1-2um wide, with some variants being larger than others (this may also be a result of the quality of data). The OIM analysis software calculated the mean "grain" diameter to be 0.15um, roughly the expected thickness of a single martensite lath. The actual distribution of the IPF points for the SA condition can be seen below:

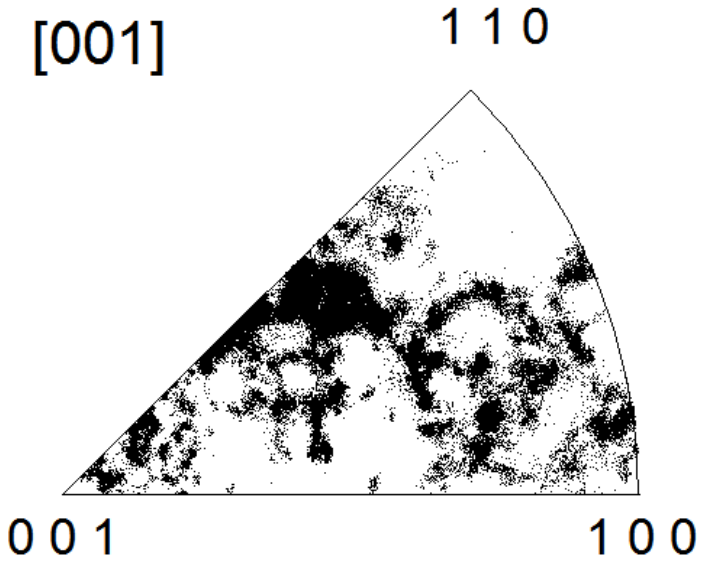

Figure 36: IPF Distribution of Figure 35

Most of the data points are clustered around the [001] orientation followed by the [110], with [100] being the orientation of least frequency. Due to the small area analyzed, approximately 58x28 um^2, the IPF in Figure 36 appears to be relatively discretized. A larger area sampling would help smooth out the distribution and be more representative of the overall microstructure.

In the H1000 condition, the [001] remains the favored direction even after precipitation heat treatment (if aged for long enough times, the growth of reverted austenite may have an effect on the texture of the material). The average grain diameter increased to 0.45 microns, though this may partly be a result of the increased step size, as opposed to entirely a result of grain coarsening from the heat treatment. The benefit of the increased step size for the H1000 scan was that a larger area (140x117 um^2) could be sampled for an equivalent time period. The IPF distribution is significantly more populated. In addition, the larger area scan begins to reveal the prior austenite grain structure with respect to the different martensite variants.

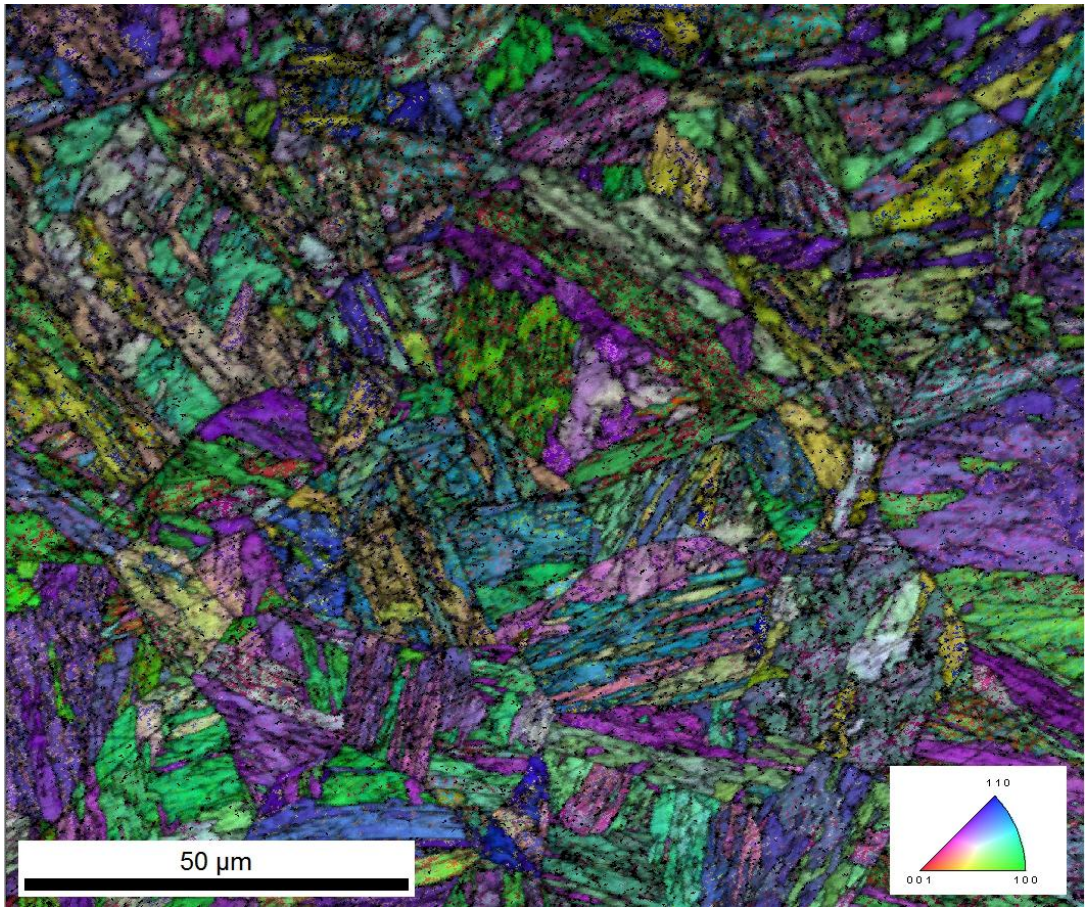

Figure 37: Colored IPF of PH 13-8Mo in the H1000 Condition.
Note: Red corresponds to 001, green to 100, and blue to 110

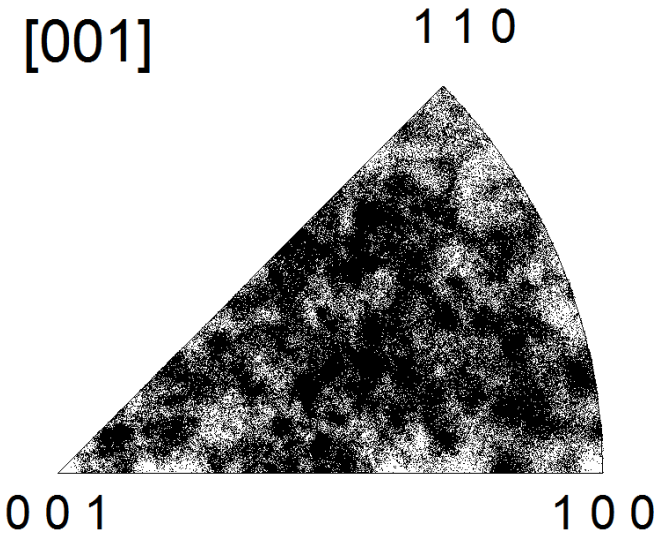

Figure 38: IPF Distribution of Figure 37

Though optical microscopy detected some austenite, none was detected in EBSD for the H1000 condition sample. This could be the result of the relatively large step size as well as sample contamination from polishing and handling.

In the H1150 condition, the large area scan size (288x171 um^2) yields a large enough area that virtually the entire IPF distribution is saturated, meaning no conclusions can be drawn from the IPF. Austenite becomes detectable via EBSD in the H1150 condition as a result of increased nucleation and growth from the higher aging temperature (621^oC for H1150 vs 538^oC for H1000). Austenite was highlighted in the OIM software by using the Phase plot, which assigns a unique color to each phase, and further highlighting the grain boundaries of the austenite to make the relatively small grains readily discernible at no/low image magnification.

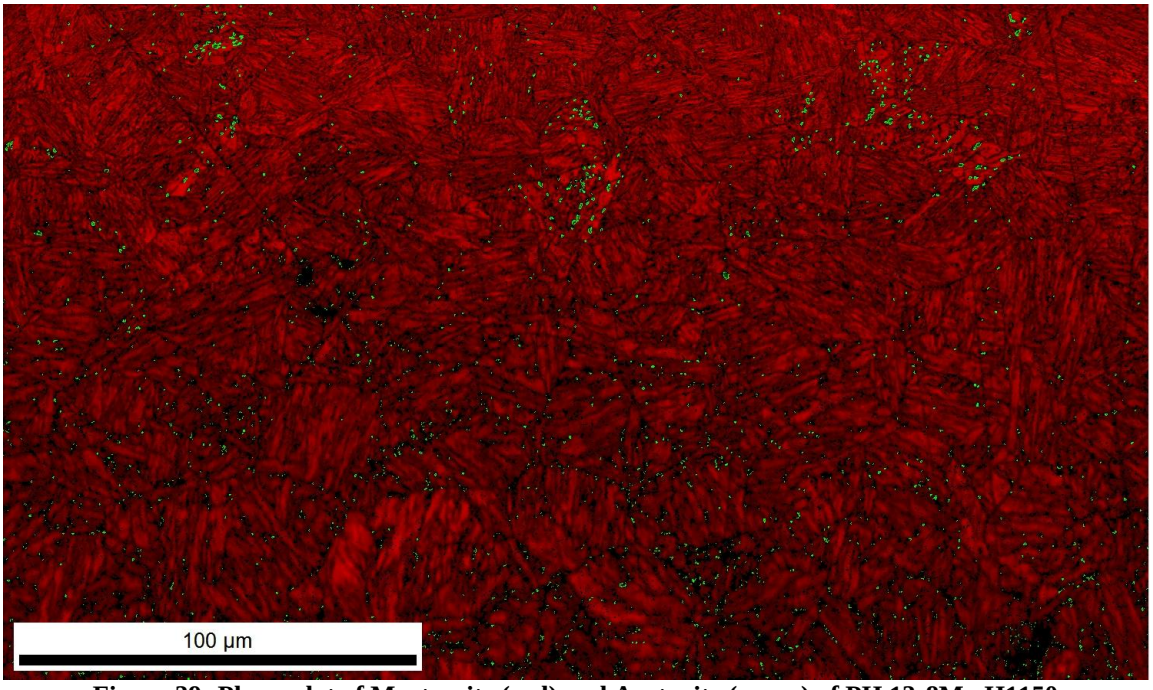

Figure 39: Phase plot of Martensite (red) and Austenite (green) of PH 13-8Mo H1150.
Notice how the austenite populates the boundaries between lath packets (variants) of martensite.

While there are only a handful of points indexed in the austenite IPF, Figure 40, there is a slight preference for a certain direction, namely the [111]. This is could be a result of the Kurdjumov-Sachs (KS) or Nishiyama-Wasserman (NW) orientation relationship, which has been observed in maraging steels by prior researchers (8; 40). To further investigate this observation, an area of austenite particles was selected and magnified. In Figure 41, the austenite particles that are clustered together within a ~30um spacing (roughly the order of a prior austenite grain) virtually all have the same orientation.

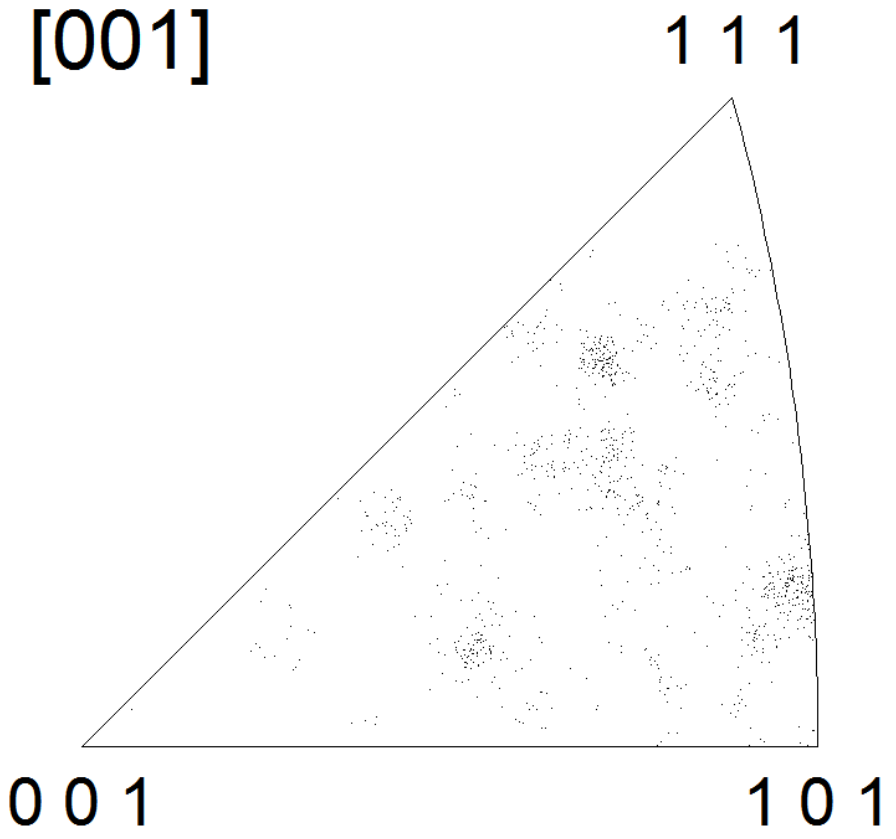

Figure 40: IPF of Austenite in PH13-8Mo H1150

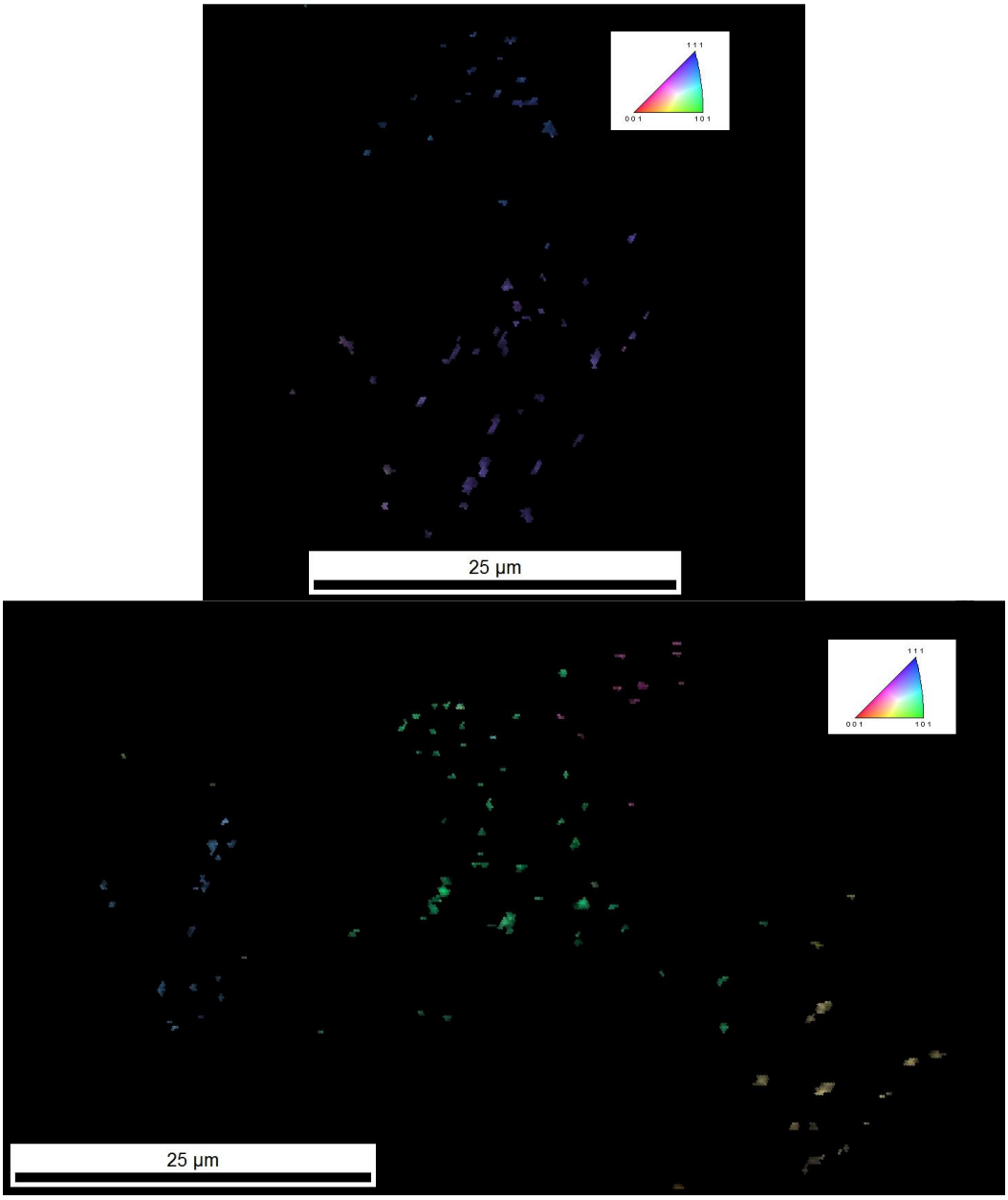

Figure 41: Reverted Austenite Within Clusters Tend to have Similar or Identical Orientations
Note: Red is 001, green is 101, blue is 111

It has been noted by Hsiao, Chiou, and Yang that reverted austenite in PH 17-4, a precipitation hardening steel similar in composition to PH 13-8Mo, possesses the NW orientation relationship with the martensite from which it forms (8), and that the reverted austenite has some form of "memory."

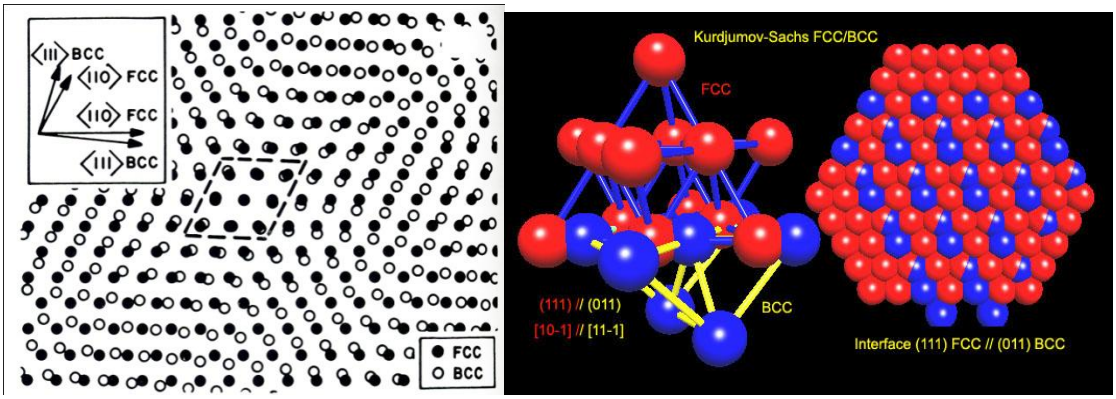

Figure 42: The Nishiyama-Wasserman (NW) and Kurdjumov-Sachs (KS) Orientation Relationships
NW (left) and KS (right) images courtesy of Porter and Easterling (KS) (41)and Hulinks(NW) (42).

Table 8: The Kurdjumov-Sachs and Nishiyama-Wasserman Orientation Relationships

Orientation Relationship	Plane Orientation	Direction Orientation
Kurdjumov-Sachs (KS)	$\{111\}_{fcc}$ // $\{110\}_{bcc}$	$< 101 >_{fcc}$ // $< 001 >_{bcc}$
Nishiyama-Wasserman (NW)	$\{111\}_{fcc}$ // $\{110\}_{bcc}$	$< 101 >_{fcc}$ // $< 111 >_{bcc}$

In both the KS and NW orientation relationships, the (111) planes in austenite (FCC) are parallel to the (110) planes in ferrite/martensite (BCC). In addition, the <101> direction in austenite is parallel to <001> in ferrite/martnesite for the NW relationship while the <101> planes in austenite are parallel to the <111> planes in ferrite/martensite for the KS relationship. Images of both the Nishiyama-Wasserman and Kurdjumov-Sachs relationships are provided above, along with Table 8 detailing the official nomenclatures (43).

If the reasoning for the apparent "memory" of reverted austenite has not already been addressed, it is proposed that it can readily be explained in terms of the minimization of interfacial energy. Based on the orientation data collected in this experiment on PH 13-8Mo, it can be seen that there are packets of laths with a common

orientation – these laths all transformed into the same variant of martensite from the prior austenite grain. Inside of these packets, the martensite lath boundaries are most likely low-angle grain boundaries (LAGBs). However, between laths of differing variants, there should be high-angle grain boundaries (HAGBs). HAGBs have a significantly higher interfacial energy than LAGBs, and would therefore provide significant energy for nucleation of reverted austenite. In order to minimize interfacial energy between two (or more) different lath variants and the nucleated austenite, the orientation of reverted austenite that would nucleate would possess the same orientation as the prior austenite grain, since that particular prior austenite grain must shear and give rise to the current martensite laths. While it has not been confirmed that PH 13-8Mo possesses the KS or NW orientation relationships, there is no particular reason why this would not be applicable to precipitation hardening steels possessing the NW relationship as well, such as 17-4 PH or 18Ni, since the NW and KS orientation relationships are two variants of the $(110)_{bcc}//(111)_{fcc}$, but with different directions being parallel between the crystal systems (8; 40).

Tensile Testing

The tensile properties of PH 13-8Mo are relatively well known, having been studied by various authors, given in material specifications, and statistically established in the Metallic Materials Properties Development and Standardization Handbook (MMPDS-04). The tensile values found in the MMPDS (and materials specification documents, eg AMS 5629E) are more representative than those found in individual studies because of the fact that the important tensile properties (yield and ultimate stress,

reduction in area, etc.) are provided on a statistical basis. For a comparison between typical stress-strain properties (MMPDS) and those as-measured, the reader is directed towards Appendix Graph A9.

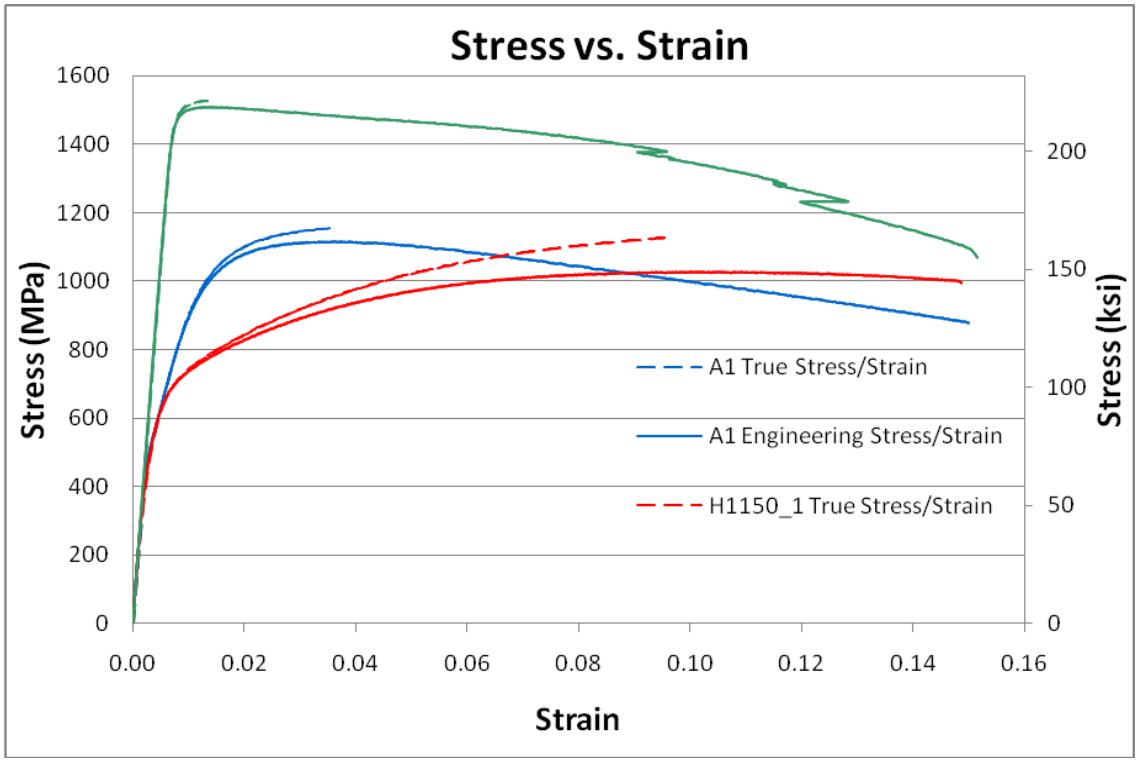

Figure 43: Engineering and True Stress-Strain Curves for PH13-8Mo
Note: The clip gage used (12.7mm gage length) ran out of travel for the H1150 sample, so its strain data is incomplete. For the H1000, the clip gage did not seat well, leading to discontinuities in the strain data.

Tensile stress-strain curves for the H1000, H1150, and SA conditions, tested in the longitudinal direction, are shown above in Figure 43 and compared with their respective properties from MMPDS-04 (except the SA condition) below:

Table 9: Average Tensile Properties of PH 13-8Mo in Various Heat Treatments

Sample	0.2% Offset Yield Strength (MPa)	Ultimate Tensile Strength (MPa)	Average Uniform Strain	Average % Reduction in Area
H1000	1500	1510	0.013	41
SA	650	1120	0.035	60
H1150	630	1030	0.10	63
H1000 (MMPDS)	1310	1390	-	50
H1150 (MMPDS)	620	930	-	50

The yield strength, ultimate tensile strength, and percentage elongation of both the measured samples, and the statistically derived values from the MMPDS, are given in Table 9 above. The as-measured properties for the H1000 and H1150 conditions are higher than those given by the MMPDS – this is because the MMPDS values are based around statistical measurements. For the H1000 condition values, the MMPDS properties are designed around 99% exceedance at a 95% confidence level (99% of all PH13-8Mo H1000 in AMS 5629E specification should exceed the associated yield strength, ultimate strength, and elongation). A 99% exceedance with 95% confidence is referred to as the "A-basis." The "B-Basis" values (not listed) have only a 90% exceedance rate, and thus the associated strengths are higher because less material is required to "pass." As the percentage exceedance rises, the mechanical properties will become more and more conservative to account for increasingly stringent statistical limits. The same is true for the H1150 condition, though the MMPDS rates its values at the "S-Basis." "S-basis" can be considered equivalent to "A-Basis", but more testing needs to be performed for the values to be statistically derived for 99% exceedance at a 95% confidence level.

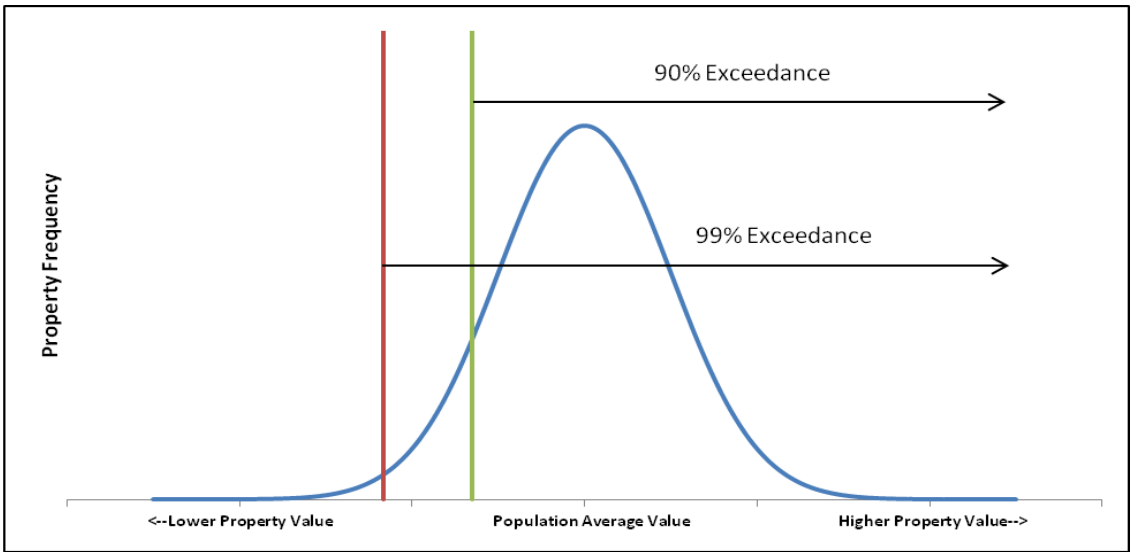

Figure 44: Schematic Normal Distribution for Material Property Values

Assuming that the distribution of the data from MMPDS obeys a normal distribution behavior, a schematic of the normal distribution with 99% and 90% exceedances is shown above in Figure 44.

Typical ("average") *yield and ultimate tensile stress* values for PH 13-8Mo H1000 are around 1415 MPa for the yield stress and 1480 MPa for the ultimate tensile stress. Compared to the as measured yield stress of 1497 MPa and UTS of 1509, the as-measured material is on the higher end of the assumed property distribution.

With respect to the effects of the heat treatments on the mechanical properties of PH 13-8Mo, the SA condition's high dislocation density gives it relatively good strength and ductility (though PH 13-8Mo is never actually used in the SA condition). Aging at 538^{o}C increases strength dramatically at the cost of ductility as fine NiAl particles precipitate. Any dislocation recovery from the aging process is overcome by the precipitation

strengthening. Overaging at 621^{o}C in the H1150 condition yields a combination of martensite and austenite that is extremely soft. Between austenite growth and dislocation recovery, significant strength loss occurs, as the H1150 condition has vastly lower yield and ultimate tensile strengths than the H1000 condition, and moreover, lower strengths than even the SA condition. The H1150 condition tends to be the most corrosion resistant of all the tempers (at least with hydrogen embrittlement, HE resistance is associated with greater austenite content). The low-strength, high-ductility nature of the SA and H1150 conditions will later affect the apparent plane strain fracture toughness testing for these tempers (the failures were predicted, and indeed observed, to be entirely ductile). All of these properties are to be expected, however. A more interesting analysis might be of the effects of the heat treatment on the strain hardening abilities of the different tempers, which are shown below in Figure 45.

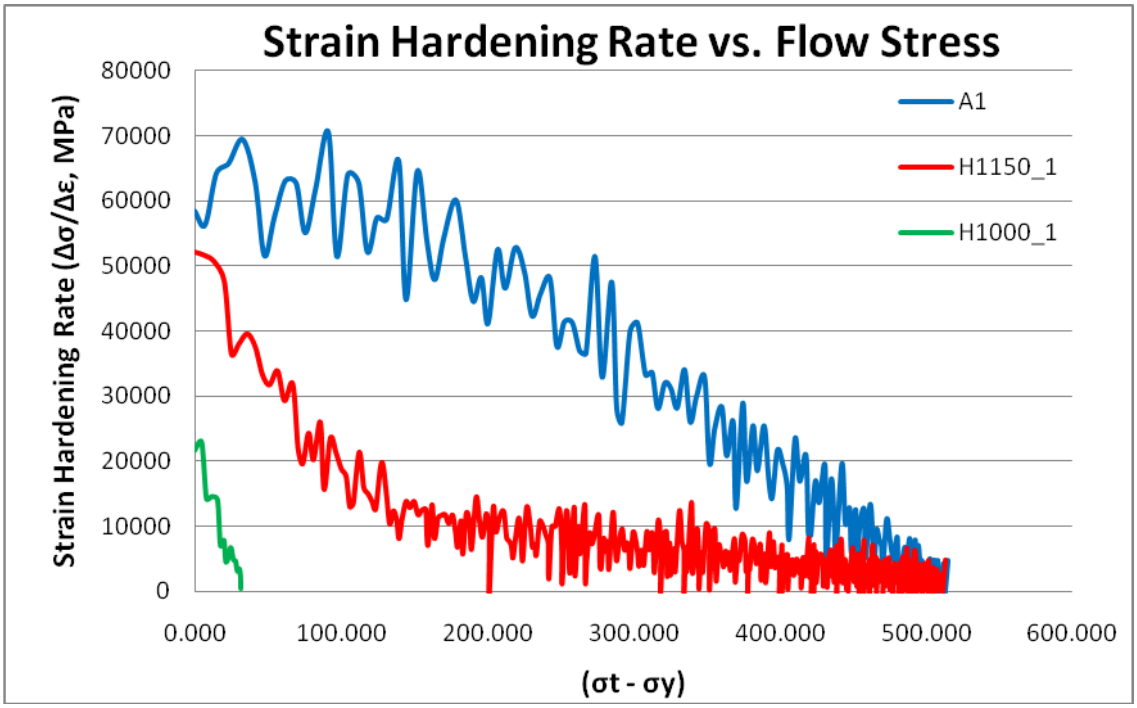

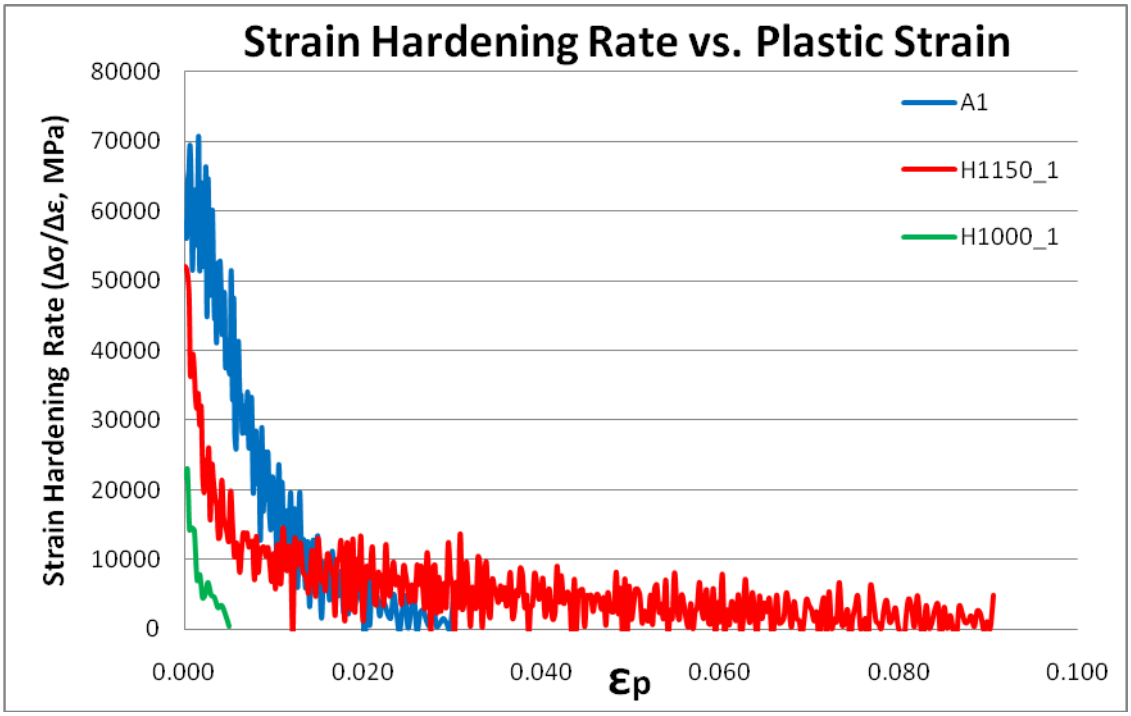

Figure 45: Strain Hardening Rates of Different Tempers of PH 13-8Mo
Only one sample of each temper has been shown to increase clarity.

The strain hardening rate of the H1000 condition is extremely low and short-lived compared to the SA and H1150 conditions. The strengthening effect of the nm-sized NiAl precipitates, a result dislocations either cutting or pulling through the precipitates, inhibits dislocation motion significantly, leading to an extremely high yield stress. In addition, whatever dislocations remain from the martensitic phase transformation will aid in strengthening. Once plastic flow begins, there is little to impede the motion of such a large density of dislocations resulting in fracture at low engineering strains compared to the SA and H1150 conditions.

In the SA and H1150 conditions, strain hardening is significantly higher. In the SA condition, which possesses the highest strain hardening rate of the three, the dislocations from the martensite transformation have a different Burgers vector than the dislocations introduced from the tensile stress. This results in an extremely high strain hardening rate since the only dislocations that contribute to annihilation are the ones produced by the tensile stress. For the H1150 condition, the higher strain hardening rate is a result of thermal recovery, the growth of the soft austenite phase, and the coarsening of the precipitates. These effects result in little dislocation motion inhibition (low yield stress), but allow the generation and motion of a large number of dislocations without causing microvoid coalescence (typical dimple rupture in a ductile failure).

K_{IC} Testing

K_{IC} testing was performed on two uniaxial closed-loop servo-hydraulic loading frames. According to ASTM E399 (36), fracture toughness is determined first by constructing a 95% slope intercept line in the load displacement graph. In the initial case, the load where the 95% line intercepts the load-displacement data, designated P_5, is lower

than the maximum load of the actual load-displacement curve. Thus, the maximum load is the load designated P_Q, and P_Q is input into the stress intensity factor equation. Combining the compliance equations, Equations [11-13], with the appropriate stress intensity equations for the CT specimen, Equations [10-13], K_Q was determined to be approximately 103 MPa-$m^{½}$ (94 ksi-$in^{½}$). The requirement for a specimen to meet plane strain fracture toughness is:

$$B,a,W\ldots. > 2.5\,(K_Q/\sigma y)^2 \qquad [18]$$

The smallest characteristic dimension of the specimen (thickness, crack length, width, etc.) must be at least 2.5x the size of the plastic zone to provide sufficient elastic constraint. If this requirement is met, then $K_Q = K_{IC}$. One sample of PH 13-8Mo in the H1000, SA, and H1150 conditions were fractured. The SA and H1150 condition samples were side grooved because of their extremely low yield strength in order to promote as much elastic constraint as possible. It was predicted that these samples would not meet the requirements for plane strain. In fact, the 95% slope intercept line did not correspond to the maximum loads observed in the SA and H1150 conditions because of the amount of ductile fracture occurring. Because no valid K_Q was reached by the ASTM standards, P_5 was used to determine a K_Q value that is significantly smaller than the true fracture toughness, as the sample size is too small to permit appropriate K_{IC} values for the SA and H1150 conditions.

Table 10: Fracture Toughness Testing Data of the Different Heat Treatments

Sample	K_Q^* (MPa-m ^{½})	K_{IC} (MPa-m^{½})	Plane Strain Met?
H1000-1	103	103	Yes
SA-1**	330	-	No
H1150-1**	270	-	No

*Compliance corrected using Eqs [12-13]
** K_Q calculated at dP/dV ~0 on force-displacement curve (max load).

Despite meeting plane strain fracture toughness requirements, the PH 13-8Mo in the H1000 condition showed some shear lipping. The fracture toughness specimens are shown below:

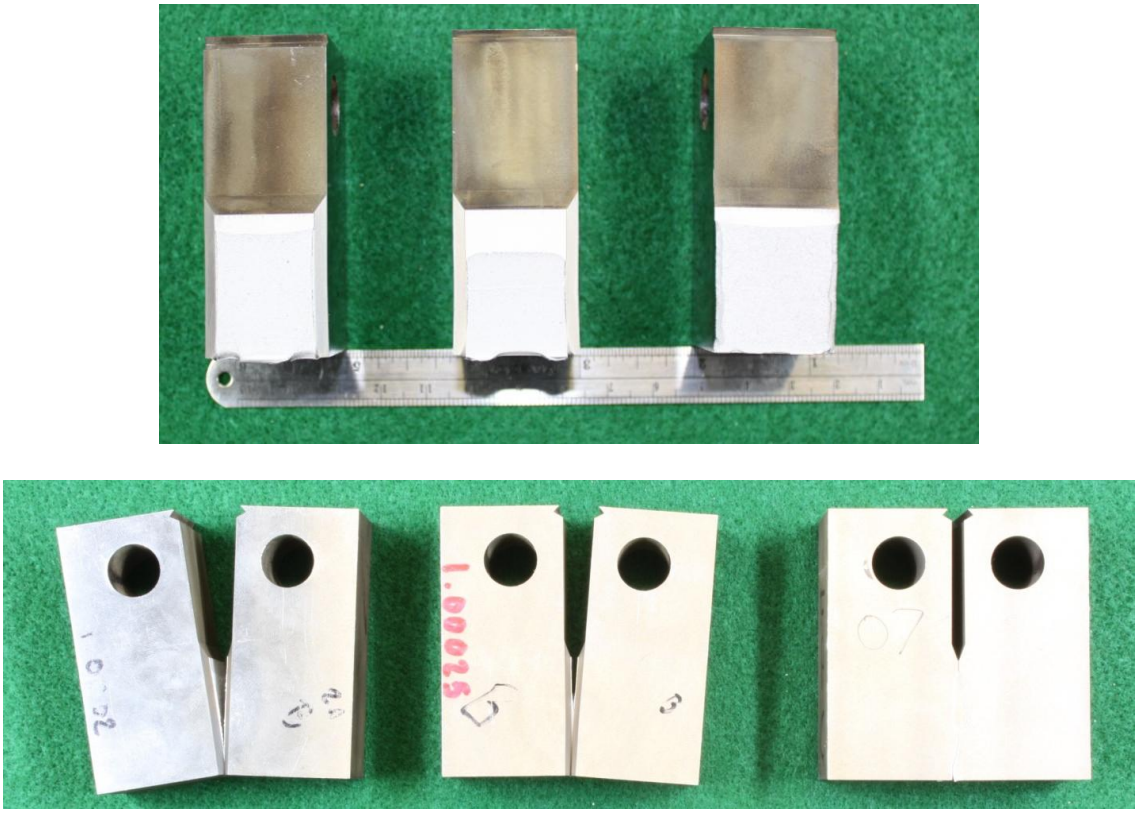

Figure 46: Fracture Toughness Specimen for the SA, H1150, and H1000 Conditions.
Note: the SA (left), H1150 (center), H1000 (right). The H1000 is actually fractured.

Failure Criterion and the Stress-Intensity vs. Life Curve

It is well established that environmental factors have serious effects on the behavior of materials. Not only are typical mechanical properties of interest, such as tensile properties (Young's Modulus, yield stress, ultimate tensile stress) and fracture toughness, but also properties under a given environment – yield strength has a function of temperature, stress corrosion cracking (SCC) fatigue and stress-intensity limits, etc. Determining the point of crack initiation is of utmost important because naval aircraft are designed around crack initiation rather than fatigue behavior. Thus when measuring load, displacement, and K versus time, the resulting time to crack initiation will be *extremely* sensitive to the behavior of each parameter. Furthermore, the term "life" used herein refers to the time required for crack initiation. Used in other mechanics fields, the term "life" can carry a very different meaning and thus must be explicitly defined.

Load and displacement data are recorded as a function of time and then converted in to K via Equations [10-13]. At each point in time, the load and displacement are input into the compliance equation, Equation [12], which produces the nondimensional variable U.

$$U = \frac{1}{1 + \sqrt{\frac{E' V_m B_e}{P}}} \qquad [12]$$

U is then input into Equation [13], which yields an effective a/W value:

$$\frac{a}{W} = 1 - 4.5U + 13.157U^2 - 172.551U^3 + 879.944U^4 - 1514.671U^5 \qquad [13]$$

With a/W, the appropriate stress intensity factor is computed using Equation [11]:

$$Y = \frac{2+\frac{a}{W}}{(1-\frac{a}{W})^{\frac{3}{2}}} * (0.886 + 4.64\left(\frac{a}{W}\right) - 13.32\left(\frac{a}{W}\right)^2 + 14.72\left(\frac{a}{W}\right)^3 - 5.6(\frac{a}{W})^4$$

[11]

Finally, K can be calculated by either of Equation [10a] or [10b] – [10b] is used in this case:

$$K = \frac{YP}{B\sqrt{W}} \quad [10b]$$

Upon the initial loading step, the predicted a/W differs significantly from the measured a/W because small loads produce almost no measureable displacement. Once a sample reaches its final load, the Equations [12-13] predict a/W very well. The compliance equations continue to hold, even once crack initiation has occurred inside the HCl environment. Post-failure samples were broken open and the crack length was measured by optical comparator. The final record of load and displacement were input into the compliance equations and the resulting a/W, compared to the as-measured values, differed by less than 10% for all specimens. Typically the compliance equation for front-face C(T) specimens holds well up to a/W = 0.8 (a < 43mm).

Table 11: Comparison of Measured and Predicted Crack Lengths

Sample	Avg Ao (mm)	Avg Af (mm)	Compliance Af (mm)	% Difference	a/W > 0.8?
H1000_18	26.3	28.6	31.1	-8.5%	no
H1000_22	26.2	28.2	30.5	-8.0%	no
H1000_17	26.2	28.6	30.2	-5.8%	no
H1000_13	26.4	50.4	47.7	5.4%	yes
H1000_14	26.4	47.5	46.5	2.2%	yes
H1000_12	26.2	50.4	46.9	7.0%	yes
H1000_11	26.1	50.4	47.4	6.1%	yes
H1000_21	26.2	28.7	28.7	0.1%	no
H1000_9	26.2	29.5	31.5	-6.8%	no
H1150 HE	**29.2**	**29.6**	30.5	-2.9%	no

H1000_20	26.3	32.5	32.6	-0.3%	no
SA HE2	**26.6**	**27.3**	27.7	-1.5%	no
H1150 HE2*	**26.39**	-	27.88	-	no

*The final crack length for the H1150 HE2 sample was unable to be determined unambiguously either visually or under SEM.

While this difference is quite sizeable, the amount of data available to determine representative values of fracture toughness and elastic modulus limit the accuracy of the compliance equation predictions. In addition, reactions with environment will have a considerable effect on how the crack grows.

Initial sample loading is identical to any type of K_{IC} test – with the exception that the goal is not to fracture the sample. Because of the bolt-loaded nature of the test system, however, the load falls as the crack grows. Typical load- and displacement-time curves (taken from Sample 11) are shown below:

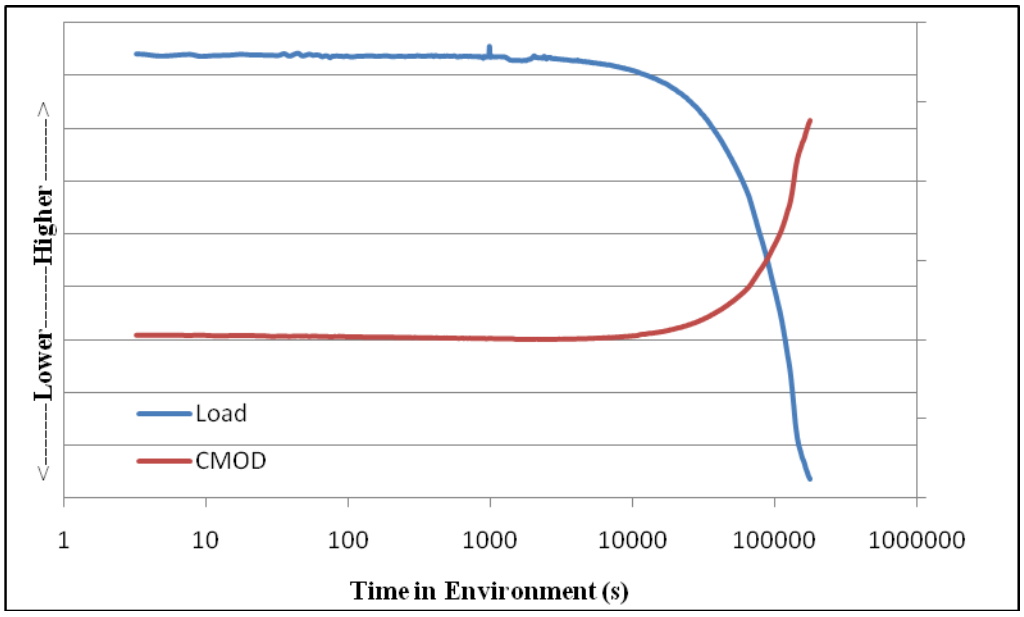

Figure 47: Typical Load- and Displacement- Versus Time Behavior.

The decreasing load and increasing displacement produce offsetting effects - a decreasing load decreases K, but an increasing CMOD increases K; the net result is that K remains relatively constant for some time, as can be seen in Figure 48. Once large crack extensions are achieved, the stress intensity factor (Y in Equation [11]) rises faster than the load drops. As a result, K effectively increases with time. However, after sufficient time has passed (and the crack has further extended), the load begins to drop faster than the stress intensity factor rises, and K falls with time to near-zero levels until the crack has run completely through.

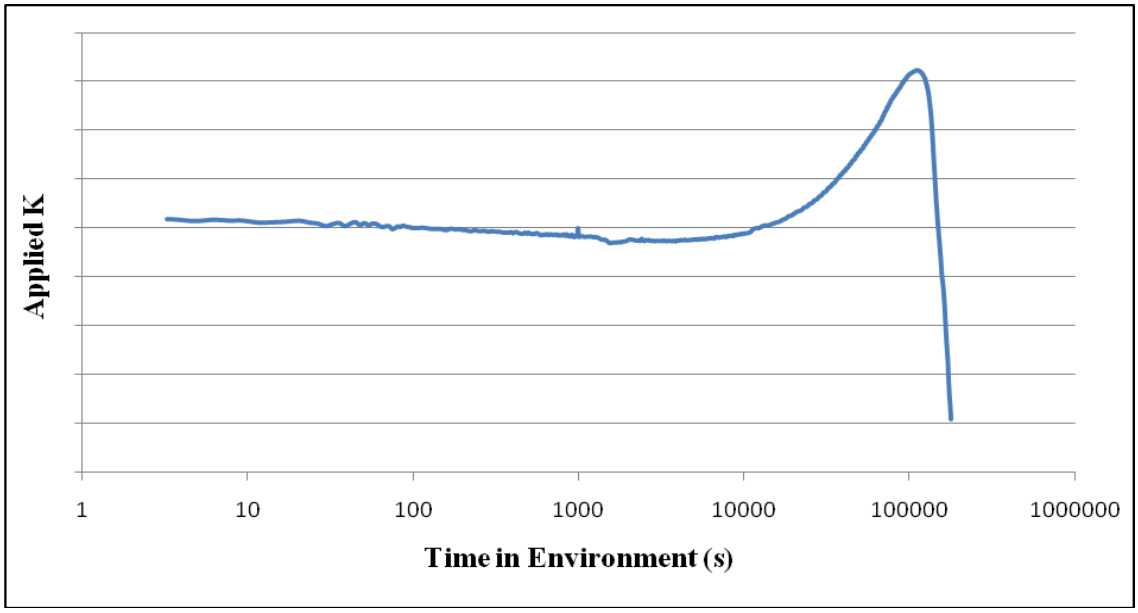

Figure 48: Typical Stress Intensity versus Time behavior.

Presented below are the load-, displacement-, and K-versus time curves for each specimen tested in the H1000 condition. Each sample has been identified by the percentage of K_{IC} to which it was loaded.

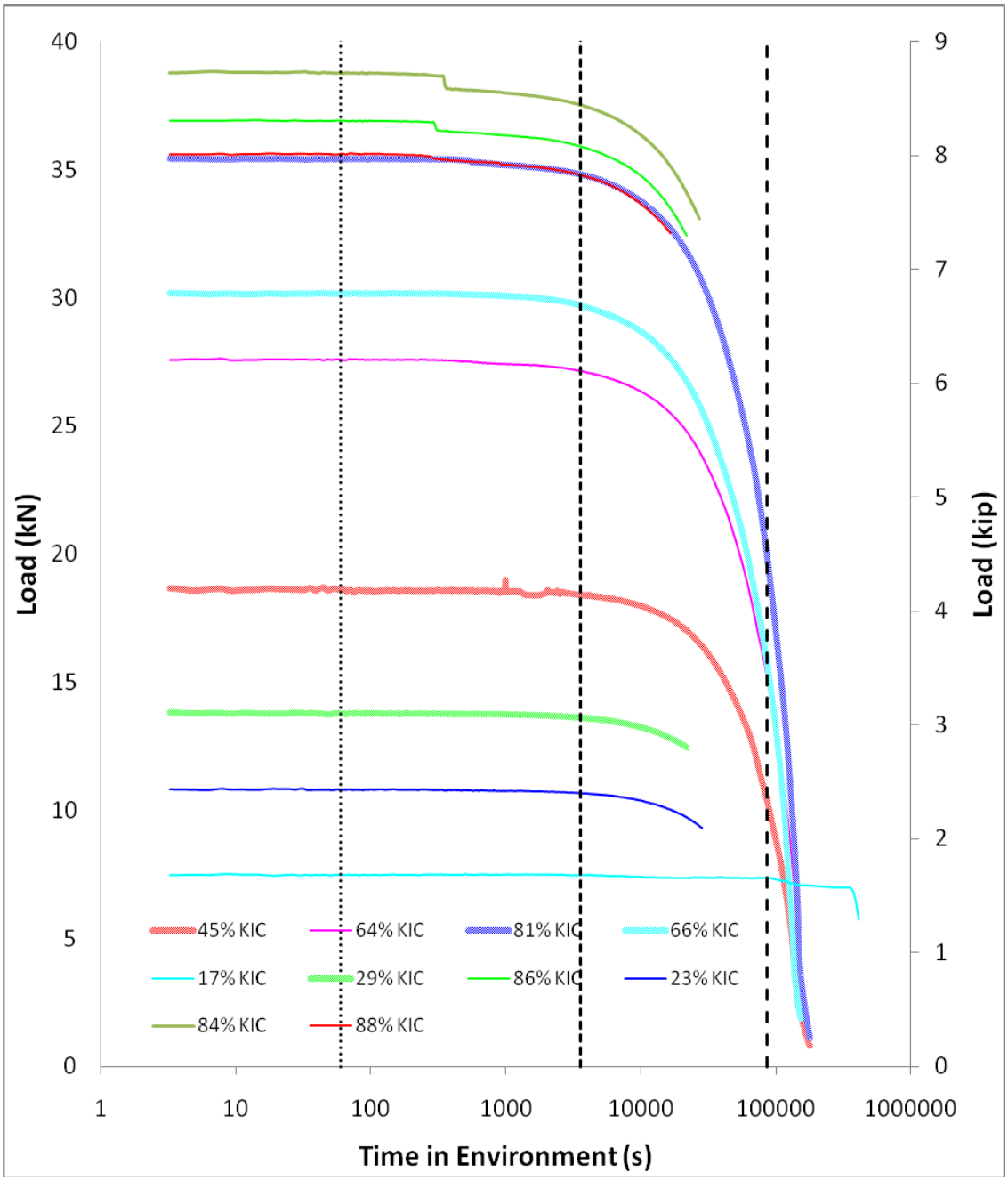

Figure 49: Load Versus Time Curves for all H1000 Samples.

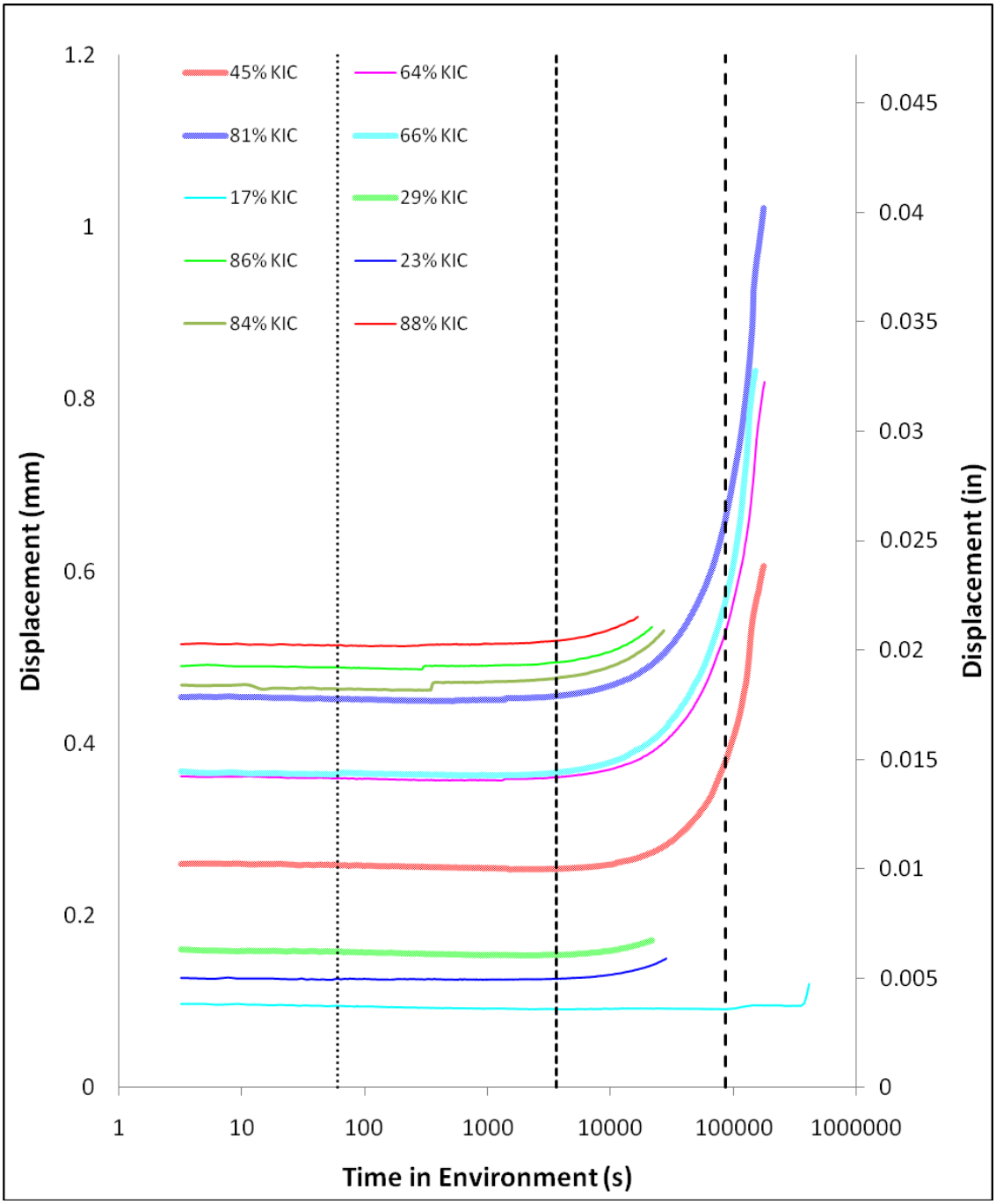

Figure 50: Displacement Versus Time Curves for all H1000 Samples.

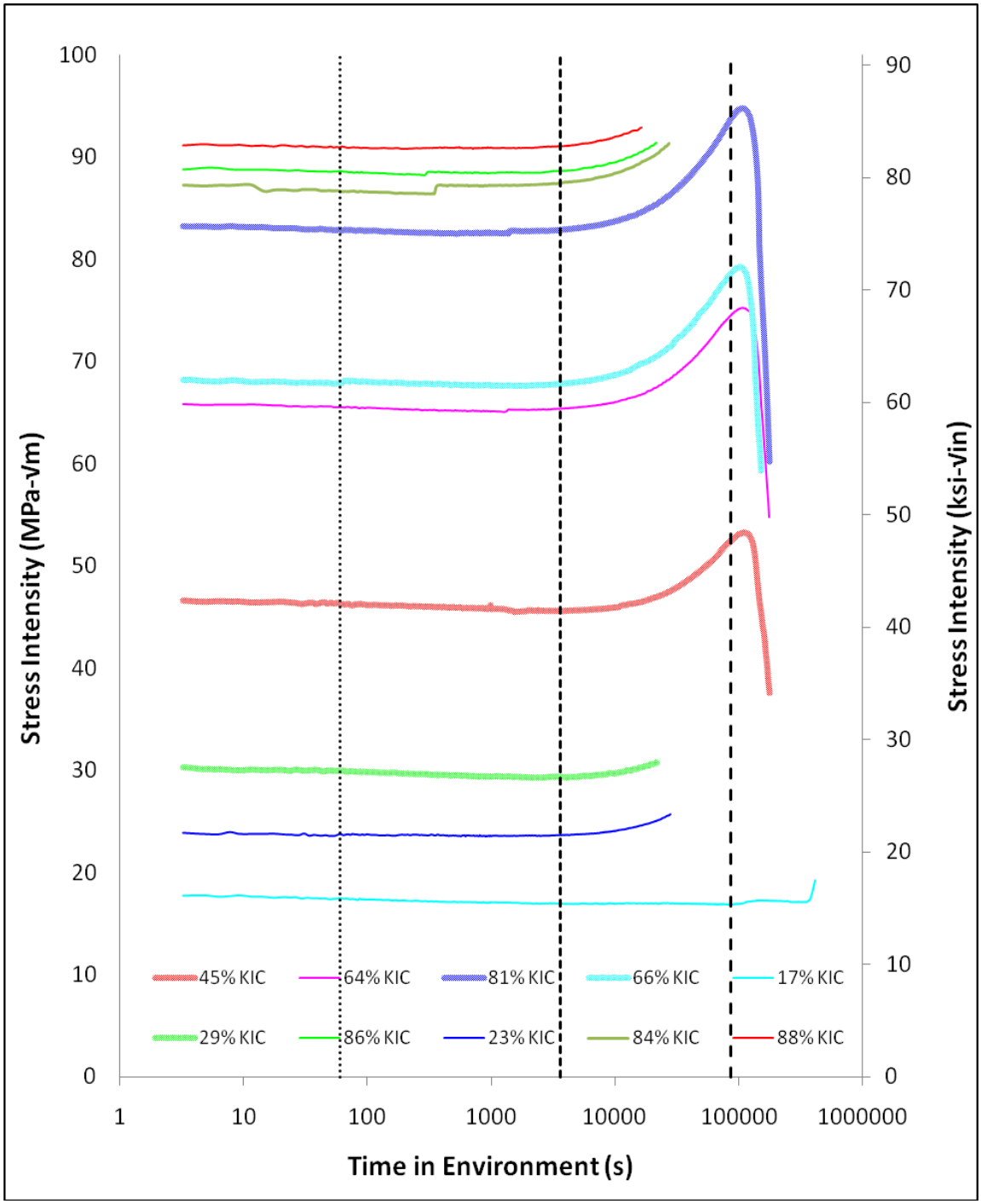

Figure 51: Stress Intensity versus Time Curves for all H1000 samples.

Stress Intensity (K) Failure Criterion

Since the objective is to determine a Stress Intensity versus Time to Crack Initiation (Life) curve, one may be tempted to examine the K-versus time curve, Figure 51, in order to derive an appropriate failure criterion. In examining Figure 51, it appears as though the time for crack growth is extremely large – even samples at the highest of K levels appear to have crack initiation times on the order of 10,000 seconds (about 3 hours). If one were to determine failure criterion solely based on the K behavior, several criteria immediately come to mind based on the behavior shown in Figure 51 – the first is defining the time to crack initiation as the time at which the peak in K occurs. This method would be the simplest, but would also overestimate crack initiation time the most; the second and third would be the time required for either the first or second derivative (dK/dt or d^2K/dt^2) to exceed some critical level. Finally, absolute and relative (percentage) K-changes could also be used. Samples at low K levels tend to experience a small drop in K before seeing the large rise due to crack extension. Conversely, samples initially loaded to high K levels generally do not see any decrease in K before the rising-K region. All of these criteria are completely valid based on the K-time curves. However, they would tend to overestimate the time to crack initiation as a result of the load and displacement changes offsetting one another. By overestimating the time to crack initiation, this would result in the fielding of parts that may be either severely embrittled or already cracked. Since hydrogen embrittlement often produces sub-surface cracks, the cracks could remain undetectable to standard non-destructive inspection (NDI) methods and pose a significant risk when re-entered into service. Using K might become effective if extremely conservative failure criterion were put in place, but

because K is dependent on both load and displacement, there might be something hidden in the underlying load and displacement data that might be missed if only K were used as a failure criterion. Therefore, basing the lifetime on the K versus life curve appears unacceptable.

If Figures 49 and 50 (the load- and displacement-versus time curves) are examined, they suggest crack initiation may occur much, much earlier – well below 1000 seconds for the samples with the highest K-levels, in fact. It is critical to bear in mind that K is a function of *load and displacement*. Thus any failure criterion derived, rather than being based on K, should be based on the variables of which K is a function. K remains the characterizing parameter at which the time to crack initiation (life) is measured (for example, at a K level of X MPa-$m^{½}$, the life is approximately Y hours) because it takes into account the load and geometry of the specimen. One would not expect two samples of different crack lengths to fail at the same time under the same load, because the resulting K levels are different; however, the times for crack initiation for equivalent K levels *should* be approximately the same if the two sample geometries are similar (two different crack lengths, but still in plane strain). Using load and/or displacement should increase the sensitivity of the failure criterion, particularly since it is known that the load drops and the displacement rises. For samples in the H1000 condition that were loaded to near-K_{IC} levels, transient and detectable load drop occurred on the order of minutes.

The first set of failure criterion is merely a raw percentage of load drop – 1, 3, and 5% load drops were all considered to be failure criterion in order to observe the effects these had on the resulting K-life curve. ASTM F1624, used to determine the threshold

stress intensity value, considers a 5% load drop one possible definition of crack initiation (43).

The second and third criteria are developed from experimental observation while creating the load-time (Figure 49) and displacement-time (Figure 50) curves. The criterion require that either the load drops or the displacement increases by a specified amount (ie, a 100N load drop or a 1mm increase in displacement). As compared to the percentage load drop method, these failure criteria are based on absolute measurements – it does not matter whether the starting load were 5kN or 50kN – a load drop of 180N (40lbf), 310N (70lbf), or 450N (100lbf) must occur for "failure" to be considered. Likewise for the displacement, absolute increases of 0.038mm (0.15mil), 0.057mm (0.225mil), and 0.076mm (0.3mil) are also considered as possible failure points. In Figure 49 detectable load drops occur well within one hour for samples that are loaded above 35kN (the times, in fact, are only on the order of a few minutes). These load drops were on the order of ~130N+ and were accompanied by a clip gage displacement of approximately 0.00381mm. Because the sensitivity of the load cell is approximately +-180N (40lbf), based on raw data on a stressed C(T) out of solution, a 180N load drop was chosen as the minimum value for the absolute load drop criterion, as opposed to ~130N which was experimentally observed. As a note to the reader, should one average the load reading at 100-1000Hz over the period of 1 second, the accuracy of the resulting load readings would increase greatly and the +-180N load variation would be eliminated from the signal. The observed variance is simply a result of the low sampling rate used experimentally (2 Hz) and could be easily rectified.

Over extended periods of time, relaxation within the load train can occur.

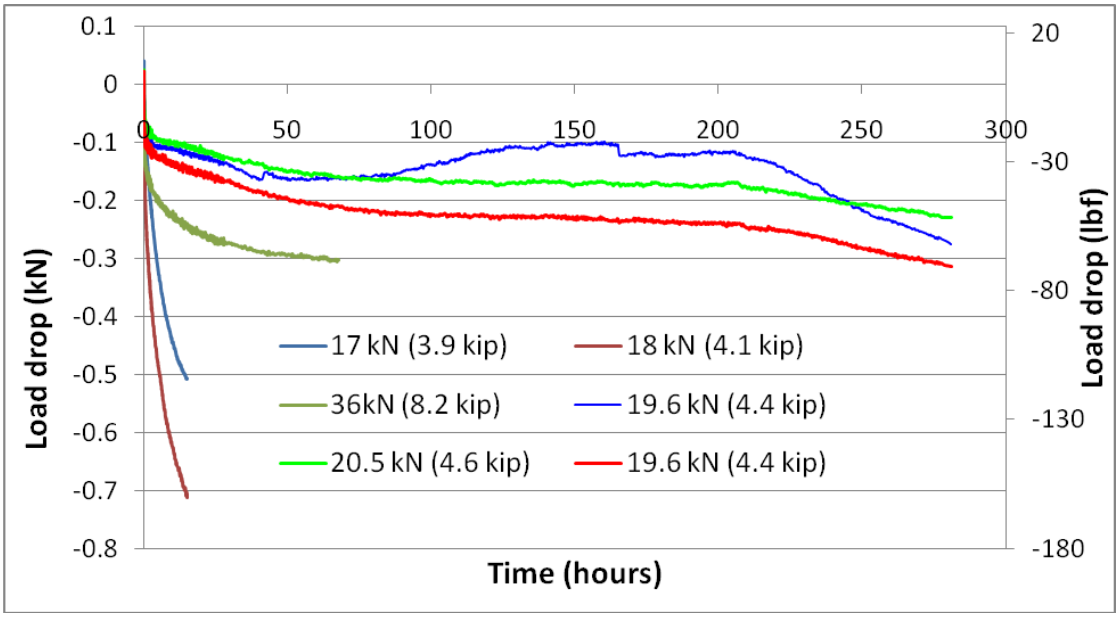

Figure 52: Load Relaxation in Specimens Stressed in Air.

This relaxation was measured by placing a sample under load in air and recording the load and displacement as a function of time. The load drop (current load minus initial load) is plotted as a function of time. Preliminary tests showed that, at loads of ~36kN, ~18 kN and ~17 kN, load relaxations of approximately 240N, 720N, and 580N occurred over a period of 15 hours, as shown in the graph above. Subsequent tests were run with approximately the same loads (19.6, 20.5 kN). Load relaxation in these tests was minimal – over the course of nearly 12 days, the largest load drop of the three tests was 310N (100lbf). This behavior suggests that some of the "slack" in the load train – friction along walls, etc. is reduced as the number of tests increases on any given frame. Furthermore, it complicates the corrections made to the load-time and CMOD-time data – if the relaxations change as more samples are run, how can they be accounted for properly? Ideally, there would be no relaxation in the load train whatsoever. For future testing, it may be preferable to load several dummy samples in air before proper

hydrogen embrittlement testing in order to limit relaxation effects. Alternatively, relaxation could simply ignored – as will be shown later, the uncorrected failure criterion data is actually more conservative than relaxation-corrected data (with one exception).

Clip gage data from these relaxation tests also showed that the clip gage closed over time.

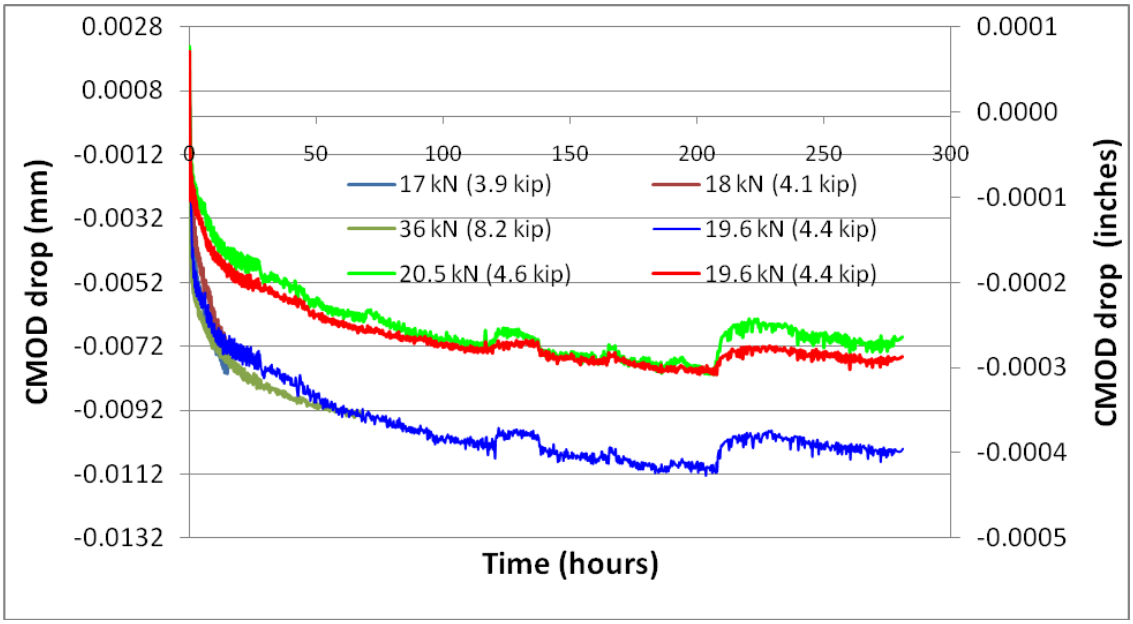

Figure 53: CMOD Relaxation in Specimens Stressed in Air.

This is likely the result of the load relaxing within the C(T) specimen, causing the clip gage to close. Samples immersed in the acid environment can also experience crack closure, which is an entirely separate phenomenon from load relaxation. Crack closure occurs when the surfaces of the crack come in contact while under tensile loading as a result of plastic deformation or oxide formation around the crack tip (5). In order to limit the effects of both the load relaxation and any potential crack closure, the absolute clip gage displacements of 0.038mm, 0.057mm, and 0.076mm are measured the minimum point on the CMOD versus time curve.

In addition, the as-measured load- and CMOD versus time curves were corrected based on the data gathered from the C(T) samples stressed in air. This was done by measuring the load and CMOD drop as a function of time. Using the worst-case-scenario relaxation data (18kN data from Figures 52 and 53), the corresponding drops in load and displacement as a function of time were subtracted from the original load and displacement curves. This had a negligible effect on the K-versus time behavior – the applied K for all samples tested changed nominally by 1 MPa-$m^{½}$, which is relatively insignificant. However, as will be shown later, these corrections have a dramatic effect on determining when "crack initiation" occurs based on the differing failure criterion.

The greatest weakness to using a single failure criterion is that each definition of failure will yield different results. Is it important, when defining failure, to compare various criteria and determine which combination is most appropriate. For engineering, component failure is examined in a conservative manner – safety factors limit stress (or stress intensity) to some fraction of the yield stress, fracture toughness, or fatigue life. Thus, the safest failure criterion examined here will be the one that generally yields the most conservative results. It is also expected that the K-Life behavior should roughly follow the shape of Figure 1. As a reminder to the reader, the K-Life curve is only being constructed for PH 13-8Mo H1000.

Each of the individual failure criteria:

1) percentage load drop
2) absolute load drop
3) absolute clip gage displacement

will now be discussed and compared with one another, leading up to the establishment of the full Stress Intensity vs. Life (time to crack initiation) curve.

Percentage Load Drop: Failure Criterion I

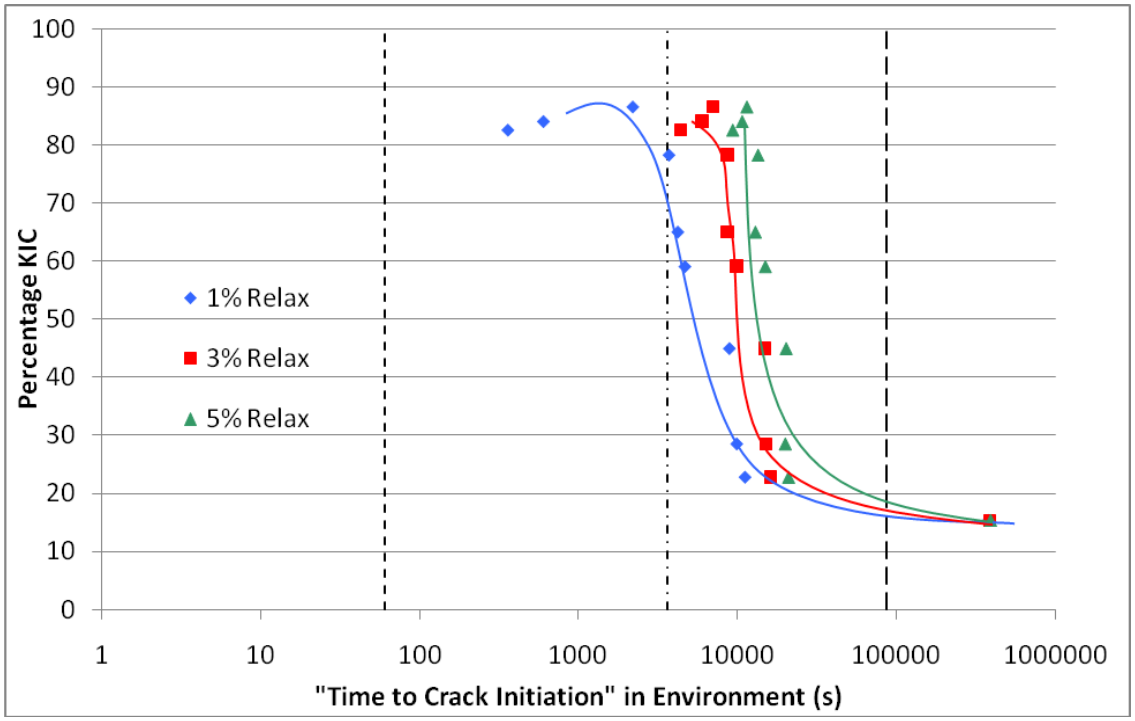

Figure 54: Time to Crack Initiation for Percentage Load Drop Failure Criterion

Beginning with the failure criterion of a percentage load drop, large amounts of scatter only appear to exist at the highest fractions of K_{IC}, where a sample would intuitively be most sensitive to the environment, loading conditions, and the "true" K_{IC} (statistical mean and distribution of a population's K_{IC} values). Because only one K_{IC} measurement was made, there is no ability to determine how large a variance of K_{IC} values exists within the sample set tested. This means that the samples loaded to 86% and 84% K_{IC} might really have been loaded to 90%+ of the real K_{IC} – giving rise to a

significantly shorter time measured for a 1% load drop. As a trend, below 80% K_{IC} and above 20% K_{IC}, it appears as though the time required for crack initiation (for any given % load drop) is more or less constant. This means that the slope of the line in Figure 1 is extremely large – nearly infinite – and the time difference between fracturing just below K_{IC} (~80% K_{IC}) and far below K_{IC} (~20-30% K_{IC}) is relatively small. This would indicate an extreme sensitivity to the combination of imposed stress and an aggressive outside environment. While PH 13-8Mo is a stainless steel, HCl is an aggressive environment, and it has been noted by Hirth that aqueous hydrogen environments can be more damaging that gaseous ones (10). As the definition of "crack initiation" increases to 3% and 5% load drops, the times required to achieve these load drops increase in their variation (the standard deviation increases). However, the time *between* load drops becomes more uniform (the standard deviation of these differences decreases).

Table 12: Time Changes Between Percentage Load Drops

% K_{IC}	**1% to 3%**	**3% to 5%**
88	4216	3939
86.2	3844	4242
84.4	2540	4292
80.6	4595	4437
65.9	3636	3937
63.6	4444	4584
45.1	7524	5020
29.2	4798	4725
23.3	5202	4380
Mean	**4533**	**4395**
Std. Dev	**1361**	**352**

This can be observed especially well when samples above 20% K_{IC} are analyzed (the sample at 17% K_{IC} tends to skew the data because its times are so long, though the trend remains). This suggests that whatever mechanism is responsible for *propagating the crack* is largely *stress independent* and is equally effective between 80% and 20% K_{IC}.

Below 20% K_{IC}, the time for failure is quite significant –a 1% load drop requires times near 10,000 seconds (~3 hours) and greater than 10^5 seconds (about 30 hours) for a 3% load drop. Once the effects of load relaxation are taken into account, the graph in Figure 54 gets shifted to the right and the overall shape of the curves for 1%, 3%, and 5% load drop remain identical to their uncorrected counterparts.

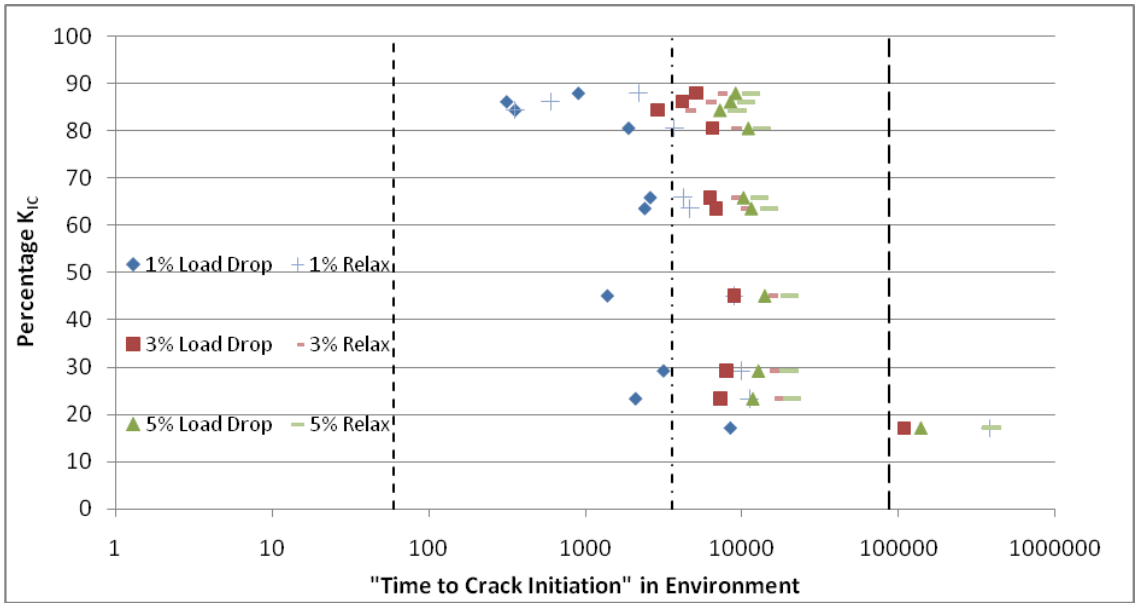

Figure 55: Time to Crack Initiation for Percentage Load Drop Failure Criterion (Relaxation Adjusted)

Samples above 80% K_{IC} were mostly unaffected at the 1% load drop level because crack extension was more or less immediate and there was insufficient time for

the system to relax. For all other samples and load drops (1/3/5%), the effects of relaxation were dramatic – at 80% K_{IC} the time required for a 1% load drop was increased by 1800s (½ hour), while at 17% K_{IC}, the time for 1% load drop was increased by 30000s (8.3hrs). These differences tended to increase as the load drops changed from 1 to 3 to 5%.

Absolute Load Drop: Failure Criterion II

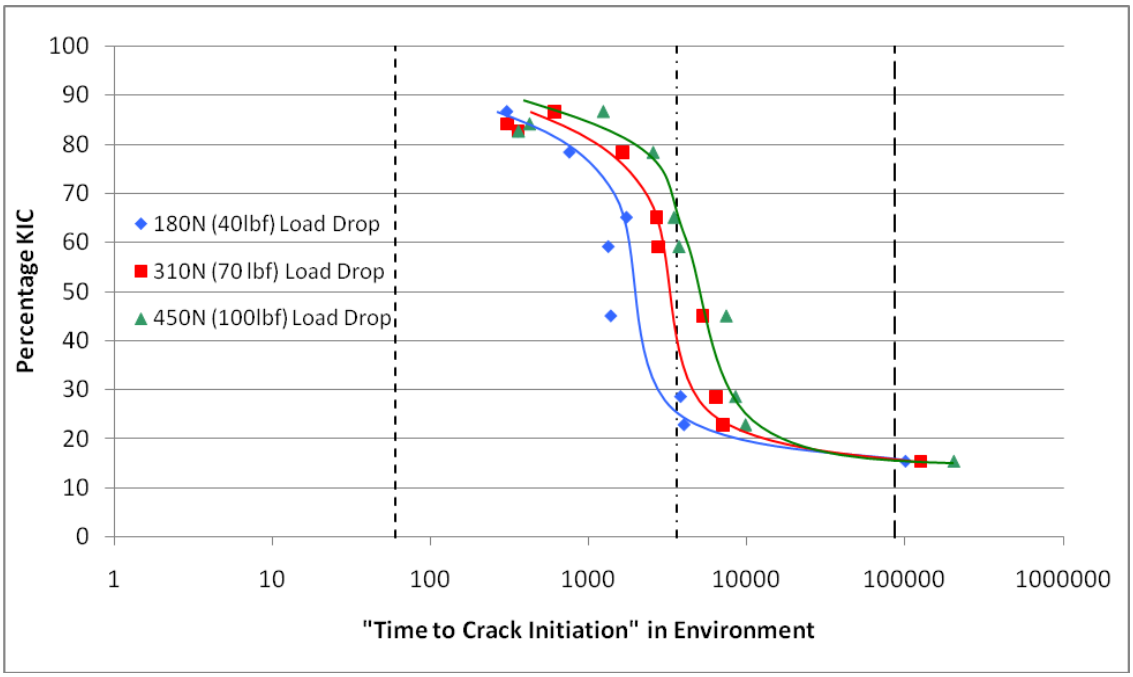

Figure 56: Time to Crack Initiation for Absolute Load Drop Failure Criterion

The second failure criterion required that an absolute load drop of 180N, 310N, or 450N (40, 70, and 100lbf, respectively) must occur in order for a crack to have "initiated." While crack initiation times remain on similar orders of magnitude for all applied percentages of K_{IC} as compared to the previous failure criterion, utilizing absolute load drops as a criterion for crack initiation yields a greater degree of curvature in the K-life relationship. Lifetimes are also 50-70% shorter for similar fractions of K_{IC}.

This, as well as the increased curvature, is likely a result of the fact that for large fractions of K_{IC}, 180/310/450N are smaller than 1/3/5% of the applied load, so a shorter measured lifetime is not unexpected. Likewise, at the lowest fraction of K_{IC} (17.1%), 180/310/450N are *larger* than 1/3/5% load drops, which results in lifetimes that are larger by several hours at all levels. Furthermore, the crack initiation times above 80% K_{IC} appear more sensible. Under the previous criterion, the sample at 88% K_{IC} took a longer time for a 1% load drop than samples at 86 and 84% K_{IC}. Using an absolute load drop, however, crack initiation times are equal for the samples loaded to 88 and 86% K_{IC}. Interestingly, however, subsequent times for 310 and 450N load drops are still higher for 88% K_{IC} than 86 and 84% K_{IC}. This could be the result of crack blunting and plastic zone effects around the crack time under the hydrogen-rich environment.

Below 80% K_{IC}, the measured crack initiation times are more consistent with the expected result that crack initiation times increase as applied % K_{IC} decrease. The slope of the curve is much more gradual, rather than a sharp drop observed previously. For a 180N load drop, the sample at 66% K_{IC} has a greater time to crack initiation than samples at 64 and 45% K_{IC}. Beyond these first 180N however, the 66% K_{IC} sample has shorter times to reach the 310 and 450N load drops, and the expected result is satisfied.

What is most interesting about the absolute load drop criterion (and reinforced by the previous criterion) is that there is a massive time difference between failure criterion for 23 and 17% K_{IC}, particularly as the criterion limits increase. For a 180N (40lbf) load drop, loading to 23% K_{IC} takes only 4000s (slightly over an hour), but loading to 17% K_{IC} takes 10^5 seconds (over one day) for a similar load drop. This indicates that the driving force for crack extension, under the HCl environment, is dramatically reduced.

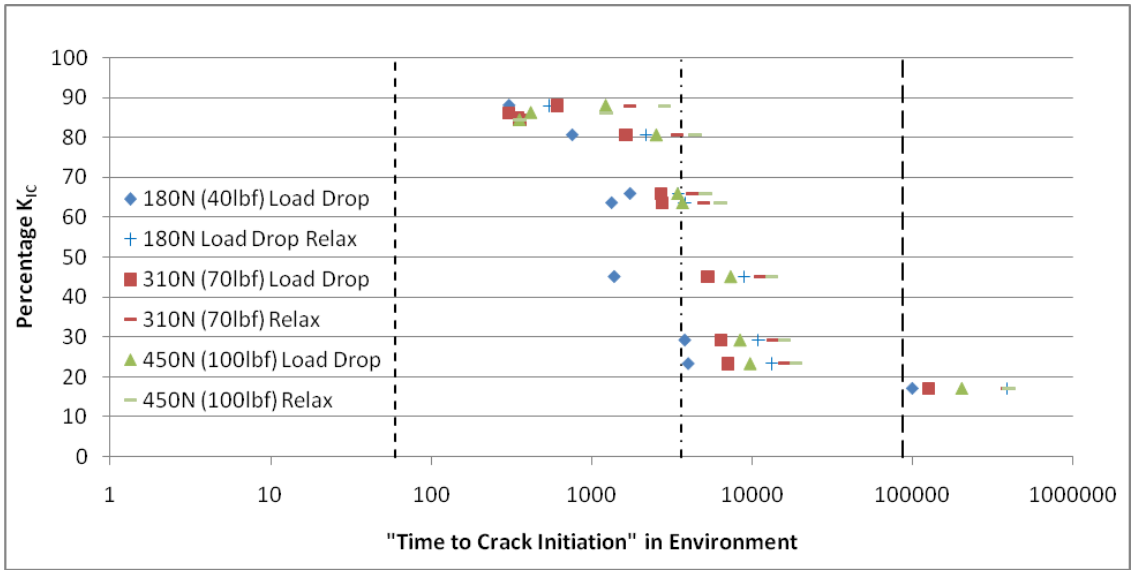

Figure 57: Time to Crack Initiation for Absolute Load Drop Failure Criterion (Relaxation Adjusted)

Once load relaxation is taken into account and added to the Load vs. Time data, the absolute load drop failure criterion is dramatically changed. For a 180N load drop, sample lifetimes doubled across the board, except for those samples loaded above 80% K_{IC}. Because of short time required to extend the crack, these samples were not affected by the load relaxation corrected. Post-correction, the sample at 88%K_{IC} returns to possessing crack initiation times greater than samples at lower percentages of K_{IC}. More than likely, this 88% K_{IC} sample has a true K_{IC} greater than the sample measured.

Absolute CMOD Displacement Increase: Failure Criterion III

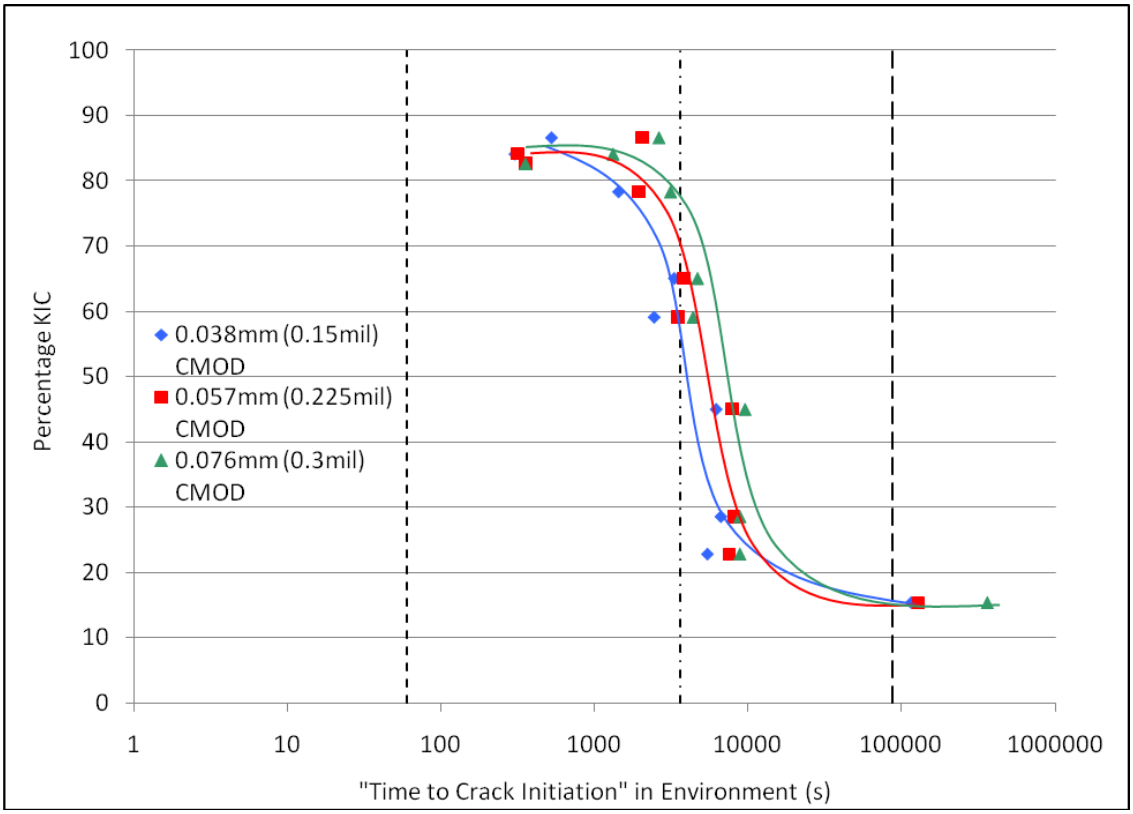

Figure 58: Time to Crack Initiation for Absolute CMOD Failure Criterion

The final crack initiation criterion was that of an absolute change in CMOD. CMOD gages are very sensitive and able to detect displacements on the order of 10um. Like the K-Life curve generated from the absolute load drop criterion (Figure 57), the K-Life curve in Figure 58 has much more curvature to it than the resulting curve from the percentage load drop criterion (Figure 56). Unlike the absolute load drop criterion, where the K-life curve tended to match the expected result quite well, with the CMOD criteria there is a fair degree of variation in the measured results – a sample at 66% K_{IC} has a greater time to initiation than one at 64% K_{IC}, and a sample at 23% KIC has a shorter time to initiation than samples at 29% and 45% K_{IC}. Much of this is a result of load

relaxation, which causes the clip gage to close. CMOD vs Time was adjusted in precisely the same manner that Load vs. Time was – the clip gage closure as a function of time was subtracted from each CMOD vs Time curve. Unlike either of the load drop criterion, where accounting for relaxation lengthened the time to crack initiation, subtracting a clip gage closure *shortens* the time to failure since the criterion is a CMOD *increase*.

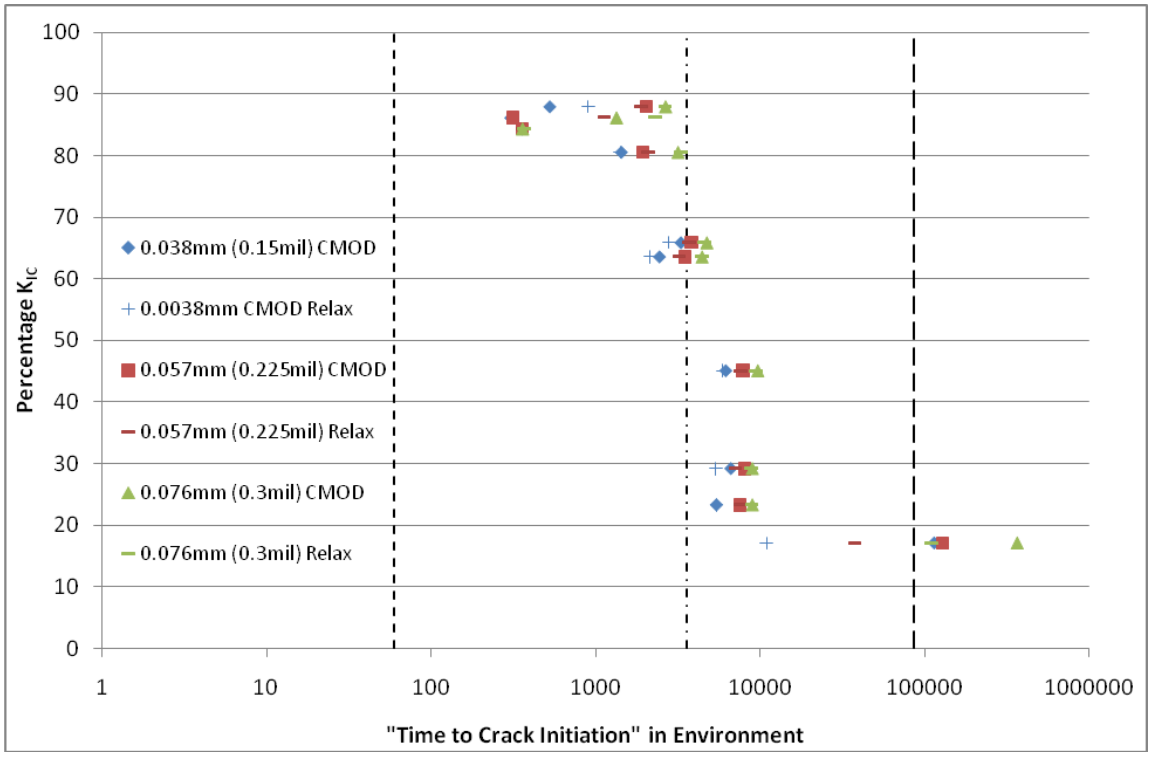

Figure 59: Time to Crack Initiation for Absolute CMOD Failure Criterion (Relaxation Adjusted)

As with the absolute load drop failure criterion, samples above 80% K_{IC} in the CMOD increase criterion are least affected by the load relaxation correction because the time required to achieve the initial 0.038mm CMOD increase was so short. Between 20% and 80% K_{IC}, samples are moderately affected – corrections reduce lifetimes by

1500s (~½ hour) on the bottom end (23% K_{IC}) and only a few minutes (3-500s) at the high end (66% K_{IC}). The sample loaded to 17% K_{IC} is affected the most. While both load drop criterion (relaxation corrected) indicated failure times beyond 10^5 seconds (~30 hours), using an absolute CMOD increase of 0.038mm shows that crack initiation is likely to take place at 10,000s (~3 hours) – a 10-fold reduction in crack initiation time. Initially, it was thought that 17% K_{IC} was approaching the threshold level K_{th}, however the clip gage data indicates that the applied stress intensity must be reduced to even lower levels of K_{IC} to come closer to a measurable K_{th}. As stated previously, Gangloff has stated that the threshold level for hydrogen embrittlement can be as low as 5-10% K_{IC} (2).

Comparison of Failure Criterion and the K- Life Curve

With the various failure criteria examined, it is now necessary to determine which criterion(s) will be used to specifically define "crack initiation." The shortest time from each criterion (1% load drop, 180N load drop, and 0.038mm CMOD increase) will be used as the baseline points. Using larger, less conservative values of load drop or CMOD as defining points for crack initiation could lead to the fielding of a part in which crack initiation has occurred and subsequent in-service loading leads to crack extension or catastrophic component failure, dramatically increasing risk.

Each failure criterion – 1% load drop, 180N (40lbf) load drop, and 0.038mm (0.15mil) CMOD – is shown below in Figure 60. The top graph *does not* account for relaxation in the load train, while the bottom one does. When load relaxation is not taken into account, the 180N load drop criterion is the most conservative, except when K levels are below 30% K_{IC}. In this case, a 1% load drop borders on the ±180N variation in the

load sensor signal. Thus, the next most conservative failure criterion must be used instead. This leads back to the 180N absolute load drop, in which case the entire curve may be simplified and only data from the 180N absolute load drop criterion is used. However, for extremely long tests, where the applied K is near the threshold value K_{th}, load relaxation may account for nearly the entire measured load drop. In that event, it becomes necessary to add a second supporting criterion. Because of the high sensitivity of the clip gage, the 0.038mm CMOD increase is used to support the absolute load drop in events where load relaxation significantly affects the applied load as a function of time.

Once the data is corrected for load relaxation, the CMOD opening becomes the dominant defining characteristic for crack initiation. It is only at the highest applied percentages of KIC that using an absolute load drop remains a viable failure criterion. The most dramatic change occurs at the lowest fractions of applied K_{IC}. Previously, the 1% load drop criterion (despite conflicts with sensor accuracy/precision) indicated the shortest time to crack initiation. With the relaxation correction, a 1% load drop does not occur until ~30 hours. However, a CMOD of 0.038mm is met at just ~3 hours, a ten-fold *decrease* in the defined time to crack initiation. This suggests that threshold stress intensity maybe still be much farther away than previously expected.

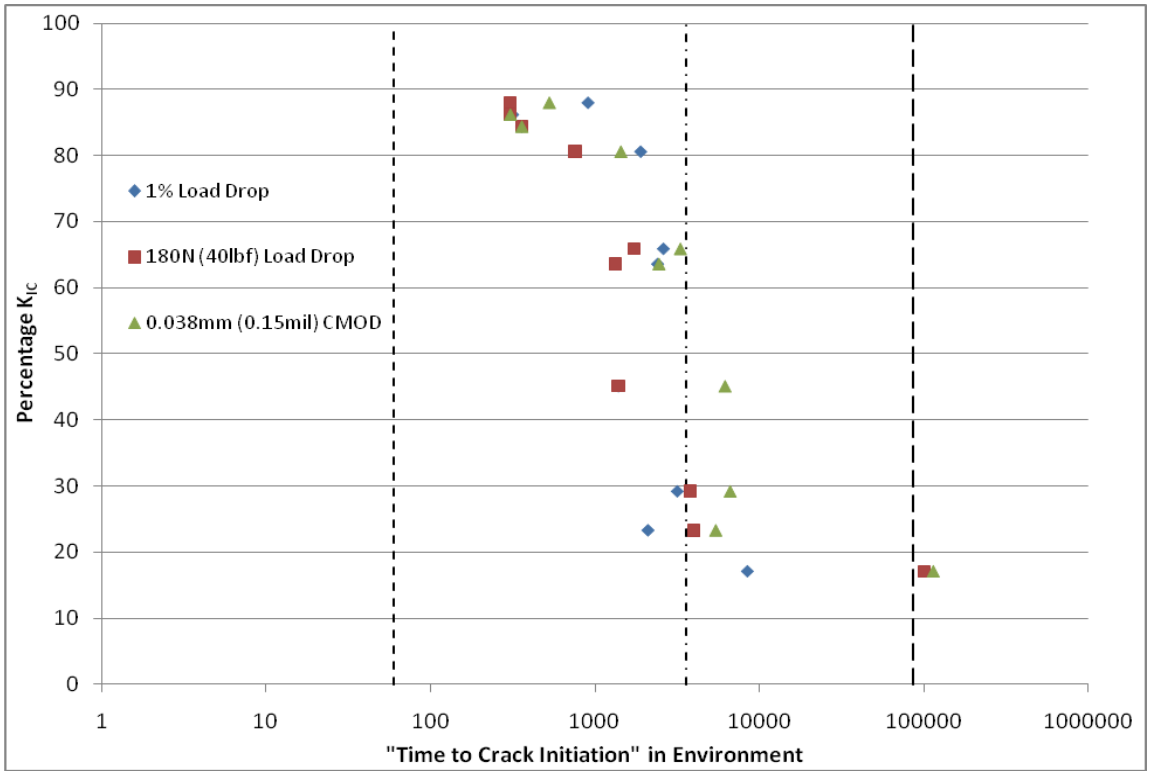

Figure 60: Failure Criterion Comparison – *Not* Relaxation Adjusted

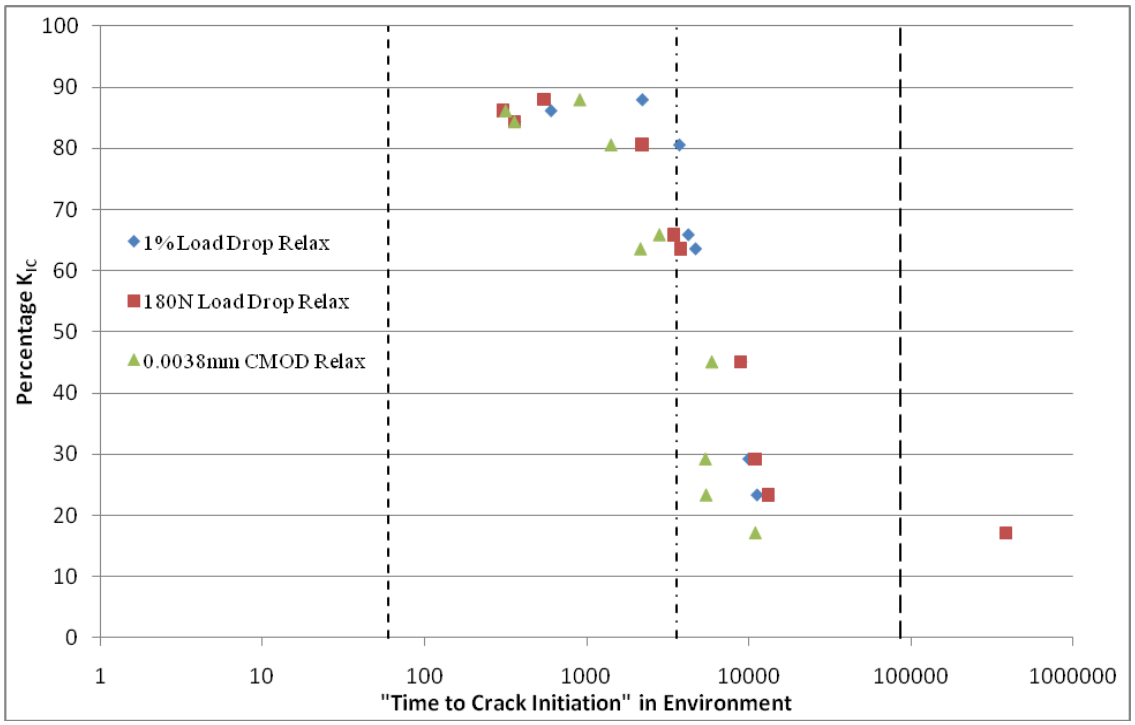

Figure 61: Failure Criterion Comparison - Relaxation Adjusted

The resulting normalized stress intensity (% K_{IC}) versus life curves shown below in Figure 62 for both the relaxation-adjusted and non-adjusted data sets. Interestingly, the unadjusted data proves to be the more conservative set, having equal or lesser times to crack initiation at all fractions of K_{IC} , except at the 17% K_{IC} level. Both curves show that PH 13-8Mo is highly susceptible to the 1M (N) HCl environment under the influence of a remote load. As defined, both curves predict crack initiation in only a few hours or less. This means that, more than likely, crack initiation *will* take place during stripping and plating procedures and the incremental crack growth must be accounted for when determining the useable lifetime of an aircraft component. Additionally, the applied K levels can be converted into applied stress based on equation [10a]. Back-calculating the applied stress can then be used to determine acceptable levels of residual stress for aircraft components or to modify stripping, plating, and reworking procedures in order to prevent crack initiation from occurring in the first place.

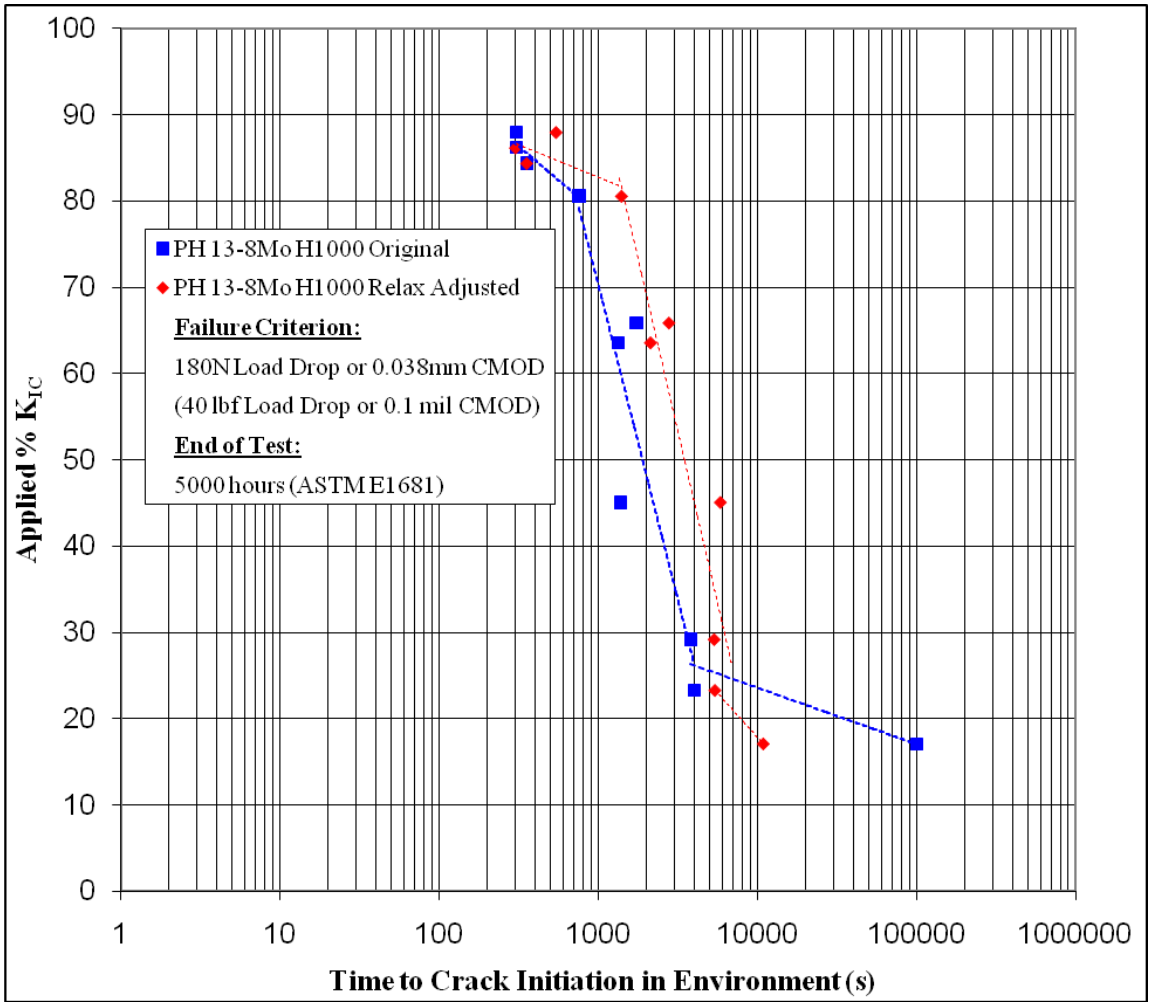

Figure 62: Stress Intensity vs. Life for PH 13-8Mo H1000

Relative Susceptibility of Tempers

Prior research work has shown three general behaviors with respect to hydrogen embrittlement:

1) lower strength materials tend to be less susceptible

2) over-aging tends to improve resistance to hydrogen embrittlement

3) austenite tends to improve resistance to hydrogen embrittlement

PH 13-8Mo in both the solution annealed and H1150 conditions are significantly lower in strength than the H1000 condition. Despite having roughly the same yield and ultimate tensile strengths, the SA and H1150 conditions possess very different microstructures – the SA condition is a supersatured, highly dislocated lath martensite, while the H1150 features NiAl and/or Ni3Mo/Ni4Mo precipitates along with some austenite. To create as even as possible comparison between the three different conditions (SA, H1000, and H1150), the stress intensities of the SA and H1150 tempers were also normalized by their *apparent* fracture toughness values (in the case of *H1000*, K_Q was found to be a *valid* K_{IC} measurement). PH13-8Mo H1150 and SA were too ductile to properly measure their plane strain fracture toughnesses. A table containing the applied percentages of K_Q (SA/H1150) or K_{IC} (H1000) can be found in Appendix A7.

PH 13-8Mo H1000

As the K-Life curve in Figure 62 demonstrated, PH 13-8Mo H1000 is highly susceptible to crack initiation in a hydrogen-rich environment, with crack initiation times on the order of a few hours for the relaxation un-adjusted samples. Because of its high strength and ability to support large elastic stresses, the crack tip in the H1000 was most likely to be in a (plane strain) triaxial stress state. This should result in a large driving

force for hydrogen to diffuse towards the crack tip and weaken the material, causing crack initiation. At applied K levels of greater than 20% K_{IC}, crack initiation times were measured at less than an hour. For stress intensities below 20% K_{IC}, the time to crack initiation became extremely long – measuring approximately 27 hours based on the 180N (40lbf) / 0.0038mm (0.15mil) crack initiation criteria (~3 hours for load and clip gage relaxation adjustments). Furthermore, the threshold stress intensity level, K_{th}, appears on the order of 10% K_{IC}, given that 17% applied K_{IC} yielded a 30 hour lifetime (at best) and K_{th} is defined as a 5000 hour lifetime.

PH 13-8Mo Solution Annealed (SA)

In the SA condition, PH 13-8Mo has a lower yield strength than H1000 (650MPa vs. 1500 MPa) despite its high dislocation martensitic structure due to the lack of precipitation hardening (compared to the H1000 condition). It has much less solid solution hardening compared to a quenched carbon steel. As a result of this lower yield strength, the real fracture toughness is expected to be higher than that of H1000. This has been confirmed but the measured K_Q of 330 MPa$\sqrt{m}$ was not a valid K_{IC}, so the true K_{IC} is likely to lie somewhere between 103 and 330 MPa$\sqrt{m}$.

Dislocations act as weak traps for atomic hydrogen, which can be beneficial in some instances but detrimental in others. Because dislocations are weak traps, hydrogen does not strongly bind to them, reducing the likelihood of developing a locally high concentration of hydrogen atoms. On the other hand, dislocations can transport hydrogen atoms throughout the crystal lattice. If the hydrogen is brought to a grain boundary or carbide particle, the resulting concentration could be sufficient to cause failure.

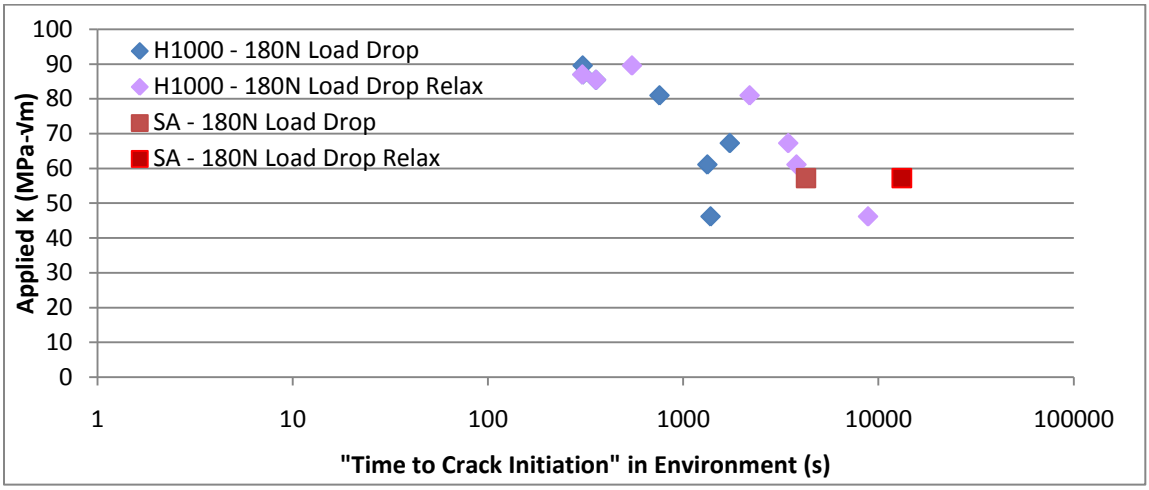

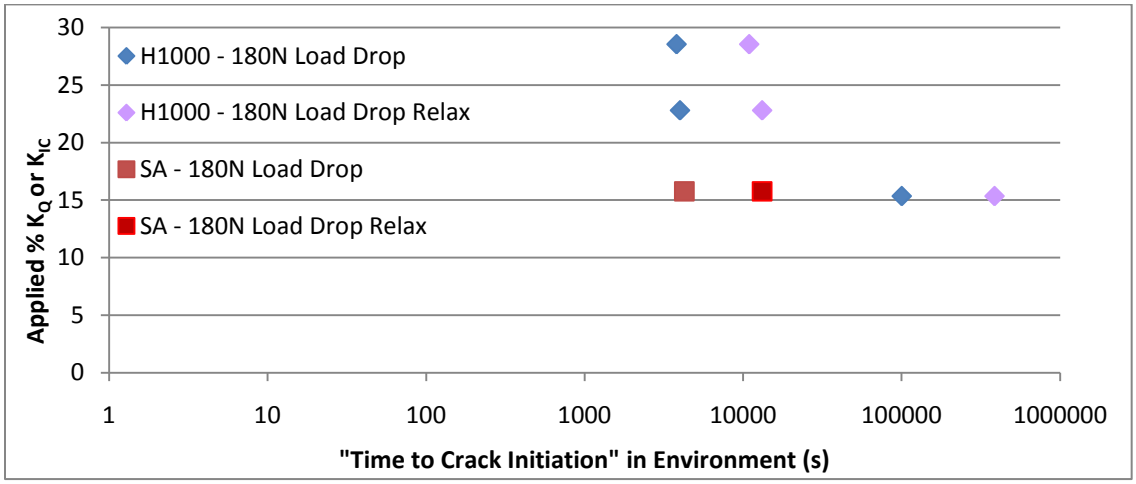

Figure 63: "Time to Crack Initiation" for PH 13-8Mo H1000 and SA

As indicated by Figure 63, the SA condition possesses resistance to crack initiation superior to that of the H1000 condition based on the imposed failure criterion (180N load drop) at equivalent applied K levels. The SA condition is so ductile that its crack is not fully constrained by the surrounding material. It is in neither a state of perfect plane strain nor plane stress. The greater degree of plastic deformation surrounding the crack tip in the SA sample (due to a lower yield stress) means there is lower elastic stress driving hydrogen ingress than an equally stressed H1000 sample.

This could explain the result of a longer time to crack initiation at an equivalent applied stress intensity.

Due to the fact that the measurement of K_Q produced an invalid K_{IC} for the SA condition, its toughness is overestimated, and therefore at equivalent applied *percentages* of K_{IC} (K_Q), the SA appears to possess much worse resistance to HE than a similarly stressed sample of H1000 material. Without measuring a true K_{IC} and testing an appropriately sized sample, however, the conclusions one can draw from this data are limited. Supposing that the true K_{IC} of the SA condition is at most 210 MPa√m (and no geometrical effects from increasing the sample size to support plane strain conditions), this would yield an applied K_{IC} of ~30% for the tested SA sample, whose resistance to HE would then be equivalent to, or greater than, comparable H1000 condition samples at 30%+ K_{IC}.

PH 13-8Mo H1150

Like the SA material, the H1150 is too ductile to maintain a plane strain state surrounding the crack tip; however, its microstructure is significantly different. Precipitates coarser than those of the H1000 condition are present, and the austenite in the H1150 is a strong hydrogen trap.

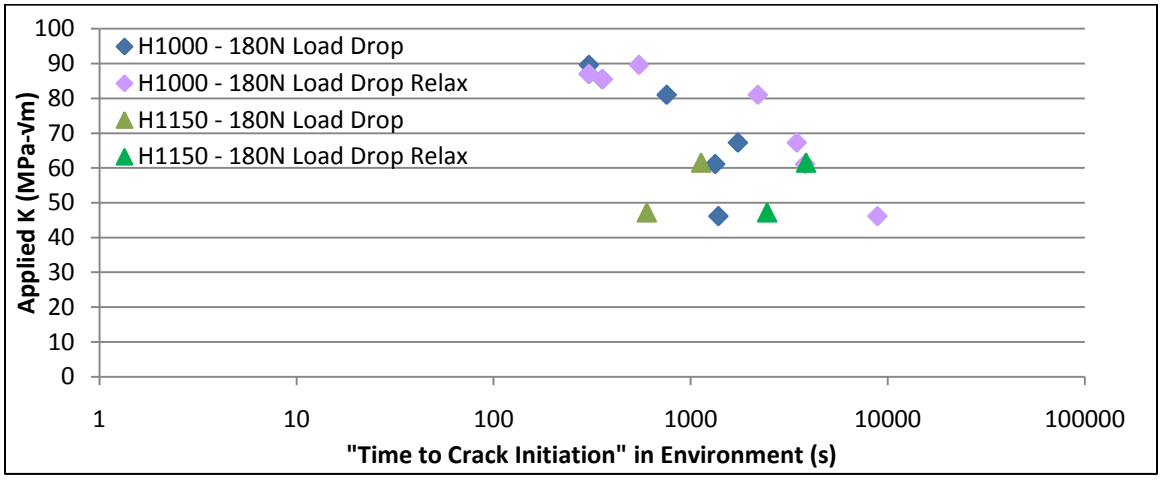

Figure 64: "Time to Crack Initiation" for PH 13-8Mo H1000 and H1150

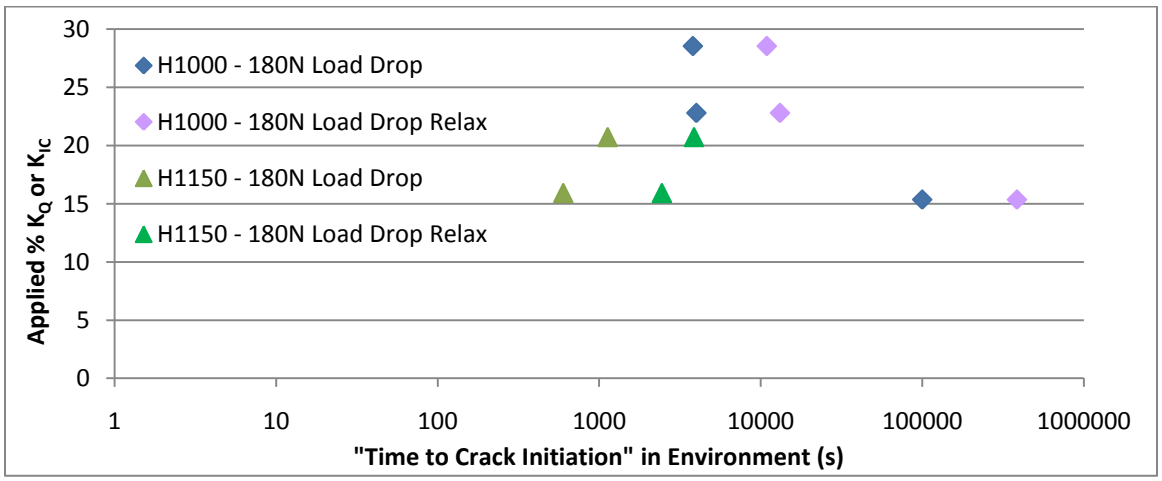

Figure 65: "Time to Crack Initiation" for PH 13-8Mo H1000 and H1150

Surprisingly, the H1150 condition appears to display similar or worse resistance to crack initiation when compared to the H1000 condition at both equivalent applied K levels and percentages of K_{IC} (K_Q) based on Figures 64 and 65. At the very least, one would expect the H1150 condition to behave similarly to the SA condition since their mechanical properties (YS, UTS, and RA) are nearly identical. The H1150 condition's yield strength is slightly lower than the SA's, meaning it will experience greater deformation and possess a larger plastic zone size for a given applied stress intensity, but

only to such a degree. The largest difference between the SA and H1150 conditions is the microstructure. Since austenite is known to be an excellent hydrogen trap, it is possible that the austenite, in addition to the coarser Ni_3Mo/Ni_4Mo precipitates in the H1150 condition, cause crack initiation to occur earlier than either the H1000 or SA samples. As before, comparisons at equal percentages of K_{IC} (K_Q) are limited due to an invalid K_{IC} measurement for the H1150 condition. In order to have resistance similar to the H1000 condition at equal *percentages* of KIC, the true toughness of the H1150 condition would need to be less than 100MPa√m. Because the true toughness of H1150 is higher than H1000, it is *possible* that cracks do *initiate* sooner in the H1150 condition (alternatively, the failure criterion may need to be revised). In either case, repeat measurements for both the H1150 and SA conditions, as well as verification of crack initiation times by physically examining the samples, would be extremely beneficial in improving the accuracy of this analysis.

Crack initiation is not the only way to define resistance to hydrogen embrittlement though. A crack might initiate, but if it cannot propagate (or does so very slowly), then it may pose less of a risk than a crack with a lower chance of initiation but higher rate of propagation, and therefore, potential for catastrophic failure. From the compliance equations, crack lengths can be calculated as a function of time. To determine crack growth, the points of crack initiation (180N/40lbf load drop – no relaxation adjustment) are taken to be the origin of the crack extension versus time curve (0 time, 0 crack extension). Crack extension, plotted as a function of time, is shown below in Figure 66:

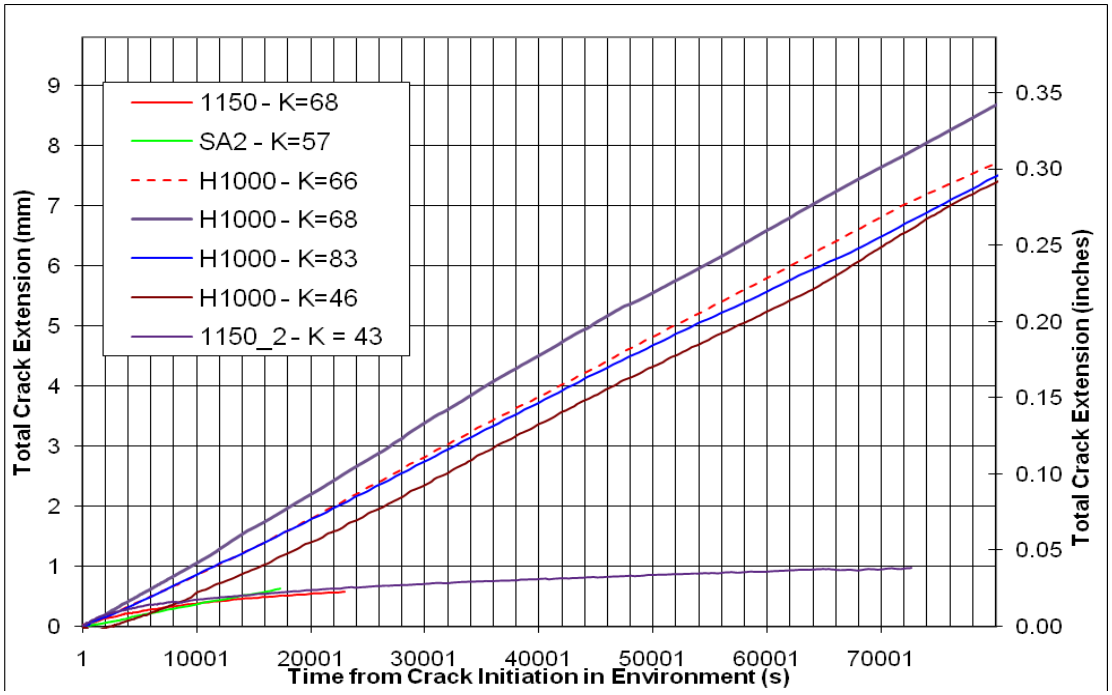

Figure 66: Crack Extension as a Function of Time for PH 13-8Mo H1000, H1150, and SA

Initially, crack extensions for the different samples vary significantly in the first hour (3600s). However, by 10,000s (about 3 hours), it is quite clear that cracks are growing at differing rates. Interestingly, the H1000 sample at K=68 MPa-$m^{½}$ has the highest crack growth rate despite the fact that it is not the sample carrying the highest stress. For the two H1150 samples that were tested, both exhibit higher initial crack growth rates than the SA sample that was tested. Beyond 10,000s (~3 hours), the predicted crack growth rates for the H1150 samples fall below the crack growth rate of the SA sample and appear to begin to level off. More importantly, beyond ~3000s (roughly 1 hour), the two H1150 samples and single SA sample have lower total crack extensions and lower crack growth rates than any of the H1000 samples.

Examining the crack growth and crack growth rates of the H1000, H1150, and SA samples provides evidence that resistance to hydrogen embrittlement, based on long-term

exposure to a hydrogen environment, is greatest in the H1150 condition followed by the SA and H1000 conditions, which is in agreement with what has been established in literature from a qualitative standpoint. Usage of the established failure criterion for the H1000 condition suggests that crack initiation times, compared to the H1000 condition, were equal or better for the SA condition and equal or worse for the H1150 condition. While these pieces of data appear to conflict with one another, they are not necessarily contradicting, as most of the previous work did not describe crack initiation, but fatigue crack growth rate (FCGR), reduction in strength/ductility via notched tensile strength (NTS), or permeation/diffusion rates. A crack that initiates quickly, but propagates extremely slowly, could satisfy both low FCRG and smaller reductions in NTS (observations of previous work) while still being consistent with the data presented herein. Actual measurement of crack initiation by removing samples from the acid bath after prescribed periods of time could be used to evaluate the validity of the failure criterion across the three heat treatments and help determine which heat treatments are indeed most sensitive to HE (this method, unfortunately, would require large numbers of samples for testing). For initial crack lengths (as measured), final crack lengths (as measured), and the compliance-predicted final crack lengths, the reader is directed to Table A8 in the Appendix.

SEM Fractography and Analysis

Samples from all three tempers were analyzed under SEM after being exposed to HCl. For the H1000 condition, the results demonstrate a consistent, time-dependent fracture behavior. The H1150 and SA samples differed significantly – samples in the H1150 condition formed appreciable amounts of oxide in the fatigue pre-crack front, but

showed no evidence of a brittle fracture mode. SA samples possessed oxide formations along the edge of the fatigue pre-crack front, just before hydrogen embrittlement began extending the crack. While the oxides in the H1150 sample should have little effect on its crack behavior (since the oxides were not at the edge of the crack), they may have assisted the SA condition and provided some degree of resistance to HE either by acting as a trap (oxides have high binding energies, see Table 2) or by acting as a diffusion barrier. Below is the typical, long-term fracture specimen of the H1000 condition in Figure 67.

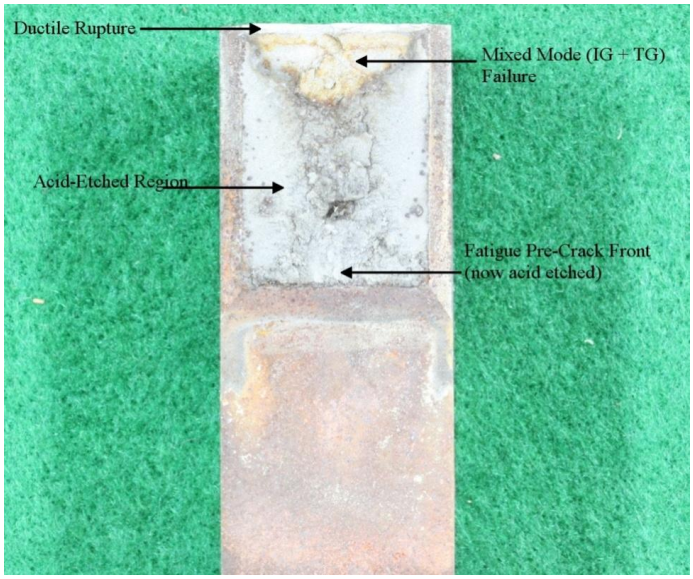

Figure 67: A Typical Fracture Surface for PH 13-8Mo H1000 Under Long-Term Acid Exposure

The bulk of the sample fracture surface has been eaten away by the acid. However, some features remain. Beyond the (former) fatigue crack front at the bottom of the image, there exists a V-shaped triangle which constitutes the brittle failure region. This region has been severely embrittled by the hydrogen. The brittle failure region is

primarily intergranular (IG) fracture, as shown in Figure 68. Interestingly, there is a transition between the brittle failure and ductile failure regions that is composed of mixed transgranular (TG) fracture and dimple-rupture fracture morphology, as featured in Figure 69.

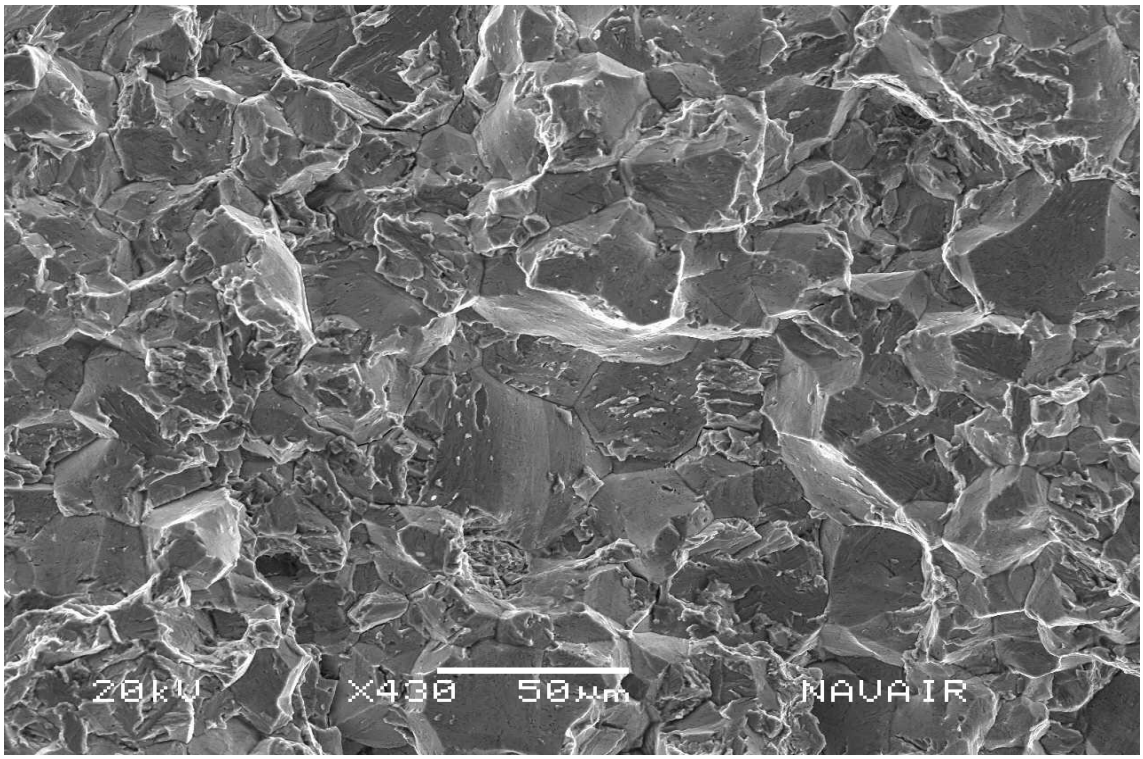

Figure 68: Intergranular Fracture Dominates the Brittle Fracture Zone

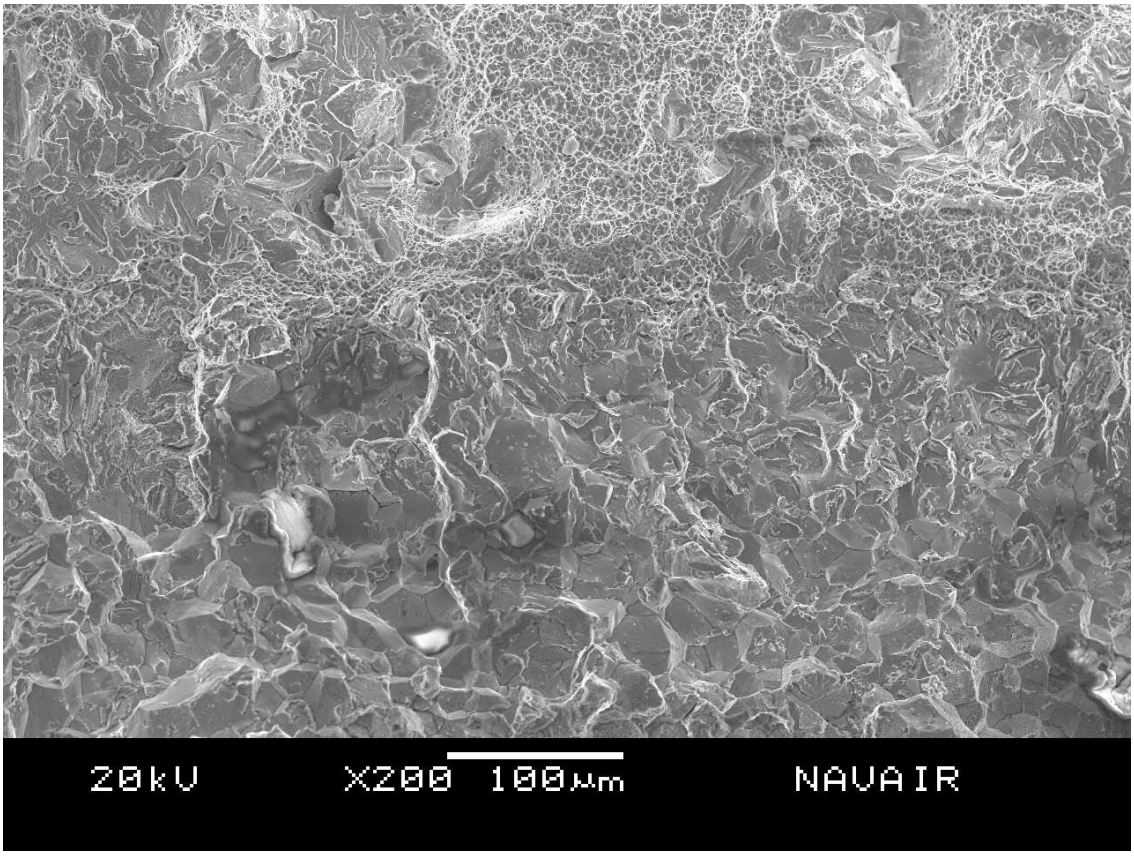

Figure 69: Mixed-Mode Fracture was found After Tearing HE Samples Open.
The initial HE fracture is intergranular, but once removed from the HE environment and loaded, the fracture mode transitioned from inter- to trans-granular fracture and then ductile rupture

The V-shaped brittle fracture zone is observed in long-term specimens as a result of the side-grooving process. While side-grooves add constraint to the C(T) specimen, they also increase the stress along the edge of the material. When crack extension occurs in steps (as in fatigue or environmentally assisted cracking), the increased stress along the side-grooves results in a non-uniform growth along the original crack front. Initially the crack growth remains uniform because the stress intensity factor along the crack front is uniform. With sufficient crack lengths (resulting in larger stress intensity factors), however, the crack front begins to grow faster along the edges. Samples that were held

exposed to the acid for only a few hours retained their uniform crack fronts despite side-grooving on account of the limited total crack extension.

The H1150 samples examined possessed vastly different fracture behaviors than the H1000 condition material.

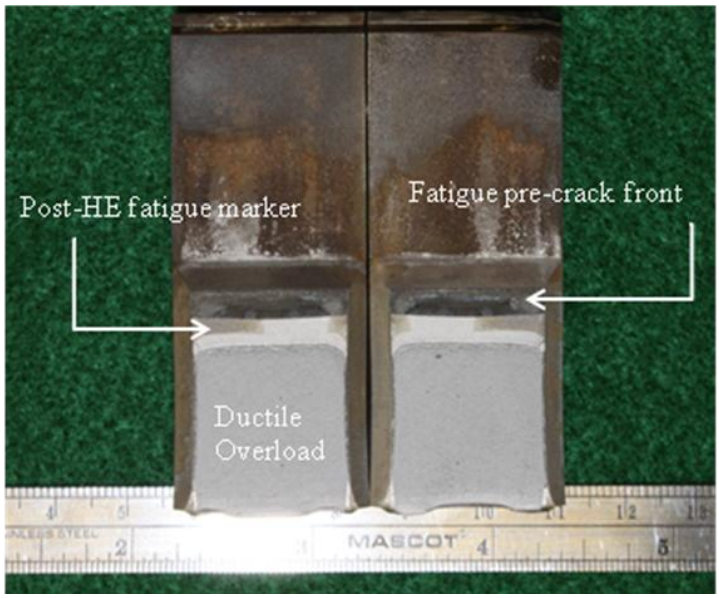

Figure 70: Optical Photo of PH 13-8Mo H1150 Exposed to Acid.

Featured above is the fatigue crack front of one of the acid-exposed H1150 samples (Figure 70). Most of the fatigue front has been etched away, although large amounts of oxide had formed just before the end of the pre-crack front. A partially corroded fatigue region from the post-HE fatigue marking is immediately observed afterwards. Unlike the H1000 samples, no brittle failure region is readily identifiable to the naked eye.

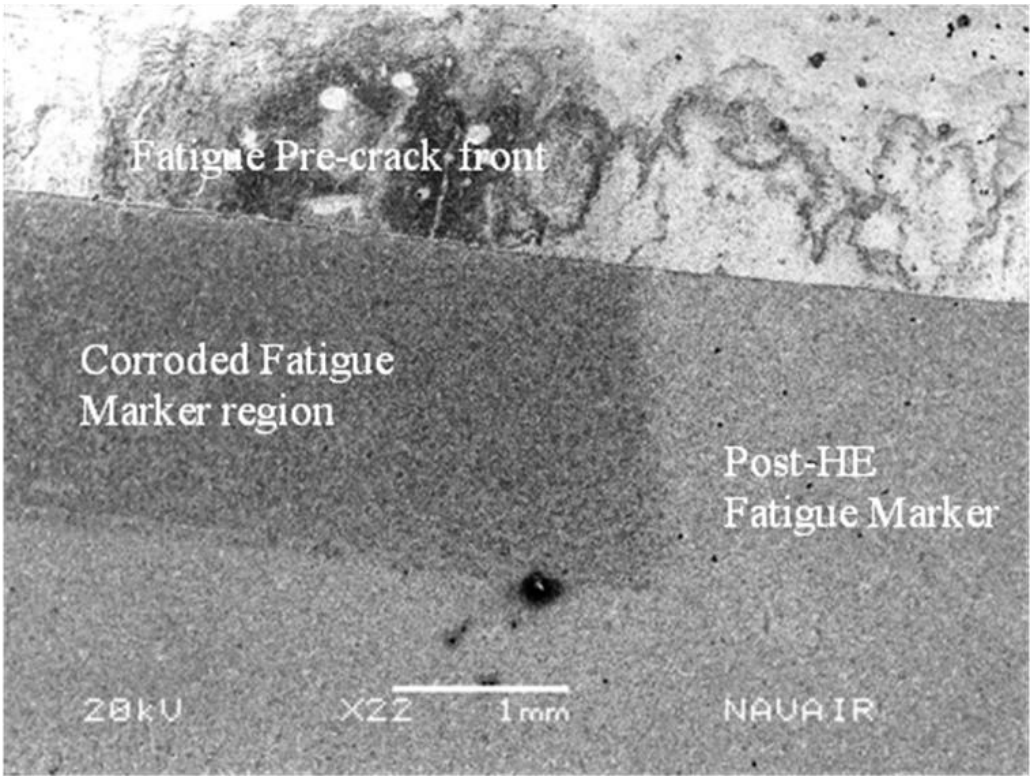

Figure 71: SEM Overview of the H1150 Fracture Surface

Examination under the SEM yielded no evidence of brittle crack growth anywhere in the fatigue marker region. This is especially puzzling in light of the fact that both load drops and clip gage extensions were recorded, and based on the compliance equations, the crack should have extended. However, there were no observable morphological differences between the corroded and uncorroded regions of the post-HE fatigue marker region, as shown in Figure 72, which would indicate any type of brittle crack growth. The next region that was examined was the interface between the original fatigue pre-crack and the fatigue marker, shown in Figure 73. At the interface of the un-corroded region (top of Figure 73), the original pre-crack front is heavily etched and some oxides appear on the right side of the image. The Post-HE fatigue marker shows fracture morphology typical of fatigue. For the corroded region (bottom of Figure 73),

however, the fatigue pre-crack is much more heavily etched. In addition, there appears to be a “shelf” at the interface, where crack growth appears to come out of the page.

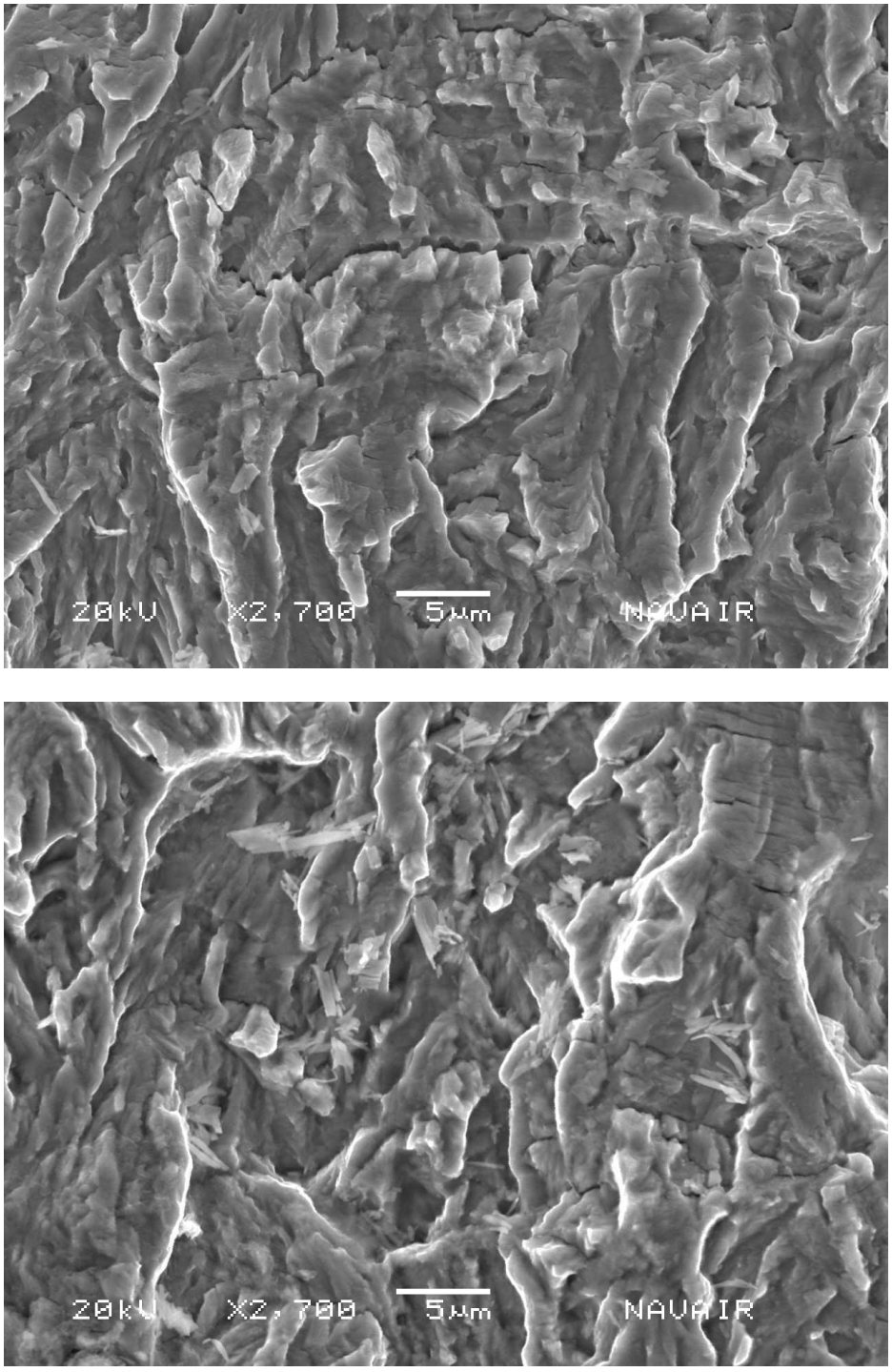

Figure 72: Fatigue Marker region (top) and Corroded Fatigue Marker Region (bottom)

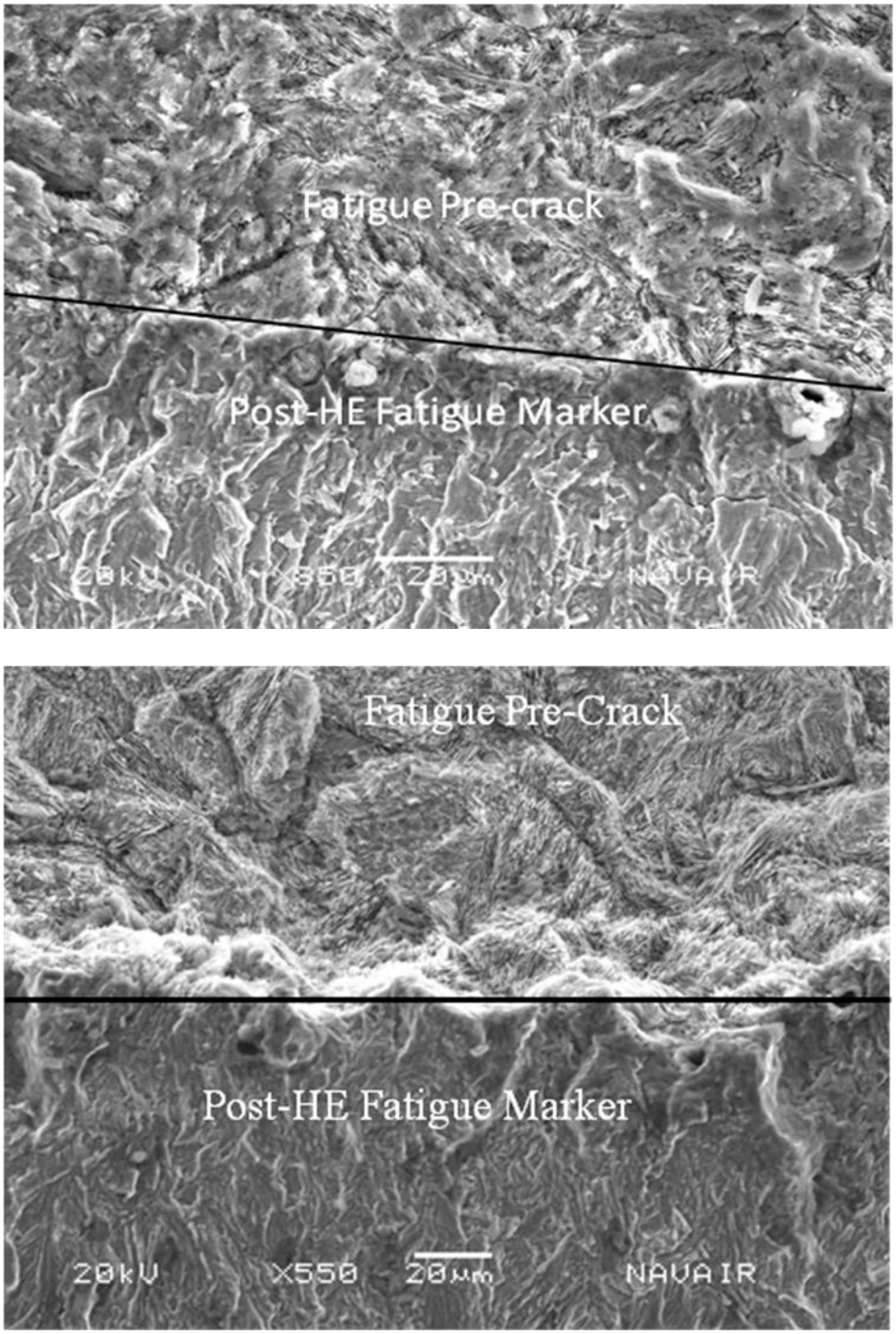

Figure 73: Interfaces Between the Fatigue Pre-Crack and the Post-HE Fatigue Marker.
On the top image, the post-HE fatigue marker saw no corrosion, but on the bottom image, discoloration due to corrosion was visible. No meaningful difference was found between the two, however.

This “shelf” could legitimately be a legitimate form of crack extension, since its morphology appears to be similar to other acid-etched regions. Alternatively, it could simply be the result of crack tunneling/branching during the fatigue pre-cracking process that was subsequently etched and exposed during hydrogen embrittlement testing.

Similar to the H1150 condition, the SA condition also formed oxides in the fatigue pre-crack area. Unlike the H1150, however, the SA sample possessed a fracture region whose morphology was clearly different than the preceding fatigue pre-crack or the post-HE fatigue marker, as shown below in Figure 74:

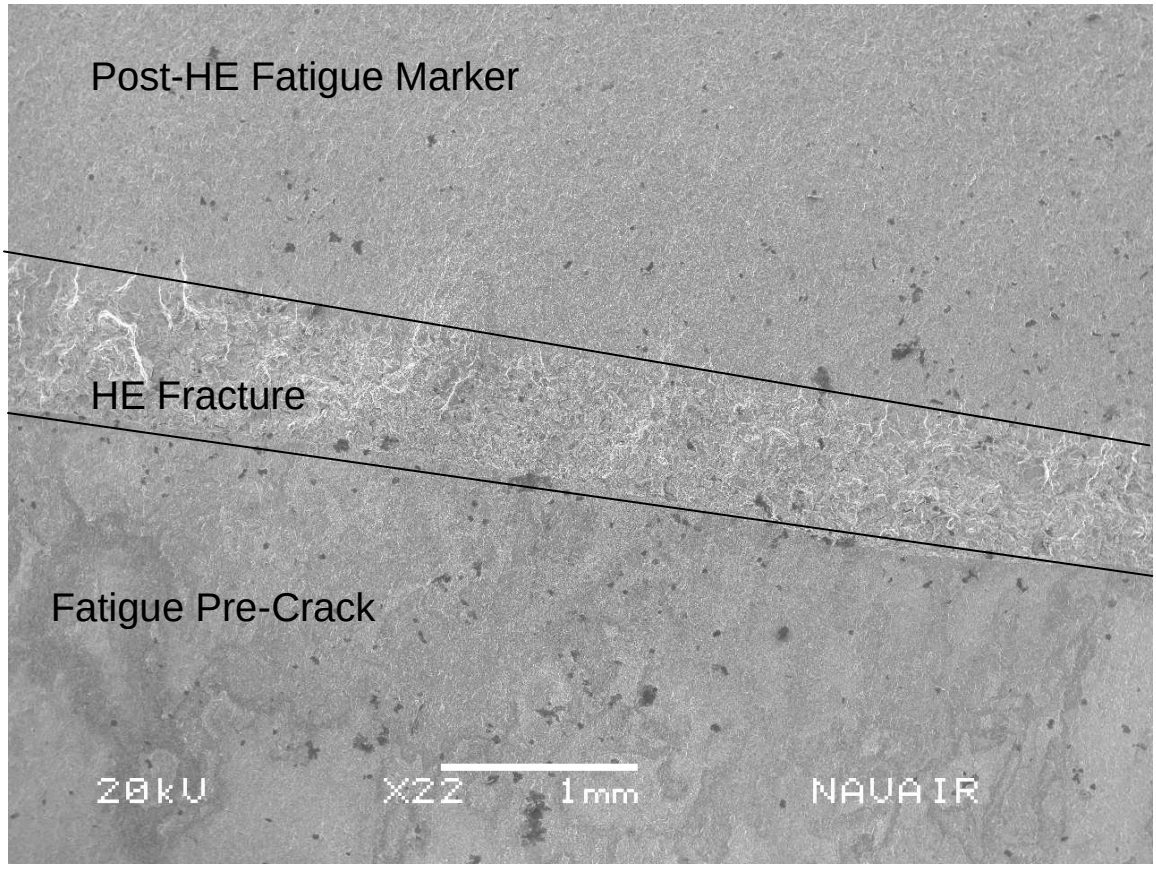

Figure 74: An Overview of the SA Sample Fracture Surface.

The fatigue-pre crack region of the SA sample was mostly acid-etched, though some oxides were present. Close-up images of the SA sample's hydrogen embrittlement region in Figure 75 show fracture surfaces that have been heavily eaten by the acid. It appears that the original fracture may have been a combination of intergranular and transgranular fracture, though it cannot be said with absolute certainty one way or another. Grain boundaries are clearly exposed in the 200x image (top), however closer examination in the 550x (bottom) shows that some grains have been cut through as well, indicating transgranular fracture. This could, however, also simply be the effects of the acid exposure.

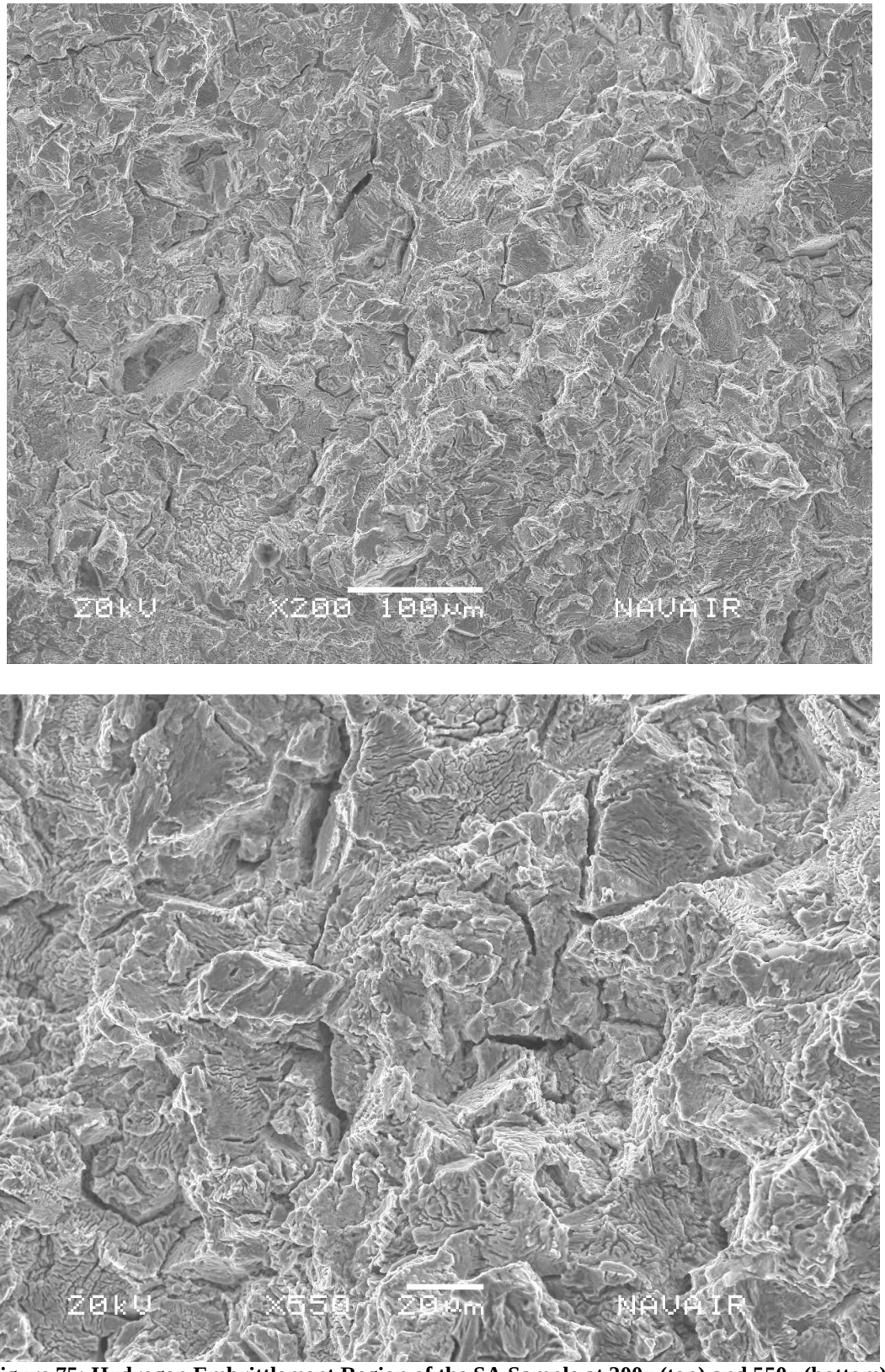

Figure 75: Hydrogen Embrittlement Region of the SA Sample at 200x (top) and 550x (bottom).

Examination of the transition region from the HE fracture to the Post-HE Fatigue Marker yielded completely different fracture morphologies (quite unlike the H1150 condition, where no appreciable different, aside from color, could be made)

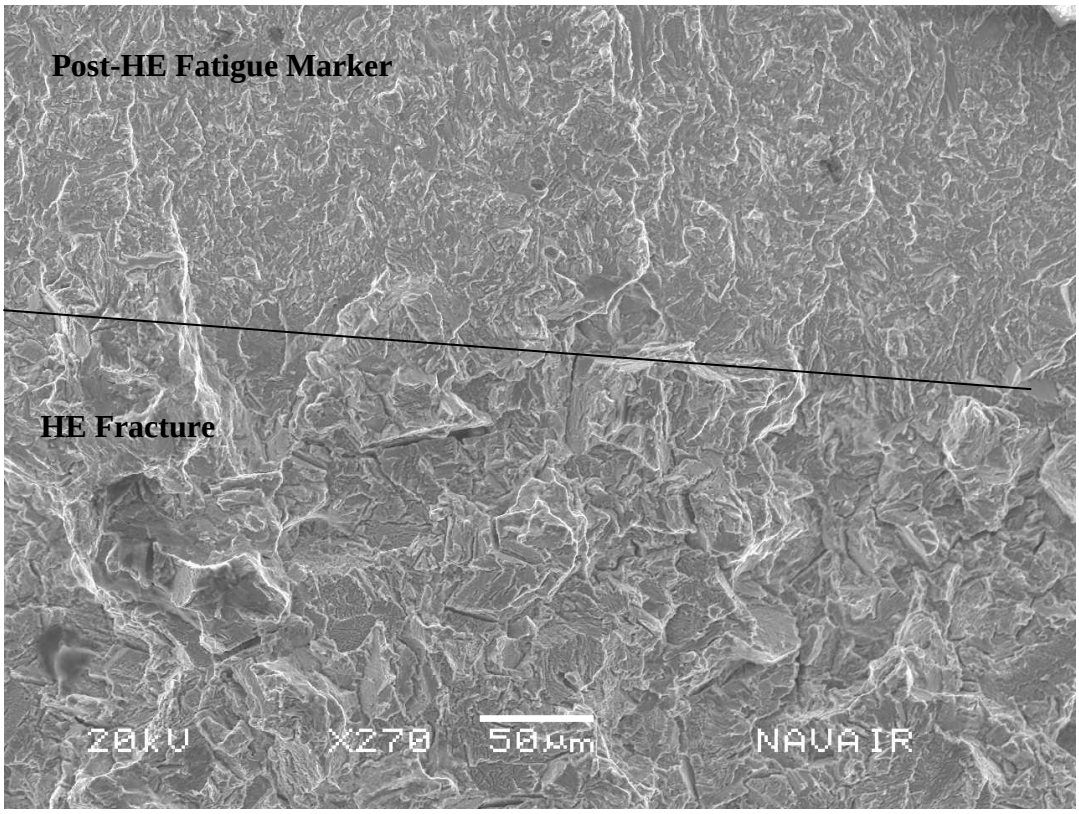

Figure 766: SA Sample Transition Region from HE Fracture to Post-HE Fatigue Marker.

The fatigue marker region showed no unusual structure, appearing relatively similar to the fatigue marker region in the H1150 condition. Some very small lines, appearing like fatigue striations, are circled in black. The expected striation size is sub-micron.

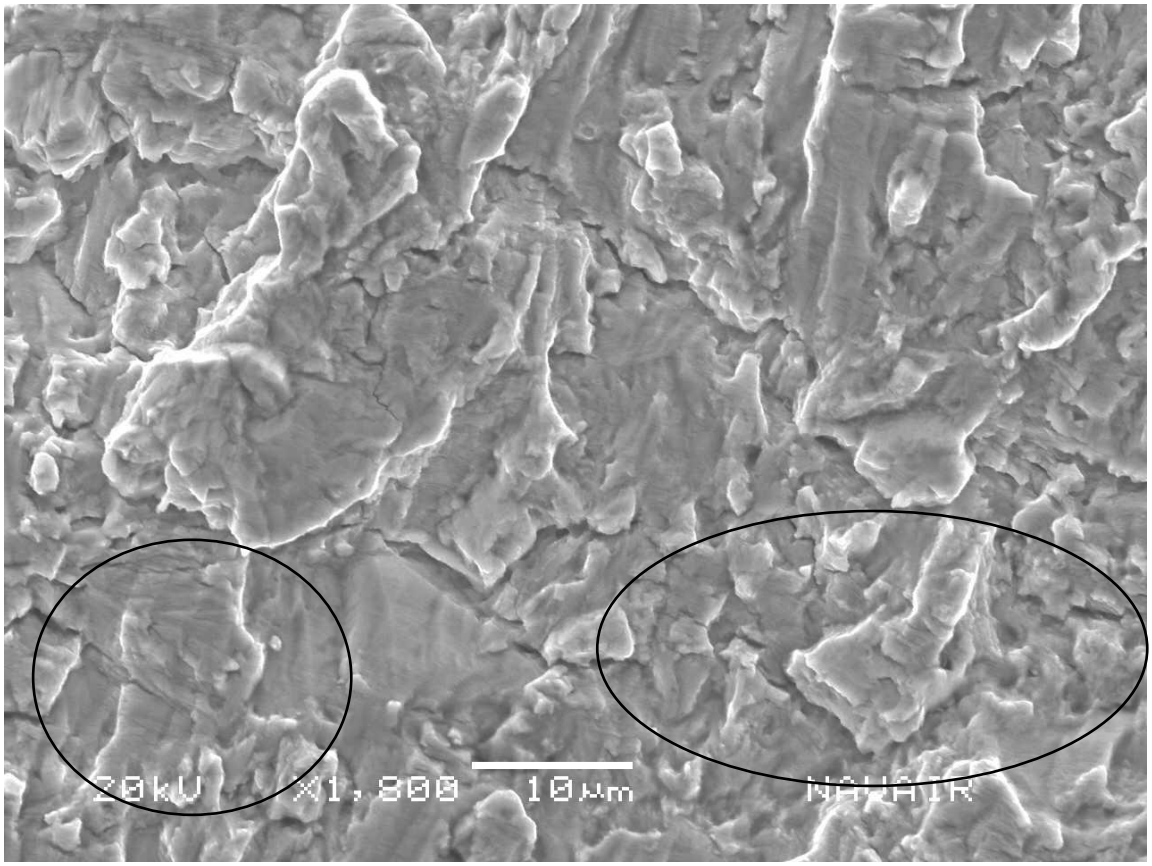

Figure 776: SA Sample Transition Region from HE fracture to Post-HE Fatigue Marker.

Overall, then, SEM analysis indicates brittle failure in H1000 condition material, as evidenced by images of intergranular and transgranular failure. The exact nature of fracture in the SA and H1150 is unclear due to corrosion of the fractured surface in the SA condition and no visual indications of brittle failure anywhere in the H1150 condition. These two observations further support the conclusion that both the SA and H1150 conditions possess superior resistance to HE crack *growth*, despite their apparent early crack initiation, as compared to the H1000 condition, which is consistent with results reported by other authors.

Conclusion

Mechanical and microstructural analyses on PH 13-8Mo were successfully performed via tensile, fracture toughness, and hydrogen embrittlement testing as well as metallography, EBSD, and scanning electron microscopy.

PH 13-8Mo in the H1000 condition has been shown to be highly susceptible to hydrogen embrittlement under acid environments. Between K levels of 80% and 20% K_{IC}, crack initiation is extremely rapid (approximately $\leq$ 1 hour). Below 20% K_{IC}, the time required for crack initiation is greatly extended. It has been suggested by Gangloff (2) that the threshold levels for hydrogen embrittlement, K_{TH}, can be as low as 5-10% of the measured K_{IC}. Though Kth was not measured in this work, this observation is not in conflict with the data reported herein (see Figure 62).

It was found that for similar applied K levels, the H1150 and SA conditions offered similar or superior resistance to crack initiation as compared to the H1000 condition based on the proposed failure criterion (Figures 63 and 64), with the SA having greater longer initiation times than the H1150 condition. At equivalent percentages of applied K_{IC} (K_Q) (Figures 63 and 65), the SA also appeared to have the greatest resistance to crack initiation, while the H1000 condition appeared to be superior to the H1150. These results conflict somewhat with what has been established in literature so far (the SA and H1150 conditions should both be superior to H1000; H1150 should be superior to SA). Crack extension analysis (Figure 66), however, showed that the H1150 condition offered the best resistance to crack growth. SEM analysis supported this result, as no evidence of brittle fracture was found in the H1150 condition samples (Figure 73). The austenite content of the H1150 condition may reduce crack initiation time when

compared to the H1000 condition, but may also prevent/retard crack growth. More work is needed to accurately quantify the crack initiation times for the SA and H1150 conditions and account for the discrepancies between the measured behavior and the reportedly high resistance to HE.

SEM analysis also showed dramatically different fracture surfaces for each temper of PH 13-8Mo. The H1000 condition clearly experienced brittle fracture behavior (Figure 68-69), while the SA and H1150 conditions appeared to have little or no brittle failure (Figures 74 and 73, respectively). It may be that different tempers of PH 13-8Mo may subject to entirely different crack initiating mechanisms – HE failure in high strength conditions (H950, H1000, etc.) might be a result of the decohesion mechanism, yielding intergranular fracture, while low-strength, overaged conditions – H1100, H1150 – could be the result of hydrogen enhanced localized plasticity (HELP), and the SA condition could be subject some combination of the two based on its unusual fracture surface.

EBSD analysis showed a potential orientation relationship, either the Kurdjumov-Sachs or the Nishiyama-Wasserman, between the martensite and the reverted austenite. Based on the orientation and positions of the reverted austenite in the H1150 condition within the microstructure, it was proposed that the reverted austenite possesses the same orientation as the prior austenite grain.

The resulting K-life data can be used to refine reworking parameters at Navy Fleet Readiness Centers (FRCs), improve accuracy of part lifing for aircraft, and improve design and understanding of aircraft components bearing residual stresses. In addition,

the orientation relationships may help better understand the processing of maraging steels and result in further research in this area.

Future Work

The path forward from this work can be taken in multiple directions. The K-Life curves for more UHS steels could be measured, failure criterion could be further refined, and more material parameters, such as texture or fracture facet orientations, could be analyzed.

Though the fracture mechanism of hydrogen embrittlement is typically designated as intergranular, many works have also cited mixed-mode (inter- and trans-granular) fracture surfaces. Even more interesting was the transgranular-ductile rupture transition region which was observed during this experimental work. Because the precipitates of PH steels possess a certain degree of coherency with the matrix, and because reverted austenite also has a unique orientation relationship via the KS/NW relationships, it is possible that transgranular fracture may occur on preferential crystallographic planes within the lattice. Several authors have explored the possibilities of EBSD Fractography on titanium and steel, using a variety of techniques including tilt fractography and serial sectioning (45; 46). Furthermore, Slavik and Gangloff (47) studied the effects of grain orientation on fatigue fracture. Their results suggest that texture analysis may also be of interest when analyzing preferential fracture.

Much work has been done, and still needs to be done, in order to more fully understand hydrogen embrittlement from the perspective of the underlying physics as well as the

macroscopic behavior in steels. The data presented herein will hopefully expand the current body of knowledge and provide new directions for further research.

List of References

1. **Davis, W.D.** *Solubility, Determination, and Diffusion and Mechanical Effects of Hydrogen in Uranium.* Knolls Atomic Power Laboratory, General Electric Company. Schenectady : General Electric Company, 1956.

2. **Gangloff, R.P.** Hydrogen Assisted Cracking of High Strength Alloys. [book auth.] R.O. Ritchie, B. Karihaloo I. Milne. *Comprehensive Structural Integrity.* New York : Elsevier Science, 2003.

3. *Hydrogen Embrittlement Failures of H-46 Rotorhead Components.* **Boyette, Brian.** Washington D.C. : NAVAIR, 2010. AIR 4.3 Conference.

4. *Precipitation Hardening in a PH 13-8 Mo Stainless Steel.* **V. Seetharaman, M. Sundararaman, R. Krishnan.** 1981, Materials Science and Engineering, pp. 1-11.

5. **Anderson, T.L.** *Fracture Mechanics: Fundamentals and Applications.* Boca Raton : Taylor & Francis Group, 2005.

6. **ASTM International.** *ASTM E1681 - 03: Standard Test Method for Determining Threshold Stress Intensity Factor for Environment-Assisted Cracking of Metallic Materials.* West Conshohocken : ASTM International, 2008.

7. *Reverted Austenite in PH 13-8 Mo Maraging Steels.* **Schnitzera, Ronald, et al.** 2010, Materials Chemistry and Physics, pp. 138-145.

8. *Aging Reactions in a 17-4 PH Stainless Steel.* **C.N. Hsiao, C.S. Chiou, J.R. Yang.** s.l. : Elsevier Science, 2002, Materials Chemistry and Physics, Vol. 74, pp. 134-142.

9. *Basic Aspects of the Problems of Hydrogen in Steels.* **Interrante, C.G. and Pressouyre, G.M.** Washington D.C. : American Society for Metals, 1982. Current Solutions to Hydrogen Problems in Steels. pp. 3-16.

10. *Effects of Hydrogen on the Properties of Iron and Steel.* **Hirth, J.P.** 1980, Metallurgical Transactions A, pp. 861-890.

11. *Hydrogen Embrittlement of PH 13-8 Mo Stainless Steel - The Effect of Surface Condition.* **Murray, G.T., Honegger, H.H. and Mousel, T.** 1984, Corrosion, pp. 146-151.

12. **Isecke, Bernd.** *Test Methods for Assessing the Susceptibility of Prestressing Steels to Hydrogen Induced SCC.* London : Maney Publishing, 2004. pp. 7-16.

13. *Hydrogen Embrittlement of Metals: A Primer for the Failure Analyst.* **Louthan, M.R. Jr.** 3, s.l. : Springer Boston, Vol. 8, pp. 289-307. 1547-7029.

14. **J.W. Martin, R.D. Doherty.** *Stability of Microstructure in Metallic Systems.* Cambridge : Cambridge University Press, 1980.

15. *Hydrogen-Enhanced Localized Plasticity - a Mechanism for Hydrogen-Related Fracture.* **Birnbaum, H.K. and Sofronis, P.** 1994, Materials Science and Engineering, pp. 191-202.

16. *Hydrogen Effects on Deformation - Relation Between Dislocation Behavior and the Macroscopic Stress-Strain Behavior.* **Birnbaum, H.K.** 1994, Scripta Metallurgica et Materialia, pp. 149-153.

17. *Hydrogen Effects on the Interaction Between Dislocations.* **Ferreira, P. J., Robertson, I. M. and Birnbaum, H. K.** 5, s.l. : Elsevier Science Ltd., 1998, Acta Metallurgica, Vol. 46, pp. 1749-1757.

18. *A Study of Hydrogen Transport During Plastic Deformation.* **Ladna, B. and Birnbaum, H.K.** 1987, Acta Metallurgica et Materialia, pp. 1775-1778.

19. *Hydrogen Trapping Phenomena in Metals with B.C.C and F.C.C. Crystal Structures by the Desorption Thermal Analysis Technique.* **Lee, Jai-Young and Lee, S.M.** 1986, Surface Coatings and Technology, pp. 301-314.

20. *Hydrogen Trapping by TiC Particles in Iron.* **H.G. Lee, Jai-Young Lee.** 1984, Acta Metallurgica et Materialia, pp. 131-136.

21. *Retained Austenite as a Hydrogen Trap in Steel Welds.* **Park, Y.D., et al.** 2002, Welding Journal, pp. 28-S - 35-S.

22. *Hydrogen Trapping in High Strength Steels.* **Pound, B.G.** 1998, Acta Materialia, pp. 5733-5743.

23. *A Kinetic Trapping Model for Hydrogen-Induced Cracking.* **Pressouyre, G.M. and Bernstein, I.M.** 1979, Acta Metallurgica et Materialia, pp. 89-100.

24. *Measurement and Modeling of Hydrogen Environment-Assited Cracking of Ultra-high Strength Steel.* **Lee, Yongwon and Gangloff, Richard P.** 2007, Metallurgical and Materials Transactions A, pp. 2174-2190.

25. **SAE Aerospace.** *AMS 5629E: Steel, Corrosion-Resistant, Bars, Wire, Forgings, Rings, and Extrusions 13Cr - 8.0Ni - 2.2Mo - 1.1Al Vacuum Induction Plus Consumable Electrode Melted Solution Heat Treated, Precipitation Hardenable.* Warrendale : SAE International, 2006.

26. **Leslie, W.C. and Hornbogen, E.** Physical Metallurgy of Steels. [book auth.] R.W. Cahn and P. Haasen. *Physical Metallurgy.* s.l. : Elsevier Science, 1996.

27. **Reed-Hill, Robert E. and Abbaschian, Reza.** *Physical Metallurgy Principles.* Boston : PWS Publishing Company, 1994.

28. *Gaseous Hydrogen Embrittlement of PH 13-8 Mo Steel.* **Y.S. Ding, L.W. Tsay, M.F. Chiang, C. Chen.** 2009, Journal of Nuclear Materials, pp. 538-544.

29. **Battelle Memorial Institute.** *Metallic Materials Properties Development and Standardization (MMPDS-04).* s.l. : Battelle Memorial Institute, 2008.

30. *Measurement and Calculation of Ferrite in Stainless-Steel Weld Metal.* **DeLong, W.T., Ostrom, G.A. and Szumachowski, E.R.** 1956, Welding Journal, pp. 521-s - 528-s.

31. **Shreir, L.L., Jarman, R.A. and Burstein, G.T.** *Corrosion.* 3rd Edition. Boston : Butterworth-Heinemann, 1994. Vol. I.

32. *Investigation of Hydrogen Sulfide Stress Corrosion Cracking of PH 13-8 Mo Stainless Steel.* **L.W. Tsay, M.Y. Chi, H.R. Chen, C. Chen.** 2006, Materials Science and Engineering A, pp. 155-160.

33. *Hydrogen Embrittlement Susceptibility and Permeability of Two Ultra-High Strength Steels.* **Tsay, L.W., et al.** 2006, Corrosion Science, pp. 1926-1938.

34. *Stress Corrosion Properties of High Strength Precipitation Hardening Stainless Steels.* **Carter, C.S., et al.** 1971, Corrosion, pp. 190-197.

35. **E.U. Lee, R. Taylor, C. Lei, H.C. Sanders.** *Aircraft Steels.* Naval Air Warfare Center Aircraft Division. Patuxent River : Naval Air Warfare Center Aircraft Division, 2009.

36. **ASTM International.** *ASTM E399-06: Standard Test Method for Linear-Elastic Plane-Strain Fracture Toughness KIC of Metallic Materials.* West Conshohocken : ASTM International, 2006.

37. —. *ASTM E8/E8M - 09: Standard Test Method for Tension Testing of Metallic Materials.* West Conshohocken : ASTM International, 2009.

38. **Ashby, Michael F. and Jones, David R.H.** *Engineering Materials I: An introduction to Properties, Applications, and Design.* Burlington : Elsevier BUtterworth-Heinemann, 2006.

39. **World Steel Association, University of Liverpool.** Strengthening Mechanisms: Overview. [Online] [Cited: September 12, 2010.] http://www.steeluniversity.org/content/html/eng/default.asp?catid=179&pageid=2081271923.

40. *Reverted Austenite During Aging in 18Ni(350) Maraging Steel.* **Li, Xiaodong and Yin, Zhongda.** 1995, Materials Letters, pp. 239-242.

41. **Porter, D.A. and Easterling, K.E.** *Phase Transformations in Metals and Alloys.* Cheltenham : Nelson Tohrnes Ltd, 2001.

42. **Hulinks.co.jp.** KSFCCBCC2.jpg. *hulinks.co.jp.* [Online] [Cited: July 16, 2010.] http://www.hulinks.co.jp/software/c-studio/images/KSFCCBCC2.jpg.

43. **Kocks, U.F., Tomé, C.N. and Wenk, H.-R.** *Texture and Anisotropy.* Cambridge : Cambridge University Press, 2000.

44. **ASTM International.** *ASTM F1624 - 09: Standard Test Method for Measurement of Hydrogen Embrittlement Threshold in Steel by the Incremental Step Loading Technique.* West Conshohocken : ASTM International, 2009.

45. *Crystallographic Analysis of Fracture Facets Using Electron Backscatter Diffraction.* **Randle, V.** 1999, Journal of Microscopy, pp. 226-232.

46. *Determining Fracture Facet Crystallography Using Electron Backscatter Patterns and Quantitative Tilt Fractography.* **Slavik, D.C., Wert, J.A. and Gangloff, R.P.** 1993, Journal of Materials Research, pp. 2482-2491.

47. *Environment and Microstructure Effects on Fatigue Crack Facet Orientation in an Al-Li-Cu-Zr Alloy.* **Slavik, D.C. and Gangloff, R.P.** 9, 1996, Acta Materialia, Vol. 44, pp. 3515-3534.

Appendix A: Additional Mechanical Testing Data

Table A1: Crack Initiation Times (s) for Percentage Load Drop Criterion

% K_{IC}	1% Load Drop	3% Load Drop	5% Load Drop
88	903	5119	9058
86.2	315	4159	8401
84.4	357	2897	7189
80.6	1887	6482	10919
65.9	2594	6230	10167
63.6	2392	6836	11420
45.1	1382	8906	13926
29.2	3149	7947	12672
23.3	2090	7292	11672
17.1	8401	108727	139742

Table A2: Crack Initiation Times (s) for Absolute Load Drop Criterion

% K_{IC}	180N Load Drop	310N Load Drop	450N Load Drop
88	305	609	1230
86.2	305	305	420
84.4	357	357	357
80.6	756	1634	2543
65.9	1735	2695	3452
63.6	1331	2745	3705
45.1	1382	5270	7391
29.2	3806	6381	8451
23.3	4000	7039	9766
17.1	100097	125740	203770

Table A3: Crack Initiation Times (s) for Absolute CMOD Criterion

% K_{IC}	0.038mm CMOD	0.057mm CMOD	0.076mm CMOD
88	525	2038	2644
86.2	304	315	1331
84.4	357	357	357
80.6	1432	1937	3149
65.9	3301	3806	4715
63.6	2442	3503	4412
45.1	6179	7846	9620
29.2	6634	8048	8906
23.3	5423	7544	8908
17.1	114730	128740	363860

Table A4: Relaxation Adjusted Crack Initiation Times (s) for Percentage Load Drop Criterion

% K_{IC}	1% Load Drop	3% Load Drop	5% Load Drop
88	2189	7037	11420
86.2	598	5977	10668
84.4	357	4411	9310
80.6	3704	8653	13424
65.9	4209	8653	12923
63.6	4664	9916	14927
45.1	8906	14927	20188
29.2	9916	15177	19937
23.3	11171	16181	20940
17.1	382865	387872	392875

Table A5: Relaxation Adjusted Crack Initiation Times (s) for Absolute Load Drop Criterion

% K_{IC}	180N Load Drop	310N Load Drop	450N Load Drop
88	546	1735	2846
86.2	304	347	1230
84.4	357	357	357
80.6	2189	3401	4411
65.9	3452	4260	5118
63.6	3805	4967	6330
45.1	8855	11169	13174
29.2	10919	13424	15929
23.3	13175	15930	18686
17.1	385866	390874	395876

Table A6: Relaxation Adjusted Crack Initiation Times (s) for Absolute CMOD Criterion

% K_{IC}	0.038mm CMOD	0.057mm CMOD	0.076mm CMOD
88	903	1886	2644
86.2	315	1129	2290
84.4	357	357	367
80.6	1406	2088	3300
65.9	2795	3704	4563
63.6	2139	3199	4411
45.1	5876	7593	9411
29.2	5371	7088	8800
23.3	5423	7544	8908
17.1	10919	37472	109727

Table A7: Applied K Levels and Measured Crack Lengths for All Samples

Sample	Applied % $K_{IC}(K_Q)$	Time in Acid (hrs)	Average A_o (mm)	Average A_f (mm)	Average Crack Growth (mm)
H1000_18	87	4.6	26.29	28.61	2.33
H1000_22	84	6	26.24	28.23	1.99
H1000_17	83	7.6	26.18	28.56	2.38
H1000_13	78	49.3	26.36	50.41	24.05
H1000_14	65	42.2	26.36	47.51	21.16
H1000_12	59	49.3	26.18	50.41	24.24
H1000_11	45	49.3	26.11	50.44	24.33
H1000_21	29	6	26.24	28.70	2.46
H1000_9	15	7.8	26.23	29.51	3.29
1150 HE	**88**	**6.7**	**29.17**	**29.64**	**0.47**
H1000_20	90	114.9	26.32	32.53	6.21
SA HE2	**62**	**6**	**26.63**	**27.29**	**0.65**
1150 HE2*	**69**	**20.3**	**26.39**	-	-

*The final crack length for the H1150 HE2 sample was unable to be determined unambiguously either visually or under SEM.

Table A8: Final and Predicted Final Crack Lengths for All Samples

Sample	Avg Af (mm)	Compliance Af (mm)	% Difference	a/W > 0.8?
H1000_18	28.6	31.1	-8.5%	no
H1000_22	28.2	30.5	-8.0%	no
H1000_17	28.6	30.2	-5.8%	no
H1000_13	50.4	47.7	5.4%	yes
H1000_14	47.5	46.5	2.2%	yes
H1000_12	50.4	46.9	7.0%	yes
H1000_11	50.4	47.4	6.1%	yes
H1000_21	28.7	28.7	0.1%	no
H1000_9	29.5	31.5	-6.8%	no
1150 HE	**29.6**	30.5	-2.9%	no
H1000_20	32.5	32.6	-0.3%	no
SA HE2	**27.3**	27.7	-1.5%	no
H1150 HE2	-	27.88	-	no

Note: The compliance equations are typically valid from $0.2 < a/W < 0.8$. However, because of the acidic environment, additional reactions around the crack tip may be responsible for the discrepancies in the measured and compliance-predicted final crack lengths when $a/W < 0.8$

Graph A9: PH 13-8Mo H1000 Engineering Stress-Strain Curve

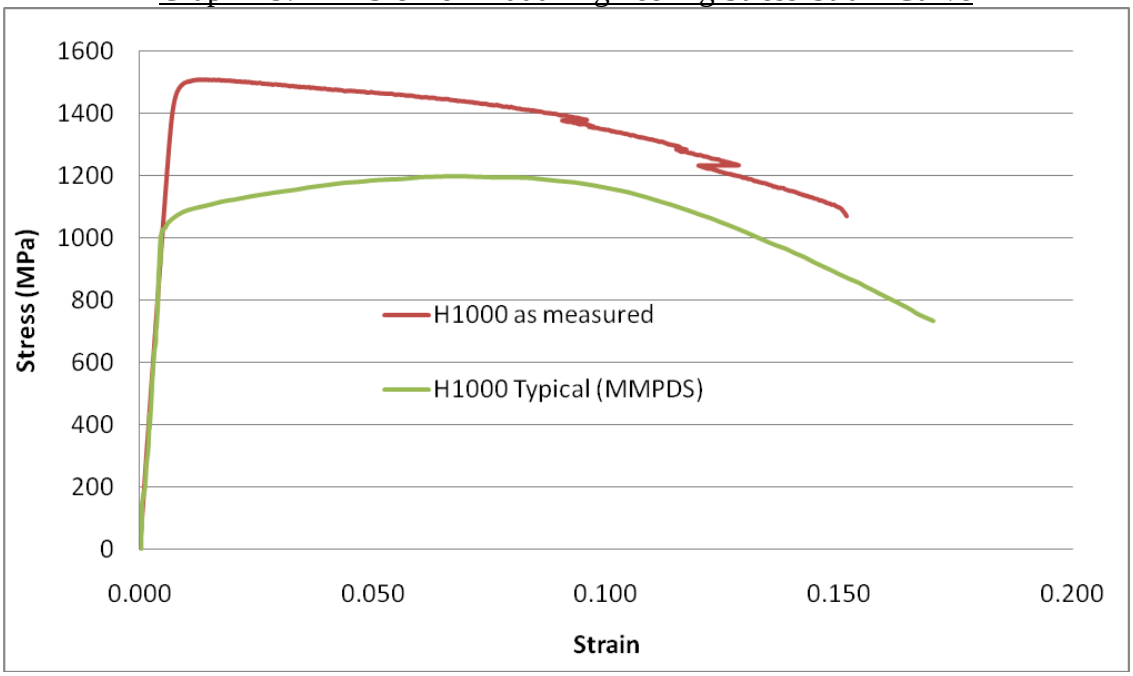

Note: Clip gage slippage occurred in the "as measured" recording.
Typical stress-strain curves for H1150 and SA unavailable from MMPDS

Matlab Data Reduction Analysis Scripts

Logarathmic Data Reduction (logdatared.m)

```
function [reduceddata reducedtime] = logdatared(signal, time)

%%%reduces data where time is used in the log10 scale
%%%and data is sparse near      t = 0

%%%% data must be input with time already in the log10 scale

timeavg = zeros(1620,1);
dataavg = timeavg;
i=1;
j=1;
L=length(time);
while i <= L
if time(i) <= 1
    dataavg(j,1) = mean((signal(i:(i+1))));
    timeavg(j,1) = mean((time(i:(i+1))));
   i=i+2;
   j=j+1;
    elseif time(i) > 1 && time(i) <= 2
    dataavg(j,1) = mean((signal(i:(i+4))));
    timeavg(j,1) = mean((time(i:(i+4))));
    i=i+5;
    j=j+1;
    elseif time(i) > 2 && time(i) <= 3
       if i+20 >= length(time)
     dataavg(j,1) = mean((signal(i:end)));
    timeavg(j,1) = mean((time(i:end)));
       else
    dataavg(j,1) = mean((signal(i:(i+19))));
    timeavg(j,1) = mean((time(i:(i+19))));
    i=i+20;
    j=j+1;
       end
    elseif time(i) > 3 && time(i) <= 4
       if i+100 >= length(time)
     dataavg(j,1) = mean((signal(i:end)));
    timeavg(j,1) = mean((time(i:end)));
    i=length(time);
       else
    dataavg(j,1) = mean((signal(i:(i+99))));
    timeavg(j,1) = mean((time(i:(i+99))));
    i=i+100;
    j=j+1;
       end
    elseif time(i) > 4 && time(i) <= 5
       if i+500 >= length(time)
     dataavg(j,1) = mean((signal(i:end)));
```

```
    timeavg(j,1) = mean((time(i:end)));
    i=length(time);
       else
       dataavg(j,1) = mean((signal(i:(i+499))));
       timeavg(j,1) = mean((time(i:(i+499))));
    i=i+500;
    j=j+1;
       end
    elseif time(i) > 5 && time(i) <= 6
       if i+2000 >= length(time)
     dataavg(j,1) = mean((signal(i:end)));
     timeavg(j,1) = mean((time(i:end)));
     i=length(time);
       else
    dataavg(j,1) = mean((signal(i:(i+1999))));
    timeavg(j,1) = mean((time(i:(i+1999))));
    i=i+2000;
    j=j+1;
       end
end
i=i+1;
end
r = min(find(timeavg==0)) - 1;
reduceddata = dataavg(1:r,1);
reducedtime = timeavg(1:r,1);
end
```

Stress Intensity and Crack Length Calculation using Front Face Compliance for C(T) Specimen (kacalcfrontface.m)

```
function [K,a] = KAcalcfrontface(P,CMOD,b,bn,ao,Y)
W = 2;
L = length(CMOD);

StressINT = zeros(L,1);
E = Y;
Be = b-((b-bn)^2)/2;
B = sqrt(b*bn);
A = zeros(L,1);
F = A;
for i = 1:L
u = 1/(sqrt((Be*E*CMOD(i)/P(i))) + 1);
A(i) =(1 - 4.5*u + 13.157*(u^2) - 172.551*(u^3) + 879.944*(u^4) - 1514.671*(u^5));
end
a = W*A;

for i = 1:L
   F(i) = ((2+A(i))/((1-A(i))^1.5))*(0.886 + 4.64*(A(i)) - 13.32*(A(i)^2) + 14.72*(A(i)^3) - 5.6*(A(i)^4));
   StressINT(i) = (P(i)*F(i))/(B*sqrt(W));
end
K = StressINT/1000;
```